Creation and Control of Entanglement in Condensed Matter Spin Systems

Stephanie Simmons

Magdalen College

A thesis submitted for the degree of Doctor of Philosophy
At the University of Oxford
Trinity Term 2011

Creation and Control of Entanglement in Condensed Matter Spin Systems

Stephanie Simmons
Magdalen College
Trinity Term 2011

An abstract submitted for the degree of Doctor of Philosophy

The highly parallel nature of the fundamental principles of quantum mechanics means that certain key resource-intensive tasks — including searching, code decryption and medical, chemical and material simulations — can be computed polynomially or even exponentially faster with a quantum computer. In spite of its remarkably fast development, the field of quantum computing is still young, and a large-scale prototype using any one of the candidate quantum bits (or 'qubits') under investigation has yet to be developed.

Spin-based qubits in condensed matter systems are excellent candidates. Spins controlled using magnetic resonance have provided the first, most advanced, and highest fidelity experimental demonstrations of quantum algorithms to date. Despite having highly promising control characteristics, most physical ensembles investigated using magnetic resonance are unable to produce entanglement, a critical missing ingredient for a pure-state quantum computer. Quantum objects are said to be entangled if they cannot be described individually: they remain fundamentally linked regardless of their physical separation. Such highly non-classical states can be exploited for a host of quantum technologies including teleportation, metrology, and quantum computation.

Here I describe how to experimentally create, control and characterise entangled quantum ensembles using magnetic resonance. I first explore the relationship between entanglement and quantum metrology and demonstrate a sensitivity enhancement over classical resources using molecular sensors controlled with liquid-state nuclear magnetic resonance. I then examine the computational potential of irreversible relaxation processes in combination with traditional reversible magnetic resonance control techniques. I show how irreversible processes can polarise both nuclear and electronic spins, which improves the quality of qubit initialisation. I discuss the process of quantum state tomography, where an arbitrary quantum state can be accurately measured and characterised, including components which go undetected using traditional magnetic resonance techniques. Lastly, I combine the above findings to initialise, create and characterise entanglement between an ensemble of electron and nuclear spin defects in silicon. I further this by generating pseudo-entanglement between an ensemble of nuclear spins mediated by a transient electron spin in a molecular system. These findings help pave the way towards a particular architecture for a scalable, spin-based quantum computer.

ACKNOWLEDGEMENTS

I owe a great deal to the people who have supported me in working towards this goal. First and foremostly I am indebted to my supervisor John Morton who has been an excellent supervisor — dedicated, detailed and great fun at conferences. I'd like to thank my supervisors Arzhang Ardavan and Andrew Briggs for their support, perspective and insight.

I'd like to thank the entire QSD cohort for being such great people to work and travel with, although I admit it's likely I'll always be a bit apprehensive about German lakes from now on. Specifically, I would also like to give thanks to Richard George who has been a source of inspiration for me since day one. Most importantly I must give a heartfelt thanks to Richard "Scruff" Brown and the patient Vasileia Filidou for staying in the lab on countless nights until way beyond what was reasonable, and letting me choose the music now and again. I'm convinced I would have gone crazy without you both.

I am grateful for the time that Jonathan Jones has spent with me sorting out sensors and NMR time, and I'd like to thank Simon Benjamin for helping me sort out my thoughts and for getting me going with Povray. Importantly, I doubt I could have accomplished anything in the CAESR lab without Jeff Harmer's amazing support. I also would like to thank all the other users of the CAESR facility for being flexible with spare days and cold resonators in the morning and generally being great people. I'd like to thank Bruker Germany for working diligently to send us back whatever's been broken. I appreciate IQC and Ray Laflamme for getting me where I am, for the Clarendon Fund for financially supporting this work, and to the Magdalen MCR community for lots of brunches, liquid lounges and great discussions.

To the best of the best: I thank James, Hugo, Vicki, Pavel, and the rest of the clan for all the spare evenings regardless who was in the country, for boardgames, wine, whisky and Terry Pratchett. I'd like to thank all the hockey ladies for the all those loud late nights on ice, with a special thank you to my captains and Gypsy.

I owe absolutely everything to my family — I couldn't have gotten here without your support and love. I miss you all a great deal, and thank you for the care packages and pictures. Jillian — thank you so much for exploring the whole world with me year after year — you brought me so much closer to home because of it.

Lastly, and above all, I thank John Dunn, for the amazing hugs and stupid sense of humour, for being around well before and well after this whole doctoral thing, and for following me across an ocean. I love you more than you know.

CONTENTS

> “No reasonable definition of reality could be expected to permit this.”
>
> *Albert Einstein,*
> *on entanglement [EPR35]*

§ 1. Introduction

Modern society has a voracious appetite for computational power, and our current resources are able to efficiently process and store an astonishing volume of data. Yet some problems still remain computationally *hard*: they have no known efficient solutions within our current information-processing framework. Some such problems are so important that they are being attempted using classical computing techniques anyway; supercomputers worldwide are dedicating their resources to hard problems including data-searching, simulating large chemical (or quantum) systems, predicting material properties and cracking encrypted codes.

The simple idea that we cannot yet efficiently simulate quantum systems invites some natural questions. Does quantum mechanics possess inherently more computational power than the classical sort? What sorts of ‘hard’ problems could be processed efficiently if we were able to harness the power of quantum mechanics? Indeed we have evidence to suggest that *quantum information* is more powerful than classical information; each of the example ‘hard’ problems listed above seem to have a far more efficient solution available on a quantum computer [Jor11]. However the growing quantum information community has yet to conclusively resolve exactly what makes a given ‘hard’ problem easier with a quantum computer [NC00], how much of a quantum computer is necessary for enhanced efficiencies [Mer11], and which other ‘hard’ problems may benefit from a quantum efficiency boost [Aar08]. What is known, however, is that there is currently no other known alternative to efficiently attack these important hard problems, and so the global race towards a prototype quantum computer is underway.

Woven through each of these discussions has been the notion of *entanglement*: the nonclassical state of a system that cannot be described in terms of its parts alone. The earliest attempts at building a quantum computer encoded quantum information in the spin degree of freedom of a large collection, or *ensemble* of nuclear spins which, for reasons which will be discussed in this chapter, often cannot be entangled. This approach is at odds with the finding that entanglement is critical for what is thought to be the most powerful known form of quantum computation, namely *pure-state* quantum computation. These two developments raises two interesting questions: Can ensemble entanglement be created and controlled using spins, resolving this concern? Secondly, can lesser forms of entanglement still exhibit significant advantages above and beyond classical resources? To appreciate the answers to these and other questions once must first understand the fundamental unit of quantum information — the qubit.

1.1 Representing quantum information

Quantum mechanics' computational potential arises from two simple ideas. The first is the superposition principle. In our familiar classical picture we are comfortable with the idea of exclusive stationary states — a binary '0' or '1' bit, or a coin having landed heads or tails. In quantum mechanics, however, exclusive stationary states (that is, eigenstates of a Hamiltonian) can be occupied simultaneously. More rigorously, the Schrödinger equation is linear, which is to say that if it supports multiple eigenstates (denoted by 'kets' such as $|0\rangle$), it also supports any complex linear combination built out of those solutions. In quantum mechanics, superposition is not a statement about uncertainty — a coin in superposition of 'heads' and 'tails' is not simply balanced precariously on its edge, rather it is both heads and tails at the same time.

The second key computational feature of quantum mechanics is the way that state spaces are combined. In a classical setting, the total state space is given by the Cartesian product of the individual spaces. Quantum mechanics develops the free cartesian product into a truly bilinear object via the tensor product of state spaces. If systems A and B are in eigenstates $|0\rangle_A$ and $|0\rangle_B$, they can be described simultaneously as a state $|0\rangle_A \otimes |0\rangle_B = |00\rangle_{AB}$. This gives rise to entangled states which cannot be described in terms of their constituent parts.

In the context of information processing, the superposition principle across tensor product spaces allows for highly parallel processing. Given that a classical bit can take on an exclusive $|0\rangle$ or $|1\rangle$ state, a quantum bit or *qubit* can take on any value $\alpha|0\rangle + \beta|1\rangle$ for $\{\alpha, \beta\} \in \mathbb{C}$; both $|0\rangle$ or $|1\rangle$ can be processed simultaneously. A two-qubit pure state could be described by the amplitude and phase relationships of its four eigenstates: $\gamma_{00}|00\rangle + \gamma_{01}|01\rangle + \gamma_{10}|10\rangle + \gamma_{11}|11\rangle$. One way to represent this information is in the form of a matrix, which is known as a system's *density matrix.* If one has access to a quantum system's density matrix, often one is able to infer many properties of the system such as whether or not it is entangled.

To describe an arbitrary pure superposition state of N qubits (therefore 2^N eigenstates), one would in principle need to know the complex coefficients for every term in the superposition. This implies an exponentially larger computational space is required to describe an individual state than in a classical framework, and it is for this reason that quantum systems cannot be simulated without a quantum computer. At the same time, this is thought to be the source of quantum mechanics' enhanced processing power.

Unfortunately a measured quantum state cannot report being in superposition. Wavefunction collapse, the computational counterpoint to the superposition principle, forbids us from ever observing a coin having landed simultaneously heads and tails[1]. When a measurement of a quantum particle is made, it reveals only a single eigenvalue, collapsing any superpositions into strictly those consistent with the measured eigenstate of that particle. To be precise, this does not collapse the entire wavefunction — this only collapses the components of the system where information has been extracted. Seen in this way, measurement is simply another valid quantum operation at our disposal.

The probability that a particle collapses into a particular eigenstate is a function of its amplitude: for a two-level state $\alpha|0\rangle + \beta|1\rangle$, the probability of measuring an eigenvalue corresponding to the state $|0\rangle$ is $|\alpha|^2$, and the sum of all probabilities is one. Hence if one were to prepare many identical copies of a given quantum state and take enough measurements one could estimate the values of $|\alpha|$ and $|\beta|$ immediately prior to collapse. This is how quantum states are read out — either as a *temporal ensemble* (repeating the process many times) or *spatial ensemble* (preparing many identical systems simultaneously).

---

[1] For completeness, it should be noted that there are alternative interpretations of quantum mechanics that do not subscribe to wavefunction collapse, see Reference [Sch95] for further discussion.

1.2 ENTANGLEMENT

A quantum superposition state describing more than one physical item is in an *entangled* state if the physical items are so highly correlated that they cannot be described separately. If a state is not entangled, it is called separable. As examples, the separable state $|00\rangle_{AB}+|01\rangle_{AB}+|10\rangle_{AB}+|11\rangle_{AB}$ can be separated into the state $(|0\rangle_A+|1\rangle_A)(|0\rangle_B+|1\rangle_B)$, whereas the pure entangled state $|00\rangle_{AB}+|11\rangle_{AB}$, cannot be similarly factored.

Pure states, including the above examples, are ideal quantum states which can be described in terms of kets, however the idea of entanglement can be applied to the more general *mixed* form of quantum states. Both the purity and the mixedness of a state can be calculated from the state's density matrix. An entangled state cannot be arbitrarily mixed; there is a lower bound on the purity necessary to generate an entangled state [WNG$^+$03].

Occasionally the dynamics of a system are such that one can choose to separate a state into a highly pure component and a highly mixed component and disregard the highly mixed component. Under certain conditions this is known as the *pseudopure approximation*, which is the scheme often adopted with very mixed nuclear spins controlled and measured with Nuclear Magnetic Resonance (NMR). When working under the pseudopure approximation, one must carefully consider the entire quantum state before classifying a state as entangled or separable. The pure component of the state could be a maximally entangled state, however the state as a whole could be separable. A separable state that is entangled in the pseudopure approximation is known as a *pseudo-entangled* state, and is insufficient for tasks which require true entanglement, such as teleportation, measurement-based quantum computation and the most secure forms of quantum cryptography [NC00].

A state's entanglement or separability is defined with respect to a particular partition of subsystems, such as the partition between qubits A and B given above. In general a state's separability along one partition is unrelated to its separability along another. This indicates that entanglement is very strongly dependent upon the partition chosen. Specifically, the eigenbasis of a system's Hamiltonian does not necessarily indicate the proper partition to determine if a state is entangled or not. Strictly speaking, entanglement is considered with respect to the basis of the individual separate particles [AOV08]. This implies that eigenstates — even ground states — could themselves be entangled.

Ground-state entanglement is ubiquitous in nature. Electronic spin singlets in orbitals about an atom are naturally maximally entangled [Sak93], however such spins are not experimentally distinguishable and so the non-classical correlations contained between them cannot be used [Hei02]. Many other such examples exist, including ferromagnets [WMD05], Bose-Einstein Condensates [BDR$^+$07] and any other coupled multipartite system whose energy levels' degeneracy cannot be lifted. Accessible entanglement, that is, entanglement between multiple separately addressable entities, is the sort of entanglement that can be used to demonstrate the sort of non-classical behaviour Einstein believed "no reasonable definition of reality could be expected to permit" [EPR35].

In trying to determine a test to dismiss the *nonlocal* predictions of quantum mechanics, wherein two spatially separated particles cannot be described individually, John Stewart Bell derived an inequality [Bel64] that, if violated, showed the existence of correlations stronger than those allowed by classical mechanics. This inequality was later violated using entangled states by Stuart Freedman and John Clauser [FC72] and then more conclusively by Aspect *et al.* in 1981 [AGR81]. Although controversial in its philosophical implications, the physical result was clear: entanglement could be created and measured in nature[2]. Entangled states have since been shown to be an essential resource for quantum teleportation [BBCe$^+$93], the strongest forms of quantum cryptography [CLL04] and the speedup potential of pure-state quantum computation [JL03].

1.2.1 ENTANGLEMENT MEASURES, TESTS AND WITNESSES

Although the formal definition of entanglement (covered in Section 2.3.1) is unambiguous, it is hard to determine the degree of entanglement present in a general quantum state, or even if it is entangled at all [HHHH09]. There is no known 'litmus test' that definitively

---

[2] Entanglement is a broader concept than nonlocality; although all the states that violate the Bell inequality are entangled, the maximally entangled Werner state does not violate any test of nonlocality [Wer89], which is ultimately what a Bell inequality tests for.

verifies if a general quantum state is entangled, nor a consensus on which measure is best to use in different situations. There are a number of entanglement tests that are either sufficient or necessary — however the few that are both sufficient and necessary are very limited in scope. It is therefore important to navigate such entanglement measures carefully. A few important entanglement measures will now be introduced alongside their benefits and limitations.

Bell's pioneering inequality was later developed into more robust 'CHSH' inequalities [CHSH69], and multipartite inequalities [WW01], which were used to demonstrate strong forms of nonlocality for the purposes of ruling out hidden variable models of reality. Each of these entanglement tests are sufficient but not necessary: there exists bipartite (and multipartite) pure entangled states that do not violate any Bell inequality [ZBLW02]. Other tests are therefore needed.

In 1996, a necessary and sufficient entanglement test was developed independently by Peres [Per96] and Horodecki [HHH96] for small-dimension systems, pure and mixed alike. This test, often referred to as either the Negativity condition or Positive Partial Transpose (PPT) condition, involves an algebraic manipulation of a state's full density matrix to determine if it is entangled, and is given explicitly in Section 2.3.1. The idea relies upon a subsystem transposition that preserves the non-negative eigenvalues of each subsystem, caracteristic of physical density matrices, but not necessarily those of the composite system as a whole. Such a map acting upon an entangled state would produce unphysical density matrices, indicated by negative eigenvalues. Even though the partial transpose is basis-dependent, the resultant eigenvalues are not; it is the partition which determines the state's separability. This is a sufficient and necessary computable test for 2x2 and 2x3 dimensional two qubit systems, but is only a sufficient condition for larger-dimensionality, multiqubit systems. Of course to use such a test one must have reconstructed the entire density matrix of the quantum system. Any process able to faithfully reconstruct a quantum state's density matrix is known as *quantum state tomography*, which is covered in detail in Chapter 6.

Alternatively there are non-algebraic measures such as *concurrence* that aim to quantify the amount of entanglement within a system numerically [Woo98]. A concurrence value of 0 indicates a separable state and values up to 1 indicate the existence of entanglement. It is a necessary and sufficient test for the entanglement of two-qubit mixed states. Pure and mixed-state multi-qubit generalisations (of which there are at least three) are non-algebraic and can be complicated to compute [MKB05]. Calculating the true concurrence of mixed state involves finding a global minimum, necessitating an optimisation step which can give both upper and lower bounds on the true concurrence value [MKB04]. All entangled states have a positive concurrence by construction [Woo98], however the precise value and its estimate range depend on the type of mixed-state generalization [HHHH09]. These estimates offer a practical, but inconclusive, approach to the problem of quantifying entanglement.

These types of sufficient (but not necessary) entanglement identifiers are members of a more general collection called ‘Entanglement Witnesses’ [Ter00]. Every entangled state has a ‘witness’ operation that can detect it, and often these operations do not require full knowledge of the state’s density matrix. Unfortunately they need to be constructed anew for each test, and such construction can be quite involved [DPS02]. The general method for generating such witnesses experimentally has been explored [Tot05]. However, for known states, witnesses can be used to efficiently detect entanglement.

1.2.2 Experimental demonstrations

The first experimental demonstrations of entanglement were those used to violate Bell’s inequalities. Much work has been done since to demonstrate the creation and control of entanglement in a variety of quantum information systems; below a few notable experimental demonstrations are listed. Each of these demonstrations have in some form implemented superposition-generating operations and conditional operations.

From a known starting state, say $|00\rangle_{AB}$, one can form the entangled state $|00\rangle_{AB} + |11\rangle_{AB}$ through two quantum operations. The first operation forms a superposition with one of the qubits through what is known as a *coherence*-generating operation, and an example of this transforms the initial state $|0\rangle_A |0\rangle_B$ into $(|0\rangle_A + |1\rangle_A) |0\rangle_B$. The second quantum operation is a *conditional* operation which changes the state of one qubit depending upon the state of the other. An example conditional operation is known as the

CNOT operation and transforms the state $|0\rangle_A |0\rangle_B + |1\rangle_A |0\rangle_B$ into the pure entangled state $|0\rangle_A |0\rangle_B + |1\rangle_A |1\rangle_B$. The formal definitions of these operations are not strictly necessary here but will be covered in Chapter 2.

Historically the first experimental realisation of an entangling CNOT operation is due to Monroe *et al.* 1995 [MMK$^+$95]. This was implemented between two degrees of freedom (spin and vibration) in a single trapped ^{9}Be$^+$ ion. Although this was an 'entangling' operation, no entanglement was generated as it was not applied to a superposition state. This was remedied by Turchette *et al.* in 1998 [TWK$^+$98]. It was this same basic approach that led to successful eight-atom entanglement in 2006 [HHR$^+$05].

The first pseudo-entangled state was generated in 1998 by Michele Mosca and Jonathan Jones [JM98], and also independently by Lieven Vandersypen and Isaac Chuang [CVZ$^+$98] using liquid-state Nuclear Magnetic Resonance (NMR). Immediately afterwards, Braunstein *et al.* considered these experiments and constructively showed that all few-spin systems in the highly mixed NMR environment are completely separable [BCJ$^+$99]. This was determined through the calculation of a minimum qubit purity below which entanglement cannot exist.

Under the standard NMR pseudopure initialisation scheme, the polarisation of the initialised state scales as $N/2^N$ [CFH97], and this implies that with room-temperature nuclear polarisations NMR is not able to surpass the threshold given in Reference [BCJ$^+$99]. This leaves NMR facing three paths: one, the adoption of hybrid or niche magnetic resonance techniques to satisfy these polarisation requirements for pure-state quantum computation, two, the pursuit of the DQC1 computational model covered in Section 1.3.1 which shows some quantum advantages with vanishingly little entanglement, or three, the development of quantum control techniques to be adopted by other architectures in the future. All three directions have been explored; notably, a chemical process was used to highly polarise hydrogen spins for a single-shot form of entanglement with limited scalability [ABC$^+$04], and increasingly complex control methods have been developed which have allowed for the creation and control of a twelve-spin pseudo-entangled state [NMR$^+$06], and the simulation of an entangled Heisenberg spin chain [PDS05].

Neumann *et al.* avoided the purity limitations of ensembles by working with single nitrogen-vacancy (NV) centres in diamond [NMR$^+$08]. Single spins can be individually measured to collapse their state into a pure state. The electronic state associated with the NV was prepared, manipulated and measured optically, after which it was entangled with the local spin-active nitrogen nucleus.

Superconducting qubits have also been used to create and measure entanglement. Steffen *et al.* accomplished this task in 2006 with two phase qubits. Although quantum state tomography was performed, only the *fidelity*, a measure of two states' indistinguishability, between the experimental and target density matrix was used to justify the nonseparability of the state [SAB$^+$06]. The reported fidelity was 75%, but state fidelity is not enough to determine the existence of entanglement[3].

Entanglement generation can also be accomplished using adiabatic principles. Explicitly shown by Unanyan [UVB01], entangled states can be generated by modifying a ground state adiabatically. In fortunate situations, the initial and target Hamiltonians can even share eigenstates — although in practice their eigenvalues differ. The key point is exploiting anti-crossings in the adiabatic evolution so that, with some probability, what started as a ground state evolves into an entangled state. Unanyan's scheme has a maximum fidelity of 50%. These methods have been used experimentally in atomic-photonic systems by Lazarou and Garraway [LG08].

A *squeezed* quantum state is one that saturates the Heisenberg Uncertainty Principle in two of its conjugate variables [Wal83]. Both the position-momentum of ions and phase-frequency variables of photons have been successfully squeezed. The squeezing can be localised in one variable at the expense of the other. These two modes are said to be entangled in the continuous-variable model (where the two level qubit is replaced by two conjugate variables) if this conjugate behaviour belongs to different systems [JKP01]. This was first realised in 1999 by Hald *et al.* and in 2001 by Julsgaard *et al.* to polarise, and then entangle, spin ensembles in a cavity [HSSP99, JKP01]. Gaussian light was squeezed such that it was very well defined in frequency at the expense of its phase. It was directed to interact with two distinct ensembles of ions in a cavity. To determine

---

[3] Furthermore, there are two common definitions of state fidelity [Joz94, NC00], and the more generous measure was chosen in this instance. In the alternative definition, the measured fidelity was 56%.

if entanglement was present between the two ensembles, a continuous-variable version of the CHSH inequality was used as an entanglement witness.

In Chapter 7 I explore the possibility of generating spin ensemble entanglement using electrons bound to ^{31}P donors in ^{28}Si controlled with Electron Paramagnetic Resonance (EPR). I further these investigations by generating ensemble pseudo-entanglement between nuclear spins using the polarisation and fast entangling operations provided by a transient electron spin.

1.3 COMPUTATIONAL SPEEDUP

A computational speedup is determined by the relative amount of resources required to complete a problem, counted in the number of time steps or number of physical resources (such as bits or qubits). An algorithm is said to be of polynomial time if the number of time steps it takes to complete the algorithm is bounded by *poly(n)*, a polynomial expression in n, the size of the algorithm's input. To say that a quantum computer supports an exponential (or *superpolynomial*) speedup indicates that the most efficient known algorithm on a classical computer is of exponential time (bounded by $2^{poly(n)}$) whereas an equivalent known quantum algorithm is of polynomial time. Shor's factoring algorithm and linear system manipulations (including matrices and quantum system dynamics) are notable examples in a long list of algorithms boasting exponential speedups using quantum information [Jor11]. Algorithms of exponential time are considered computationally *hard* or intractable, whereas solutions calculated in polynomial time are considered efficient, and so much work has been devoted to identifying the power behind quantum computers' exponential speedup [Ved10].

Broadly speaking it is the ability to explore the entire Hilbert space of states that allows quantum computation its exponential speedup. An algorithm on any number of qubits which is restricted to pure states with *Schmidt rank* N — defined to be superpositions between at most N eigenstates — does not yield an exponential boost in efficiency[4] [JL03]. The speedup potential scales with the maximum superposition size, not the number of

---

[4] The same is true for mixed states, where a given mixed state's density matrix is said to have Schmidt rank N if its nonzero elements are restricted to diagonal blocks of at most width N.

qubits. Entangled states form a large proportion of N-term superpositions; in fact, the number of separable states in a pure N-term superposition is relatively small [Sza05], and by symmetry the same could be said for separability along *any* partition of the system. A consequence of this is that entangled states whose Schmidt rank scales with the number of qubits (*unbounded* entangled states) are necessarily present to achieve exponential speedup using pure-state quantum computers, however other states of Schmidt rank N are present as well [JL03].

One can attempt to isolate precisely which states give rise to computational speedup by determining which quantum algorithms (and the states they use) can be simulated on a classical computer with only a polynomial resource overhead — this is said to be an *efficient simulation.* A pure separable state of N qubits can be described by $2N$ real numbers, which can be simulated efficiently using a classical computer [JL03]. Therefore the only remaining pure states which avoid efficient simulation are entangled states, and it is for this reason that some subset of entangled states give rise to pure-state quantum computers' computational speedup. Interestingly, no similar relationship between entanglement and the computational speedup potential of mixed quantum states has been identified.

Moreover, the Gottesman-Knill theorem states that even some pure entangled states can be simulated efficiently [NC00].

Theorem 1 (Gottesman-Knill theorem)**.** *A quantum algorithm using only the following elements*[5] *can be simulated efficiently on a classical computer:*

1. *Preparation of the system into a pure basis state*
2. *Pauli* π *and* $\frac{\pi}{2}$ *operations plus two-qubit CNOT operations*
3. *Measurements in the chosen basis*

The definition of Pauli operations are given in Section 2.1.2, however we can immediately conclude that although entanglement may be necessary for quantum computational

---

[5] Such algorithms are known as *stabilizer algorithms*, and examples include entanglement distillation and quantum error correction algorithms.

speedup it is certainly not sufficient. This line of thought, in combination with the observation that mixed states can have unbounded Schmidt rank as well, led to the discovery of mixed-state algorithms which support an exponential speedup with only vanishingly little entanglement.

1.3.1 DQC1

Deterministic quantum computation with one bit (DQC1) is the name given to the first identified model of computation which supports exponential speedup with asymptotically vanishing amounts of entanglement [DSC08]. The DQC1 model works off the basic idea that only a single pure qubit is necessary to extract information about an arbitrary quantum operation which acts on any number of mixed qubits. The key is to apply the quantum operation conditional upon the state of the pure qubit; as shown in Appendix B this can reveal information about the quantum operation that cannot be deduced efficiently using only classical resources. DQC1 has been shown to support an exponential speedup in a number of algorithms including the estimation of Jones polynomials [SJ08b], and determining the partition function of spin models like the Ising model [Lid04]. It is not suspected to be able to perform Shor's algorithm or many of the other exponential speedup algorithms possible on a pure-state quantum computer [SJ08b], although this has yet to be proven.

The DQC1 model contains entanglement, however the amount of entanglement does not scale with the number of qubits of the system, and so it has been suggested that entanglement is not the driving force behind DQC1's exponential speedup capabilities. Quantum *discord* was a concept introduced to measure the non-classical correlations of a state, of which entangled states form a subset, and has been proposed as the driving power behind separable states' speedup [DSC08]. The argument for this view is that, unlike entanglement, discord scales with the number of qubits in the DQC1 model. It should be noted that discord is present in nearly all quantum states [FAC$^+$10], that it varies under local operations [DVB10] and unfortunately is not *faithful*: it does not vanish if and only if the state only has classical correlations [PGA$^+$11]. It is an open question if discord (or some other measure of nonclassical correlation) merely accompanies, or is the power behind, separable states' exponential speedup [DVB10, PGA$^+$11].

On the other hand, the Schmidt rank of the states used in the DQC1 model does scale with the number of qubits, which is consistent with the power of quantum computation being insistent upon unbounded Schmidt rank states in general. In the case of pure states, an unbounded Schmidt rank coincides with unbounded entanglement, and in either case high-fidelity entangling operations are necessary.

1.3.2 COMPLEXITY

Determining the precise computational limitations and capabilities of a given set of resources is the subject of a field of research known as *computational complexity.* The set of problems that can be solved in polynomial time with a classical computer is the complexity class P. P is a subset of BQP, the set of bounded-error quantum algorithms solvable in polynomial time. In between these two classes lies DQC1, the set of BQP problems that can be solved using the DQC1 model. Encompassing each of these classes is the complexity class PSPACE: the set of problems that can be solved with a polynomial amount of resources but with infinite time [Wat09].

Shor's factoring algorithm gave support to the idea that BQP extends beyond P [Sho94], and research into Jones polynomials lends credit to the idea that DQC1 extends beyond P as well [PMRL09]. Hundreds of complexity classes exist and a vast body of literature examines classes' relationships to one another [Wat09]. Some classes contain only isomorphic problems; to find an efficient solution to a single problem would immediately reveal efficient solutions to all members of the class. For the four classes introduced above it has been rigorously shown that $P \subseteq DQC1 \subseteq BQP \subseteq PSPACE$ (See Figure 1.1).

Computational complexity theory provides an elegant categorisation of resource requirements, however it has proven difficult to show that a given algorithm — or even any algorithm — is impossible to accomplish with polynomial resources. Notably, it has yet to be shown that $P \neq PSPACE$. The standard opinion [Hem02] is that $P \neq PSPACE$, however until this has been shown it is possible, however unlikely, that quantum informa-

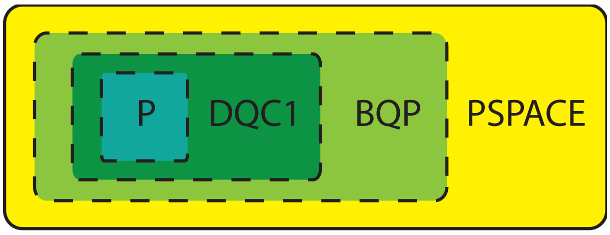

Figure 1.1: **Basic complexity classes underpinning the pursuit of quantum information.** The polynomial class of problems, labeled P, encapsulates what can be currently computed efficiently. DQC1 and BQP exploit quantum mechanics to seemingly go beyond these bounds, which are themselves contained in the set of problems solvable given infinite physical processing power, labeled PSPACE. The dashed-line boundaries indicate that it has not been proven that any these subsets are strict.

tion might be no more powerful than classical information[6].

Although this fundamental fact remains unresolved, it remains the case that a means of achieving exponential speedup has been identified by exploiting quantum mechanics. Furthermore, the only scheme known to be able to support all of these computational advantages is a pure-state quantum computer. In any implementation of such a device one would need the ability to explore the entire state space of the system, including the generation of entangled quantum states.

1.4 QUANTUM METROLOGY

In addition to the impressive speedup potential quantum mechanics is able to provide for computation, quantum mechanics can contribute towards the enhancement of other technologies as well. The highly sensitive superpositions of a quantum state that are often easily corrupted by the local environment can be used as a tool for detecting small environmental changes.

The limiting Heisenberg Uncertainty Principle states that the uncertainty of two conjugate variables, such as position and momentum, or time and energy, cannot be jointly

---

[6] If P=PSPACE, we would be able to efficiently simulate any problem we could conceive of giving rise to “godlike” computational powers [Aar08].

known perfectly; their uncertainties' product must exceed $\hbar/2$. In the context of ensemble measurements, this relation remains true and the uncertainty of one variable can be minimised at the expense of the other. With N copies, a variable A can have its uncertainty reduced by a factor of N if the uncertainty of the conjugate variable B is increased by the same factor. This scaling of sensitivity, according to $1/N$ for N particles, is termed *Heisenberg scaling*. Certain pure entangled states are able to satisfy this scaling in resources. In contrast, the standard act of averaging many runs to improve a measurement has a sensitivity which scales as $1/\sqrt{N}$ for N particles, and this reduced scaling of resources is considered the *standard quantum limit scaling*. Of course, one need not saturate the Heisenberg limit to observe a Heisenberg scaling of resources, and as is the case with the DQC1 architecture, these advantages need not necessarily rely upon entanglement to outperform classical limitations, although such a relationship is often claimed.

The idea of using quantum resources to improve the sensitivity of measurements can be applied to a variety of situations. By reducing the uncertainty in position, the resolution of lithography can be improved [KBD04]. By squeezing the phase-frequency characteristics of a beam of photons, one can minimise the uncertainty in the path travelled and improve the distance-travelled sensitivity of an interferometer [GZN$^+$10]. The enhanced phase sensitivity of light can also be used to enhance the sensitivity of detectors searching for gravity waves [KLM$^+$01a]. Similarly, by correlating multiple photons into an entangled quantum state known as a NOON state, the sensitivity of an interferometer can demonstrate Heisenberg scaling [Yur86]. Spin qubits can also form suitable NOON states, which can act as sensitive magnetometers [JKF$^+$09]. A precise calculation of resources can determine what advantages a given quantum-enhanced measurement has over its classical counterpart, if any[7], and can inspire modifications to the parameter estimation procedure that further enhances the sensitivity of the measurement.

In Chapter 4, I discuss the practice of using an ensemble of spins at room temperature to detect small shifts in the magnetic field. I also introduce methods to improve upon this

---

[7] Some recent work distinguishes between nonclassical enhancements and a Heisenberg scaling of resources, particularly in the presence of qubit loss [TPS$^+$11].

basic parameter estimation procedure to go beyond the $1/\sqrt{N}$ standard quantum limit scaling using unambigously zero entanglement.

1.5 Spins as qubits

Spatial ensembles of paramagnetic spins are excellent qubits to act as a testbed for many quantum control techniques. The two states of a spin that act as the two eigenstates of the qubit are the aligned and anti-aligned states of the spin with respect to a background magnetic field. These states are often denoted by $|\uparrow\rangle$ and $|\downarrow\rangle$, and superpositions of these two states can be created and controlled with pulses of electromagnetic radiation. Spins have been investigated in a wide range of environments. The nuclei in a molecule can act as qubits and be controlled to a high degree even if the molecules move freely in a liquid (such as crotonic acid [KLMT00]) or are frozen as a solid [Mor05]. Some molecules also have unpaired electrons that can be used as qubits (such as atoms incarcerated in C_{60} fullerenes [BAB+06]). Larger systems can collectively have a spin orientation such as quantum dots [NKN07], as well as molecular magnets [BGM08]. Single crystals or polycrystalline samples can also contain nuclear spins suitable as qubits [Wra10]; crystal defects (such as nitrogen-vacancy centres in diamond [DH76], and donors in silicon [FYPM54]) may also have an associated electron spin that can be manipulated in tandem.

Spins have several important strengths and a few disadvantages compared to other candidate qubits. The three principle strengths of spin qubits are their lifetime characteristics, their control characteristics and the fact that these characteristics are highly reproducible.

Eigenstate superposition states are nonequilibrium states which cannot exist indefinitely. After a time, nonequilibrium quantum states relax into the thermal equilibrium state and this amounts to a corruption or loss of quantum information. This timescale on which these relaxation processes occur can vary significantly — they can be shorter than nanoseconds or longer than minutes — and for the purposes of preserving quantum information over the course of an algorithm (or as a quantum memory [MTB+08]), longer times are better. Related to this is the time it takes to perform individual quantum operations; the benefits of a qubit with a ten second lifetime are mostly lost if the time it takes to perform a single quantum operation is on the order of a few seconds. Fortunately, spins are both long-lived (in particular, electron-nucleus donor pairs in silicon each have lifetimes exceeding seconds [TTM$^+$11, The11]) and can be manipulated very quickly (on the order of nanoseconds [MTA$^+$06, FDT$^+$09]).

The quality of available quantum operations plays a critical role in the assessment of qubits. In addition to the requirement that many quantum operations should be possible within the lifetime of the qubit, the quality of these operations must be high enough to not corrupt the quantum information and hence the result of the algorithm. Errors cannot be completely removed, however quantum error-correcting algorithms exist which are able to correct for computational error rates of up to nearly 1% per operation [RH07], depending upon the qubit architecture. The quality of the operations used to manipulate the qubits are therefore of paramount importance, and on this front spins have performed admirably. Techniques exist which are able to characterise this rate of error, and through a ‘randomised benchmarking’ procedure nuclear qubits controlled with NMR have displayed an error rate of 1.3(1) x 10^{-4} per gate [RLL09], which is sufficient for error-correcting algorithms. This high degree of control extends similarly to multiple qubit operations, which has allowed for advanced demonstrations in quantum control using magnetic resonance including the pseudo-entanglement of twelve spins [NMR$^+$06], the realisation of Shor’s factoring algorithm on a small number of qubits [VSB$^+$01] and algorithmic cooling [BMR$^+$05], which is discussed more in the next section. Electron qubits have also demonstrated high fidelity control [MTA$^+$05a] and this degree of control has allowed for the experiments in Chapter 6 and Chapter 7.

The characteristics intrinsic to an individual nucleus or electron are as fundamentally reproducible as the particles themselves. The environment in which the spin resides can of course vary from qubit to qubit, and minimising the variation of such inhomogeneities improves the uniformity of the qubits [KSM$^+$03, BNT$^+$09]. Spin qubits in homogeneous environments do not need to be individually tuned or calibrated: they can be controlled and measured as a spatial ensemble and the strength of couplings between qubits are predetermined by their local chemistry. Such ‘user-friendly’ characteristics contrast strongly with the other principle current competing approaches, including quantum dots, superconducting circuits, and trapped ions, which either need to calibrate individual qubits and/or re-calibrate all qubits (or the instruments controlling them) very often for high-fidelity operation [MGF$^+$10, Cho10, KLR$^+$08]. Although this uniformity is advantageous for the control of ensembles, it is disadvantageous due to the smaller degree of control over the system’s properties. Fortunately, these predetermined properties can be exceptionally attractive in their own right.

Nuclear spins and electron spins have distinct strengths as qubits. Although both are long-lived in suitable systems, nuclear spins generally outlive electron spins due to their reduced couplings to the environment. In the same vein, the direct manipulation of nuclear qubits can be much slower, leading to correspondingly fewer operations within the qubits’ lifetime. Electrons, on the other hand, couple to many different degrees of freedom, including multiple nuclei, photons, phonons and other unpaired electrons (often leading to faster relaxation) and because of their larger wavefunction depend strongly upon the local environment [LS93]. Their interactions need not be isotropic [WF61], they can be excited out of their ground state into higher orbital states [GLvdM$^+$10], and all of these properties can depend strongly on temperature and magnetic field [SJ08a]. In return, electrons provide direct access to nuclei, and in the right environment can offer exceptionally long lifetimes [TTM$^+$11] and very fast control [MTA$^+$06]. Most importantly, at experimentally accessible magnetic fields and temperatures electrons provide the polarisation that nuclei lack for proper qubit initialisation [SBR$^+$11].

Due to the weak energy splitting between the nuclear spin-up and spin-down states, only very small thermal excitations are required to change the spin state of the nucleus, and so at experimentally accessible magnetic fields and liquid-helium temperatures nuclear spins equilibrate nearly evenly as a mixture of spin-up and spin-down [Lev01]. In this setting the nucleus is said to very mixed, or equivalently, weakly polarised. In an ensemble, the net magnetic moment made up of mixture of the spin-up and spin-down states of nuclear qubits is very small, however with a sufficiently large number of spins this net difference can be detected with magnetic resonance techniques [RZMK38]. This poor initialisation is sufficient to develop many spin control methods because the quality of many quantum algorithms can be evaluated equally well when applied to weakly polarised systems [KCL98]. Unfortunately weakly polarised qubits cannot necessarily be considered equivalent in all respects; as discussed throughout Section 1.3, presently there is no known way for mixed, weakly polarised systems to match the potential performance of a pure-state quantum computer [SJ08b]. Fortunately, methods exist which are able to temporarily polarise nuclear qubits well beyond their thermal polarisation.

1.6 Optimal initialisation

Thermal equilibrium need not be the optimal initial state for a given quantum application. In practice there are many ways to initialise a quantum system and these methods can exploit a range of properties. Some of these initialisation procedures depend upon the particular choice of qubit, while others are common to any quantum system.

Universally, the collapse principle of quantum mechanics allows for efficient single-qubit single-shot initialisation. The measurement of a system can only reveal an eigenstate of that system [Sak93], and by recording this information one can either modify the following algorithm accordingly or discard that particular shot in the event that the measured eigenstate does not match the desired initial eigenstate [NC00]. This method is efficient and can result in a known pure state, although relies upon nondestructive, high-fidelity, single-qubit, single-shot measurement which has only recently become experimentally available for a few systems. Quantum dots have reported upwards of 96% measurement fidelity [VLM+10], nuclear spins in NV centres have reported upwards of 92% measurement fidelity through the electron spin [RCB+11], and phosphorus donors in silicon have reported upwards of 90% fidelity measurement through the electron spin [Dzu11].

Common to a number of different qubits, optical means can be used to initialise a system into a nonequilibrium polarisation approaching a pure state. Often these processes use excited levels which do not make up any of the individual qubits' eigenstates, but can be populated from one or more levels which make up the qubits' eigenstates through optical excitation. To preferentially populate a particular qubit eigenstate (and consequently initialise the system), either the excitation itself preferentially selects a particular eigenstate [YSS+09], or the relaxation that follows preferentially populates a qubit eigenstate [RBSH11], and sometimes both processes are selective [CGDT+06]. The rates which describe these two actions can be solved to determine the steady state distribution of populations under such conditions, and depending upon the asymmetry between various rates this initial state can have a significantly higher polarisation than the thermal distribution of populations. Certain spin states can be initialised to a high degree (upwards of 75%) in this manner including nitrogen-vacancy centres in diamond [HSM06] and phosphorus donors in silicon [YSS+09]. A related yet more complicated idea is used to optically cavity-cool trapped ions; an optical resonator can be made to enhance certain frequencies in the emission spectrum of an optically illuminated ion [HHG+97], and the rate at which these optical modes are excited (which cool the ion) balanced with the rate at which other frequencies are scattered (which recoil the ion, imparting heat) determines the ion's temperature [LLVC09]. This list is by no means exhaustive, and different opportunities exist depending upon the particular level structure of the qubits under investigation.

There is another category of cooling mechanisms which exploit internal dynamics, including relaxation processes, to temporarily enhance the initialisation of a multi-qubit state. These approaches involve a transfer of polarisation from a highly polarised qubit to a weakly polarised qubit, such as an electron to a nucleus [Feh56, MF79]. In addition to a simple transfer of polarisation, an asymmetry in relaxation rates can be used to increase the joint polarisation of both systems beyond that of the thermal equilibrium state [SBR+11]. Members of this category of initialisation schemes include 'algorithmic cooling' methods [SMW05, BMR+05] and 'dynamic nuclear polarisation' methods [Ove53, AG78], and a discussion of such techniques using donors in silicon is presented in Chapter 5.

1.7 OUTLOOK

There are a few fundamentally distinct approaches one can experimentally take in working towards the construction of a quantum computer. These approaches are referred to as 'architectures' for quantum computation, and most of these architectures fall into three broad computational classes.

If one were to directly adapt present-day classical computing techniques to quantum information processing, one would arrive at the 'gated' or 'circuit' quantum computing model [Deu85]. The gated quantum computing model relies upon a sequence of quantum operations, referred to as 'gates', applied to a well-initialised set of qubits to process quantum information — this has been the model tacitly adopted in this introductory chapter. Individual gates correspond to some temporary modified environment Hamiltonian (such as a laser or microwave pulse) which apply various quantum operations upon the input state. At the end of this sequence of quantum operations the output state is measured.

A second model, called adiabatic quantum computing [FGG+01], designs a single Hamiltonian to correspond to a full quantum sequence. The state is initialised into a known ground state (often at milliKelvin temperatures) and allowed to find the ground state of the modified Hamiltonian adiabatically. The output, the final ground state, is then measured. This model still requires full control of every individual qubit's Hamiltonian [AvDK+04] and requires unavoidably long timescales to navigate narrow energy gaps adiabatically [JKK+10]. However, it has been shown that with a polynomial overhead in time, this model is equivalent to a gated quantum computer model [AvDK+04], and may be easier to implement experimentally.

There are architectures with the potential to further reduce the experimental demands necessary for a successful demonstration. The result of the measurement after a partial collapse can give insight into how the remaining quantum information has been transformed by the measurement [Par70]. This implies that measurement itself has computational power: an idea that truly distinguishes quantum computation from classical computation. This observation has given rise to quantum teleportation [BBCe+93] and measurement-based quantum computing [RB01, BR01, VPM+07, WRR+05]. This approach initialises its qubits into a particular entangled state (independent of which algorithm is to be applied), and then applies a sequence of measurements as a sequence of quantum operations, leaving the output in the qubits not yet measured. The final output can then be read as usual. This approach largely transforms the difficult problem of manipulating and maintaining many qubits in arbitrary states into one of creating a single entangled state and performing sequential measurements informed by previous measurement results. The creation of a large entangled state cannot be avoided in this architecture; although the application of individual sequences may be easier with measurement-based quantum computation, this generation of entanglement is necessary for this approach to work.

The formation of a quantum state suitable for measurement-based quantum computation can be done in a few different ways [AL04, KLM01b, CFBK07], and one example of this involves the consumption of local entanglement to form nonlocal entanglement [BR05]. Parity measurements of two qubits can be used to form an entangled quantum state between qubits that have never interacted; this concept goes by the name *entanglement swapping* and has been studied extensively [BBCe+93, ŻZHE93, Per00] and verified experimentally [PBWZ98, YCZ+08, BPM+97] with photons. If one were to start with two entangled qubit pairs in the state $(|00\rangle + |11\rangle)_{A_1,B_1}((|00\rangle + |11\rangle)_{A_2,B_2}$, one can perform a joint parity measurement upon the two A qubits. If the parity test reveals that the A qubits share their spin state, the B spins are left in the state $((|00\rangle + |11\rangle)_{B_1,B_2}$, and if the parity measurement is negative the B spins are known to be in the other Bell state $((|01\rangle + |10\rangle)_{B_1,B_2}$ [NC00, NKL98]. The result of the parity measurement can be used to indicate which local single-qubit manipulations would be necessary to obtain any desired maximally entangled state [CG99, Eng05], possibly scaling up to a large cluster state suitable for measurement-based quantum computation [BR05]. This possibility makes the generation of electron-nucleus entanglement all the more attractive.

These approaches can be combined; adiabatic means can be used to apply individual gates [Pow58], and gates can be used to prepare the entangled state suitable for measurement-based quantum computation [KSW+05, Blo08]. These computational architectures do not specify what physical system makes up the qubit — they could include spins, superconducting qubits or any other suitable two-level system. Remarkable progress has been made towards the construction of various architectures with many sorts of qubits over the past fifteen years [NSL+11, PLG10, MWY+11, DRS+10, MPZ+10, FMZ+10, SBM+11, OWC+11], although the small-scale demonstrations performed to date have grown the size of the quantum computer one or two coupled particles at a time [MSB+11, NMR+06, MWY+11]. Scaling up approaches in this way often cannot be done without adding many more unwanted interactions that require simultaneous maintenance. Quantum states can be exceptionally sensitive to environmental variations [WMK$^+$00] and the states required for computational speedup can only survive if such interactions are kept tightly limited [CMB04, KS04]. The key to an elegant, scalable solution may instead lie with inherently parallel constructions using fundamentally identical particles, such as parity measurements of donors in silicon to form nuclear cluster states.

This thesis explores the possibility of generating spin ensemble entanglement, both between electrons and nuclei and between two nuclei in the presence of an electron in Chapter 7. I investigate how pseudo-entanglement can be used to experimentally outperform the classical Standard Quantum Limit for quantum-enhanced metrology through optimal state preparation in Chapter 4. Chapter 5 examines the role of optimal state initialisation and nuclear polarisation strategies in silicon, and the development of techniques for the practice of full density matrix tomography are covered in Chapter 6. Taken together, these results can be seen as an important step towards the development of a spin-based quantum computing architecture.

§ 2. QUANTUM INFORMATION

2.1 QUBITS

This chapter will formally introduce the technical quantum information concepts used in this thesis, starting with the representation of quantum information in the form of a density matrix and the theory of unitary quantum operations.

2.1.1 THE DENSITY MATRIX

A single pure state can be expressed in terms of the (assumedly discrete) orthonormal[1] eigenbasis of the system's static Hamiltonian as:

$$|\psi(t)\rangle = \sum_k \gamma_k(t)\,|k\rangle \tag{2.1.1}$$

where $\{\gamma_k(t)\}_k$ are time-dependent complex coefficients and $\{|k\rangle\}_k$ are eigenstates of the system. This is a vector, and all pure states can be expressed as such. Equivalently, they can be defined as operators:

$$\rho(t) = |\psi(t)\rangle\langle\psi(t)| = \sum_{a,b} \gamma_a(t)\overline{\gamma_b(t)}|a\rangle\langle b| \tag{2.1.2}$$

which permits a natural framework to describe the state of ensembles, as is discussed below. The terms $|a\rangle\langle b|$ act upon any input state like a matrix acts upon a vector, transforming any input eigenstate $|x\rangle$ onto the new eigenstate $|a\rangle$ with an amplitude given by the inner product $\langle b|x\rangle = \delta_{b,x}$.

The sum given in Equation 2.1.2 can be visually presented as a matrix wherein the terms $|a\rangle\langle b|$ correspond to individual matrix positions labelled by $|\text{row}\rangle\langle\text{column}|$. In this

---

[1] Hamiltonians are Hermitian matrices ($\mathcal{H}_{a,b} = \overline{\mathcal{H}_{b,a}}$), which guarantees a complete orthonormal eigenbasis.

presentation,

$$\rho(t) = \begin{pmatrix} |\gamma_1(t)|^2 & \gamma_1(t)\overline{\gamma_2(t)} & \cdots \\ \gamma_2(t)\overline{\gamma_1(t)} & |\gamma_2(t)|^2 & \cdots \\ \vdots & \vdots & \ddots \end{pmatrix} \tag{2.1.3}$$

A quantum system described in this form is called a system's *density matrix*, and encodes all the quantum information available in a state.

A density matrix representation is useful for describing ensembles, because an ensemble of pure states is not necessarily a pure state. A general quantum state is a *mixed* state, which is a convex linear combination of pure states. Mixed states cannot be expressed as a single vector, but density matrices describe them completely and conveniently.

The assumed density matrix basis is the eigenbasis of the Hamiltonian of the system unless otherwise specified. Density matrices are central to understanding quantum states and so a few key properties and definitions will now be listed.

1. The k^{th} diagonal element of a density matrix ρ is $|\gamma_k(t)|^2$ — precisely the probability of measuring an arbitrary state in the k^{th} eigenstate. Therefore the density matrix has unit trace and the diagonal elements are, without loss of generality, real and nonnegative.

2. *Unnormalised* density matrices differ from unit trace density matrices by a constant and are invoked for notational simplicity; a physically valid *normalised* matrix can be recovered by dividing an unnormalised matrix through by its trace.

3. Off-diagonal elements represent the amplitude and phase relationship of a quantum superposition state. The density matrix is Hermitian, meaning that $\rho_{a,b} = \overline{\rho_{b,a}}$, so this phase relationship is unambiguous.

4. If the density matrix is diagonal there are no quantum superpositions in the state; such a state represents classical uncertainty of a system's state.

5. The unnormalised identity density matrix (denoted $\mathbb{I}$) is *maximally mixed* — it is a state of classical uncertainty where all eigenstate outcomes are equally probable.

6. Diagonal elements are called *populations*, distinguishing them from off-diagonal *coherences* which describe the phase information in a superposition state. Some off-diagonal elements, including the anti-diagonal elements, are often called *multiple quantum coherences*, and specific examples are discussed in Section 3.7.

7. Pure states have Trace$[\rho^2] = 1$. This expression is known as the *purity* of a state, which ranges from $(dim(\rho))^{-2}$ (for maximally mixed states) to 1 (for pure states).

8. All mixed states can be written as a weighted sum of maximal $\mathbb{I}$ component and a unique unnormalised density matrix with nonnegative populations.

9. Physically allowed quantum states have Hermitian density matrices with positive eigenvalues. This places restrictions on the amplitudes and the phases of the coherences. Coherences' amplitudes cannot exceed either of their constituent populations' amplitudes, and their phases cannot permit $\langle x| \rho |x\rangle < 0$ for any vector $|x\rangle$.

10. Valid reversible operations upon density matrices must not corrupt the state's Hermiticity or trace: this implies valid reversible operations must be unitary matrices[2]. A unitary operation U transforms a density matrix ρ according to $U\rho U^\dagger$.

Although the idea of mixed states is useful for describing ensembles, it is worth noting that individual particles' states can also take on a mixed form, notably in the context of thermal equilibrium and relaxation processes. The "identity component" of such mixed states is not detected if an experiment is only sensitive to population differences (as is the case with conventional magnetic resonance detection). Additionally, because $\mathbb{I}$ is invariant under unitary operators, the identity component in this context is often termed the *unobservable component* and ignored. Dismissing this (often quite large) component of a density matrix is called the *pseudopure approximation.* This idea forms the basis for a state preparation strategy of the same name: *pseudopure state preparation* is the practice of mixing the thermal state in such a way that the state can be written as a sum of a perfectly mixed identity component and perfectly pure state.

---

[2] Relaxation processes can also be viewed as unitary processes on some larger Hilbert space; they can alternatively be viewed as irreversible nonunitary processes without invoking larger dimensionality.

2.1.2 The Bloch sphere

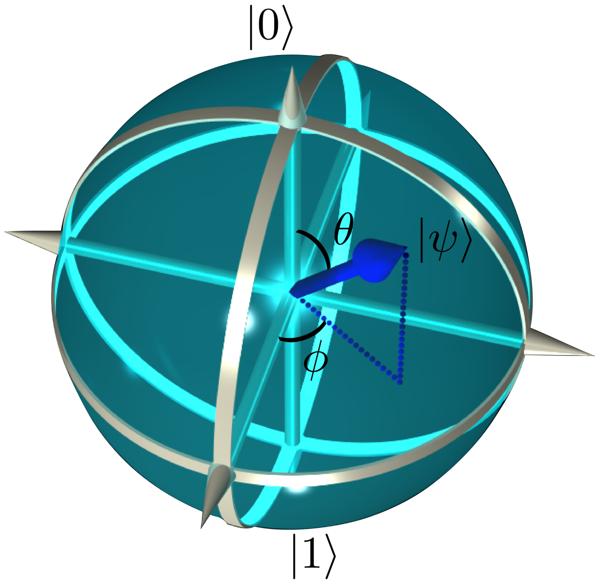

Figure 2.1: **The Bloch sphere.** This graphical representation of a single qubit is helpful in visualising qubit states and operations upon them. A qubit's state can be any vector lying inclusively within the unit sphere, where its coordinates can be given in cartesian (Equation 2.1.4) or polar (Equation 2.1.5) form, where the $|0\rangle$ and $|1\rangle$ eigenstates are along the $\hat{z}$ axis by convention.

Let us consider a two by two density matrix — an arbitrary mixed single-qubit state. This matrix has unit trace and is Hermitian, and so it has only three real degrees of freedom. Therefore this density matrix can be represented as a vector in $\mathbb{R}^3$. A useful and conventional $\mathbb{R}^3$ representation of the set of all possible qubit states is the Bloch sphere (See Figure 2.1). The vector's norm is a function of the state's purity: a maximally mixed state is assigned to the origin, pure states occupy the surface of the sphere (including the $|0\rangle$ and $|1\rangle$ eigenstates), and mixed states occupy the full body of the sphere. The conventional expression in polar coordinates for a pure state are given by:

$$|\psi\rangle = \cos(\theta/2)\,|0\rangle + \exp(i\phi)\sin(\theta/2)\,|1\rangle \tag{2.1.4}$$

Mixed states are often expressed in cartesian coordinates. The cartesian coordinates of a density matrix are found by projecting the density matrix onto each of the three traceless *Pauli matrices*. The 2x2 Pauli matrices form a basis for all complex 2x2 matrices and are given by:

$$\sigma_X = \begin{pmatrix} 0 & 1 \\ 1 & 0 \end{pmatrix}, \sigma_Y = \begin{pmatrix} 0 & -i \\ i & 0 \end{pmatrix}, \sigma_Z = \begin{pmatrix} 1 & 0 \\ 0 & -1 \end{pmatrix}, \sigma_{\mathbb{I}} = \begin{pmatrix} 1 & 0 \\ 0 & 1 \end{pmatrix} \tag{2.1.5}$$

The coordinate of a density matrix ρ with respect to a Pauli matrix axis σ is given by Trace$[\sigma\rho]$. The $\sigma_{\mathbb{I}}$ coordinate must be 1. Pauli bases exist for higher-dimensionality structures as well, although their visualisation is considerably more challenging.

In thermal equilibrium with a static Hamiltonian (without loss of generality assumed to be proportional to σ_Z), the density matrix is given by a classical mixture of its eigenstates. Perfectly initialised qubits would occupy a single eigenstate, visualised as a unit vector along $\pm\hat{z}$. Imperfectly initialised qubits would be a classical mixture of these two eigenstates, and would have a diagonal density matrix. Such matrices are described by the states along the $\pm\hat{z}$ axis: they have populations but no coherences (and so the x and y coordinates are zero). The *polarisation* of such a state is given by its norm.

As discussed in Section 2.1.1, any unitary matrix can in principle be performed upon a qubit. Visually, unitaries are arbitrary norm-preserving rotations of the state vector on the Bloch sphere. Rotations of R radians about the axis $\hat{N} = n_X\sigma_X + n_Y\sigma_Y + n_Z\sigma_Z$ have the form:

$$R^N = \exp\left(\frac{-iR\hat{N}}{2}\right) = \cos(R/2)\sigma_{\mathbb{I}} - i\sin(R/2)\hat{N} \tag{2.1.6}$$

Non-unitary operations are able to change the norm of the state vector in the Bloch sphere (that is, the purity of the state). For instance, a system undergoes relaxation to return to its thermal equilibrium state along the $\hat{z}$ axis; this recovery is a non-unitary process. One can distinguish between the relaxation processes that corrupt the coherences of the system (a decay of $\{x, y\}$ coordinates) and those that corrupt the populations of the system (a change in the z coordinate). Often the timescales of these two corrupting processes are quite different; population-recovery rates are denoted $1/T_1$ and coherence-decay (or 'decoherence') rates are denoted $1/T_2$ (T_2 is also referred to as the qubit's 'lifetime').

Given a qubit at thermal equilibrium, unitary operations and relaxation processes restrict the possible set of future states to a smaller concentric sphere with a radius defined by the polarisation of the thermal state. Often the states outside this smaller sphere are explicitly ignored by "renormalising" this smaller Bloch sphere into a sphere of unit radius. This is the visual analogy of the pseudopure approximation introduced in Section 2.1.1.

2.2 QUBIT MANIPULATION

To understand how to control quantum information, one first needs to understand single qubit rotations or *gates*. To have *universal*, or complete, quantum control one must be able to perform all possible unitaries. To generate the entire set of single-qubit rotations one needs only two linearly independent axes around which to rotate. This is useful for physical control schemes that drive transitions using resonant excitation such as magnetic resonance. I take these axes to be x and y, although what follows can be easily generalised to the case of two arbitrary distinct axes. I will show how rotations about the mutually orthogonal direction (in this example, z) can be formed using only rotations in x and y. Such rotations can be generated *dynamically* or *geometrically* [AA87, SCHP87, MTA$^+$06, SMP88].

2.2.1 DYNAMIC ROTATIONS

Dynamic operations are direct rotations. The individual unitaries R^X for R radians of rotation about x are useful examples:

$$R^X = \exp(-iR\sigma_X/2) = \cos(R/2)\sigma_{\mathbb{I}} - i\sin(R/2)\sigma_X = \begin{pmatrix} \cos(R/2) & -i\sin(R/2) \\ -i\sin(R/2) & \cos(R/2) \end{pmatrix}$$

By noting that $\sigma_X\sigma_Y = i\sigma_Z$, a *composite* z rotation can be constructed from the following:

$$\frac{\pi}{2}^X R^Y \left(\frac{-\pi}{2}\right)^X = \frac{1}{2}(\sigma_{\mathbb{I}} - i\sigma_X)(\cos(R/2)\sigma_{\mathbb{I}} - i\sin(R/2)\sigma_Y)(\sigma_{\mathbb{I}} + i\sigma_X) \tag{2.2.1}$$

$$= \cos(R/2)\sigma_{\mathbb{I}} - i\sin(R/2)\sigma_Z \tag{2.2.2}$$

$$= R^Z \tag{2.2.3}$$

Experimentally this composite rotation can be tested upon an ensemble of spins, with results shown in Figure 2.2.

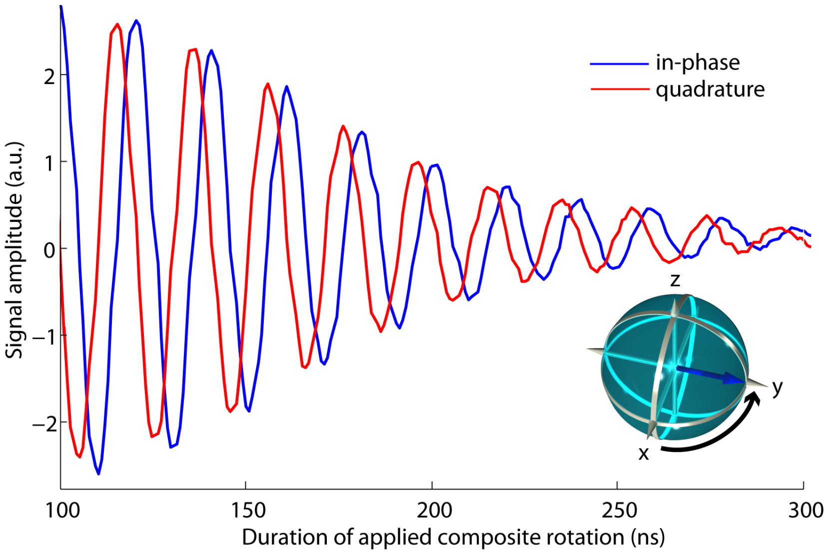

Figure 2.2: **Composite rotations.** Composite R^Z gates dynamically apply phases to states through a sequence of R^X and R^Y pulses. When applied to a σ_X state, this R^Z operation drives the state sinusoidally through the states $\pm\sigma_X$ and $\pm\sigma_Y$. This experimentally collected data displays the in-phase ($\langle\sigma_X\rangle$) component and the quadrature ($\langle\sigma_Y\rangle$) component of an electron qubit coupled to a P donor in ^{28}Si undergoing this composite R^Z rotation.

This simple three-pulse composite rotation is part of a wider class of composite rotations designed to meet a variety of goals. A notable example of this class is the five-pulse composite rotation that minimises the spread of rotation angles known as BB1 [MTA$^+$05a].

2.2.2 Geometric rotations

By examining the definition of R^X one can see that a 2π rotation is not quite the identity (or ‘do-nothing’) operator, rather it is $(-1)\sigma_{\mathbb{I}}$. This oft-dismissed “global phase” can form the basis for very efficient quantum operations. It is an example of a *geometric* gate, where a qubit taken on a closed path on the Bloch sphere acquires a phase[3] [SPM86]. These rotations can indeed be arbitrary; if permitted to rotate about any $\{x, y\}$ (or “in-plane”)

---

[3] This idea is akin to the classical concept of phase acquisition through parallel transport.

axis $\hat{N} = \cos(\phi)X + \sin(\phi)Y$, we could apply the following unitary:

$$\begin{aligned} \pi^{\cos(\phi)X+\sin(\phi)Y}(-\pi)^X &= -i(\cos(\phi)\sigma_X + \sin(\phi)\sigma_Y)(i\sigma_X) && (2.2.4)\\ &= \cos(\phi)\sigma_{\mathbb{I}} - i\sin(\phi)\sigma_Z && (2.2.5)\\ &= (2\phi)^Z && (2.2.6) \end{aligned}$$

Although this two-pulse sequence can be suitably visualised for rigid trajectories with a small number of rotations (See Figure 2.3), a generalisation for continuous trajectories and many-qubit operations requires a somewhat more general description of geometric operations.

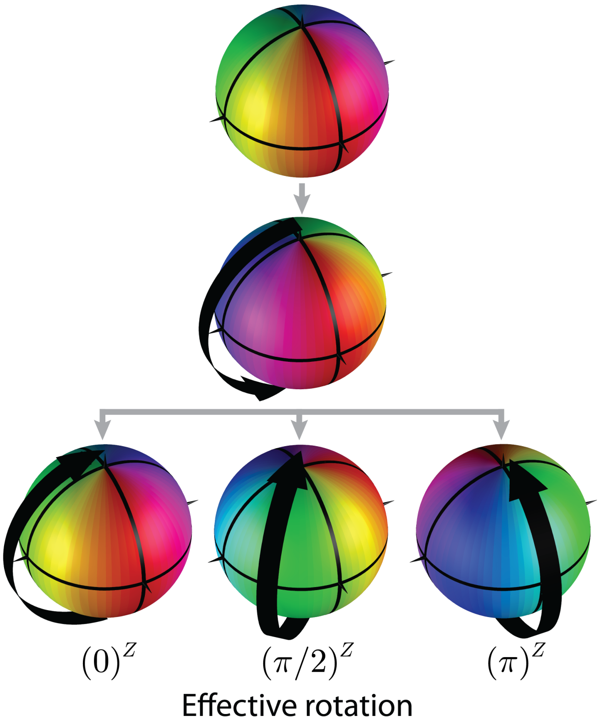

Figure 2.3: **Geometric rotations.** Geometric R^Z gates can be applied to a single qubit using two consecutive π pulses along different axes. The black arrows at each step illustrate the previously applied rotation to the Bloch sphere, and the fixed colour map displays this rotation. Three sample geometric R^Z gate rotations are shown along the bottom.

A given closed path on the surface of a unit sphere encloses a certain fraction of the total 4π surface area; this surface fraction is equal to the *solid angle* mapped out by the trajectory. It can be shown [Ber84] that the phase acquired by a single eigenstate taken on such a trajectory is equal to half the solid angle mapped out by that trajectory. A 2π rotation splits the total solid angle of a sphere 4π into two; half the solid angle it maps out corresponds to a phase of $\exp(i\pi) = -1$. Similarly, if an eigenstate is taken about any closed trajectory that splits the Bloch sphere in half, no matter how complicated the path, that eigenstate acquires the same global phase.

Truly global phases do not alter any expectation values and hence are fundamentally equivalent, however the term 'global' is critically misplaced when the two eigenstates involved are part of a larger Hilbert space. A phase acquired by one-half of a superposition acts very much like a R^Z rotation. To see this, consider a R^Z rotation acting upon the two states $|1\rangle$ and $|3\rangle$ within the slightly larger Hilbert space with an eigenbasis labelled $\{|1\rangle, |2\rangle, |3\rangle, |4\rangle\}$. Notationally this can be written as $R^Z_{1,3}$ and as a unitary operator is expressed as

$$R^Z_{1,3} = \begin{pmatrix} \exp(iR/2) & 0 & 0 & 0 \\ 0 & 1 & 0 & 0 \\ 0 & 0 & \exp(-iR/2) & 0 \\ 0 & 0 & 0 & 1 \end{pmatrix} \tag{2.2.7}$$

One can see that the phase acquired between eigenstates $|2\rangle$ and $|4\rangle$ is zero as expected, however a superposition between eigenstates $|1\rangle$ and $|2\rangle$ would experience a relative phase rotation of $R/2$. This is a simple and effective way to manipulate superpositions indirectly.

We can relate these values to the solid angle mapped out by the trajectory from the sequence presented in Equation 2.2.2 for $R = 2\phi$. A slice of ϕ radians contains the solid angle $4\pi \times (\phi/2\pi) = 2\phi = R$, and so as claimed the phase acquired is equal to half the solid angle of the trajectory of that single eigenstate. The phase acquired between $|1\rangle$ and $|3\rangle$ is precisely twice this value, and this is because both eigenstates $|1\rangle$ and $|3\rangle$ map out equal but opposite trajectories under the sequence given in Equation 2.2.2. A superposition between these two levels consequently experiences the geometric evolution for each of its eigenstates; see Figure 2.4 for an illustration.

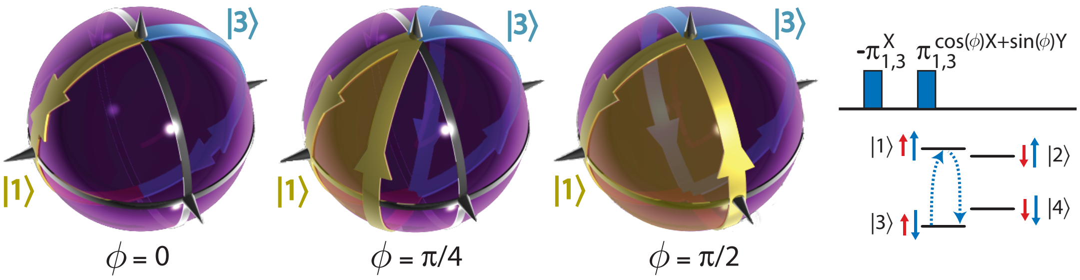

Figure 2.4: **Geometric rotations.** When geometric R^Z-rotations are applied to a subset of a larger Hilbert space (for example, between levels $|1\rangle$ and $|3\rangle$ in the four-level system considered here illustrating Equation 2.2.7), various phases are acquired. One can visually understand these phases by considering the solid angle mapped out by each eigenstate during its closed trajectory, as determined by the in-plane rotation axis, ϕ, of the second π rotation. Here the eigenstate $|1\rangle$ maps out the negative solid angle of eigenstate $|3\rangle$.

2.2.3 SELECTIVE OPERATIONS

If the eigenstates $\{|1\rangle, |2\rangle, |3\rangle, |4\rangle\}$ referred to the four eigenstates of a two-qubit system spanned by $\{|00\rangle, |01\rangle, |10\rangle, |11\rangle\}$, the unitary $R^Z_{1,2} = R^Z_{00,01}$ would be an example of a *selective* or *conditional* operation. Such operations transform one qubit conditional upon the state of the second. For example, $R^Z_{00,01}$ imparts a R^Z rotation on qubit two (the second index) conditional upon qubit one being in the state $|0\rangle$, and is sometimes called a *Controlled-Phase* (or *CPHASE*) operation. A similar element of this family of operations is the *CNOT* gate:

$$\begin{pmatrix} 1 & 0 & 0 & 0 \\ 0 & 0 & 0 & 1 \\ 0 & 0 & 1 & 0 \\ 0 & 1 & 0 & 0 \end{pmatrix} \tag{2.2.8}$$

which ‘flips’ the eigenstates $|01\rangle$ and $|11\rangle$ (that is, performs a π-rotation). Equivalently phrased, this CNOT performs a $\pi^X_{2,4}$ operation, i.e. a π^X operation upon qubit one conditional upon qubit two being in state $|1\rangle$. When presented as a quantum gate, this operation is represented by the symbol $\underset{\bullet}{-\oplus-}$. Quantum algorithms made up of gates like these flow in time from left to right, and unconditional operations are labelled boxes like $-\boxed{X}-$. For further reference on this notation, see Reference [NC00].

Conditional operations can be formed from one another: the sequence $(\frac{\pi}{2})^X$: CPHASE : $(\frac{\pi}{2})^X$ is a CNOT operation. In the same way that a universal set of single-qubit quantum operations can be formed with only two axes of rotation, a universal set of all quantum operations on N qubits can be formed by a much simpler set including only single-qubit operations and pairwise conditional two-qubit operations. A quantum computer that is able to have arbitrarily pure input states and perform this smaller set of quantum operations is said to be a *universal* quantum computer, for it can create any quantum state [NC00].

Occasionally, conditional operations are called *entangling* operations, because they have the power to create entangled states, which are of significant interest to the quantum computing community.

2.3 Density matrix characterisation

Many characteristics of quantum states can be quantified through algebraic manipulations of the density matrix. In this thesis, a state will commonly be characterised according to its linear entropy and negativity, prompting the following explicit definition.

2.3.1 Negativity

Formally [MKB05], the subsystems A and B of a pure state ρ are called *entangled* if there does not exist pure states $|\psi\rangle^A$ and $|\psi\rangle^B$ on subsystems A and B such that

$$\rho = |\psi\rangle^A \otimes |\psi\rangle^B \tag{2.3.1}$$

Analogously, a mixed state ρ is called entangled if there does not exist a convex, unit-sum set of complex numbers $\{p_{i,j}\}_{i,j}$ together with sets of pure states $\{|\psi\rangle_i^A\}_i$ and $\{|\psi\rangle_j^B\}_j$ on subsystems A and B such that

$$\rho = \sum_{i,j} p_{i,j}\ (|\psi\rangle_i^A \otimes |\psi\rangle_j^B)(\langle\psi|_i^A \otimes \langle\psi|_j^B) \tag{2.3.2}$$

One is not restricted to bipartite systems: these definitions are straightforward to generalise to the case of m-partite systems (systems of m particles), in both pure and mixed forms. For notational simplicity, tensor operators are hereafter implied by context.

To test for entanglement, one can test the density matrix for its negativity according to the Positive Partial Transpose operation. Given an arbitrary density matrix over subsystems A and B expressed in the following form:

$$\rho = \sum_{i,j,k,l} p_{i,j,k,l} \ \left|\psi\right\rangle_i^A \left|\psi\right\rangle_k^B \left\langle\psi\right|_j^A \left\langle\psi\right|_l^B \tag{2.3.3}$$

The partial transpose operator reorders system B's coefficients according to:

$$\mathrm{PPT}(\rho) = (\mathbb{I}^A \otimes \mathrm{Transpose}^B)(\rho) = \sum_{i,j,k,l} p_{i,j,l,k} \ \left|\psi\right\rangle_i^A \left|\psi\right\rangle_k^B \left\langle\psi\right|_j^A \left\langle\psi\right|_l^B \tag{2.3.4}$$

If any of the eigenvalues of the matrix $\mathrm{PPT}(\rho)$ are negative, the input density matrix is entangled. The precise value of this negative eigenvalue is the state's *negativity*. A state's negativity takes on a value of $-1/2$ for a pure maximally entangled state up to 0 where the entanglement vanishes.

As an important example, consider the state $\rho = (1-\epsilon)\sigma_{\mathbb{I}}^{\otimes 2} + \epsilon\rho_{PP}$, for $\rho_{PP} = (|00\rangle + |11\rangle)(\langle 00| + \langle 11|)/2$, the Bell pure entangled state. As a density matrix, this takes on the form:

$$\rho = \frac{1}{4}\begin{pmatrix} (1+\epsilon) & 0 & 0 & 2\epsilon \\ 0 & (1-\epsilon) & 0 & 0 \\ 0 & 0 & (1-\epsilon) & 0 \\ 2\epsilon & 0 & 0 & (1+\epsilon) \end{pmatrix} \tag{2.3.5}$$

The PPT of this matrix has a crossing point when:

$$\Rightarrow 0 = \mathrm{PPT}(\rho) = \det\frac{1}{4}\begin{pmatrix} (1+\epsilon) & 0 & 0 & 0 \\ 0 & (1-\epsilon) & 2\epsilon & 0 \\ 0 & 2\epsilon & (1-\epsilon) & 0 \\ 0 & 0 & 0 & (1+\epsilon) \end{pmatrix} \tag{2.3.6}$$

$$= (1+\epsilon)^2[(1-\epsilon)^2 - 4\epsilon] \ \text{ And for } \epsilon \in [0,1], \tag{2.3.7}$$

$$= (1 - 2\epsilon - 3\epsilon^2) \tag{2.3.8}$$

$$= (1+\epsilon)(1/3 - \epsilon) \tag{2.3.9}$$

$$\Rightarrow \epsilon = 1/3 \tag{2.3.10}$$

So in the example of a pseudopure Bell state, one requires $\epsilon \geq 1/3$ to obtain a negative eigenvalue and hence satisfy the PPT condition for entanglement.

2.3.2 Linear entropy

Entanglement requires high-purity states, and the quality of entanglement (as measured by the negativity or concurrence) increases with increasing state purity [WNG+03]. It is possible to put a bound on the concurrence or negativity of a state given its purity, and this relationship can be expressed in terms of the *linear entropy* of the state[4].

The definition of the linear entropy is given by:

$$S_L(\rho) \equiv \frac{\mathcal{N}}{\mathcal{N}-1}[1 - \mathrm{trace}(\rho^2)] \tag{2.3.11}$$

The maximum linear entropy that can sustain a nonseparable state has a value of 0.89 [WNG+03].

The general strategy for maximising the quality of generated entanglement is to first minimise the linear entropy of the state (through either modifying the environment or through the exploitation of non-unitary processes, some of which are covered in Chapter 5) and then creating the desired entangled state. If these states are of sufficient quality, these entangled states can be distilled to create entangled states of arbitrary purity [HHH97].

---

[4] In this work I use linear entropy because its upper limit for entangled states is tighter than the limit for von Neumann entropy $V(\rho) = -\mathrm{Trace}(\rho \ln \rho)$ [WNG+03].

§ 3. Quantum Control with Magnetic Resonance

The spin degrees of freedom within electrons and atomic nuclei are natural qubits. Spins controlled using magnetic resonance have provided the first [JM98], most advanced [NMR$^+$06, VSB$^+$01], and highest fidelity [MTA$^+$05a] experimental demonstrations of quantum algorithms to date. Alternative qubit implementations exist — superconducting qubits, ion-trap qubits and quantum dot qubits to name but a few — but are outside the scope of this thesis.

The particular spin systems employed in this thesis are chosen to suit particular experimental goals (See Figure 3.1). Although each are interesting standalone systems in the context of quantum information, donor defects in silicon are particularly attractive for development into a scalable architecture due to their long lifetimes and potential integration with existing silicon-based technology [Kan98]. At low temperatures, the donor nucleus (such as phosphorus) obtains an associated electron, which is also a valid spin qubit; if the silicon is isotopically pure ^{28}Si, this system is denoted by ^{28}Si:P. To understand how spin qubits work and how to exploit them, we must consider how they respond to their environment, and in particular their magnetic interactions.

Unpaired electrons (with spin $S = \frac{1}{2}$) and spin-active nuclei ($S > 0$) are paramagnetic. They respond to a magnetic field by adjusting their $(2S + 1)$ spin eigenstates' energies. This shift is the spin's Zeeman interaction with the field. In the limit where $|\vec{B}_0|$ is sufficiently large, the Zeeman interaction dominates all other interactions, and (ignoring orbital motion) the Hamiltonian of a single spin takes on the simple form:

$$\mathcal{H} = -\vec{m} \cdot \vec{B}_0 = -g\mu|\vec{B}_0|\sigma_Z/2 \equiv \hbar\omega\sigma_Z/2 \tag{3.0.1}$$

where $\vec{m}$ is the spin's magnetic moment (labeled $\vec{m}_S$ for electrons and $\vec{m}_I$ for nuclei), g is the *gyromagnetic ratio* (also called the *g-factor* for electrons), μ is the Bohr or nuclear magneton (for electrons and nuclei, respectively) and σ_Z is expressed in the $\{+1/2, -1/2\}$

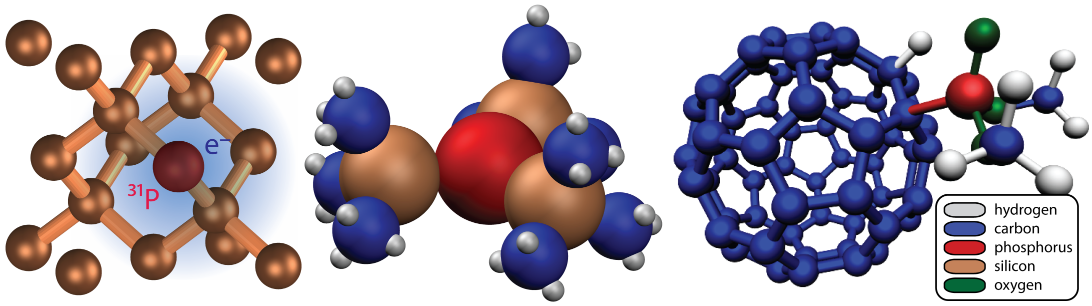

Figure 3.1: **Different physical systems suitable for quantum information processing.** Left: ^{28}Si:P, used to demonstrate ensemble entanglement in Chapter 7, and to explore the relationship of nuclear and electronic relaxation in Chapter 5. Middle: TTMSP, a sample 27+1 spin-active molecule useful for magnetic field sensing in Chapter 4. Right: DMFPH, a C_{60} fullerene with adducts able to support electron-mediated nuclear-nuclear pseudo-entanglement in Chapter 7.

spin basis of the qubit. This expression can be generalised to a larger spin S in the basis $\{S, S-1, ... -S\}$. For free spin-$\frac{1}{2}$ particles, the $\{+1/2, -1/2\}$ spin eigenbasis represents either alignment or anti-alignment with the magnetic field. The Zeeman interaction splits the eigenstates' energy levels, as shown in Figure 3.2, and these eigenstates form a suitable two level system able to support a bit of quantum information. At a fixed magnetic field this energy splitting corresponds to a frequency that can be used to drive transitions between the eigenstates.

Both electrons and nuclei can in principle be good quantum qubits, however at a fixed field and temperature the natural polarisation of an electron is at least ≈ 620 times greater for an electron over that of ^{3}H (the isotope with the highest gyromagnetic ratio) [Lev01]. This places practical restrictions upon the polarisation experimentally available to nuclei without resorting to exotic polarising schemes or milliKelvin temperatures. On the other hand, electrons have much larger wavefunctions than nuclei and couple more strongly to their environment, driving decoherence [SJ08a]. It is fruitful to consider the advantages and disadvantages of each: for instance, nuclei are suitable as a quantum memory resource, and electrons are useful as an initialisation and computational resource [MTB$^+$08]. Coupled electron-nucleus systems can be excellent hybrid qubit systems.

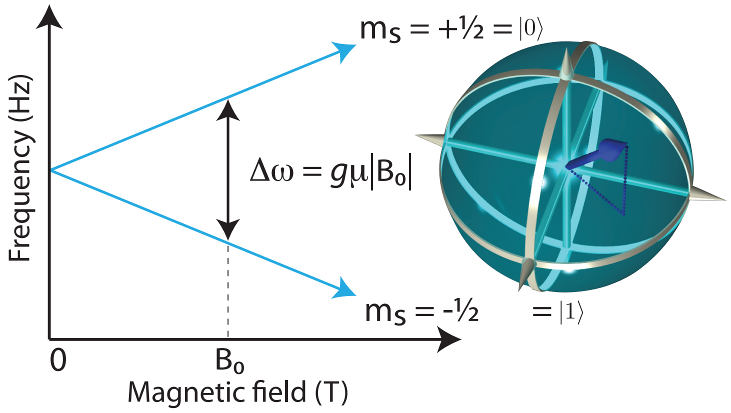

Figure 3.2: **Zeeman effect.** A paramagnetic spin, such as an electron or a spin-active nucleus, is susceptible to a magnetic field B_0, and this splits the energy levels of its aligned and anti-aligned $m_S = \pm\frac{1}{2}$ eigenstates. The energy difference between the two states at a given field corresponds to a frequency that can be used to transition between the two eigenstates. These two eigenstates form the $\pm z$ axis of a qubit's Bloch sphere.

Magnetic resonance is a standard, high-fidelity technique for measuring and manipulating an ensemble of spins. Unfortunately the magnetic moment of a single spin is relatively weak and the spins themselves are often weakly polarised; standard magnetic resonance detectors compensate for this by simultaneously measuring the net magnetisation of least 10^{10} electrons (or 10^{16} nuclei). Measuring the expectation value through a weak coupling rather than building it out of individual eigenstate projections has the advantage that conjugate variables (such as a measurement along σ_X and σ_Y) are not projective measurements and so can be simultaneously probed.

Other detection schemes exist (such as electrically or optically detected magnetic resonance) that work in conjunction with the control techniques developed for magnetic resonance, and in principle any sequences developed for spatial spin ensembles can be applied to single spins (and measured as a temporal ensemble). Although the standard detection scheme lacks sensitivity, magnetic resonance control is advantageous in that it is an inherently parallel quantum control technique, it is portable to any spin-active device or material, and lends itself naturally to the circuit quantum computing model as introduced in Section 2.1. We now turn to the physical implementation of gates using magnetic resonance.

According to the Schrödinger equation, the time-evolution operator of the Hamiltonian Equation 3.0.1 is given by

$$U(t) = \exp(-i\mathcal{H}t/\hbar) = \begin{pmatrix} \exp(i\omega t/2) & 0 \\ 0 & \exp(-i\omega t/2) \end{pmatrix} \tag{3.0.2}$$

Hence the spin precesses about the axis of $\vec{B_0}$ with a frequency ω. To best visualise Bloch sphere rotations acting upon a spin it is useful to choose a rotating frame of reference where the state vector becomes time-independent. We will consider the Hamiltonian in a rotating reference frame given by a frequency ω_p, which may or may not equal ω. If we define

$$U_p(t) = \begin{pmatrix} \exp(i\omega_p t/2) & 0 \\ 0 & \exp(-i\omega_p t/2) \end{pmatrix} \tag{3.0.3}$$

This operator defines a rotating frame of reference where the state $U_p^\dagger(t)\rho U_p(t) \equiv \rho(t)_{\text{rot}}$ is used in place of a density matrix ρ. The arbitrary Hamiltonian $\mathcal{H}(t)$ must also be moved into the rotating frame of reference according to the time-dependent Liouville-von Neumann equation:

$$\begin{aligned}
\hbar\frac{d\rho}{dt} &= -i[\mathcal{H}(t), \rho(t)] && (3.0.4)\\
\hbar U_p^\dagger(t)(\frac{d\rho}{dt})U_p(t) &= -i(U_p^\dagger(t)\mathcal{H}(t)U_p(t)U_p^\dagger(t)\rho(t)U_p(t) - U_p^\dagger(t)\rho(t)U_p(t)U_p^\dagger(t)\mathcal{H}(t)U_p(t)) \\
& && (3.0.5)\\
\hbar\frac{d(U_p^\dagger(t)\rho U_p(t))}{dt} &= -i[U_p^\dagger(t)\mathcal{H}(t)U_p(t), U_p^\dagger(t)\rho U_p(t)] + i[\omega_p\sigma_Z, U_p^\dagger(t)\rho U_p(t)] && (3.0.6)\\
\hbar\frac{d\rho_{\text{rot}}}{dt} &= -i[\mathcal{H}(t)_{\text{rot}}, \rho(t)_{\text{rot}}] && (3.0.7)
\end{aligned}$$

and so the time-dependent Hamiltonian $\mathcal{H}(t)_{0,\text{rot}} = U_p^\dagger(t)(\mathcal{H}_0 - \omega_p\sigma_Z)U_p(t)$ takes the place of $\mathcal{H}(t)$ in rotating frame defined by ω_p. In the $\omega_p = \omega$ frame of reference a state vector is stationary ($\mathcal{H}(t)_{0,\text{rot}} = 0$) and is said to be *on-resonance*. A detuned spin rotates according to an effective σ_Z rotation[1], acquiring phase with a rate of $(\omega_p - \omega)$.

To drive a transition between these two eigenstates, a pulse of frequency ω_p, amplitude B_1 and phase ϕ with respect to the rotating frame (conventionally defined to lie along

---

[1] This effect can be used to implement slow σ_Z rotations with compromised fidelity.

the σ_X axis) modifies Hamiltonian into

$$\mathcal{H}_p = \mathcal{H}_0 + B_1 \cos(\omega_p t - \phi)\sigma_X \tag{3.0.8}$$

Moving into the rotating frame,

$$\mathcal{H}(t)_{p,\mathrm{rot}} = U_p^\dagger(t)(\mathcal{H}_p - \omega_p \sigma_Z)U_p(t) \tag{3.0.9}$$

$$\mathcal{H}(t)_{p,\mathrm{rot}} = \mathcal{H}(t)_{0,rot} - B_1 \cos(\omega_p t - \phi)U_p^\dagger(t)\sigma_X U_p(t) \tag{3.0.10}$$

$$= \begin{pmatrix} (\omega_p - \omega)/2 & B_1 \cos(\omega_p t - \phi)\exp(i\omega_p t) \\ B_1 \cos(\omega_p t - \phi)\exp(-i\omega_p t) & -(\omega_p - \omega)/2 \end{pmatrix} \tag{3.0.11}$$

$$= \begin{pmatrix} (\omega_p - \omega)/2 & B_1 \exp(-i\phi)(1 + \exp(2i\omega_p t)/2 \\ B_1 \exp(i\phi)(1 + \exp(-2i\omega_p t)/2 & -(\omega_p - \omega)/2 \end{pmatrix} \tag{3.0.12}$$

By invoking the *rotating wave approximation*, the high-frequency components are neglected and so $(1 + \exp(2i\omega_p t)) \approx 1$. If applied on-resonance, this modified Hamiltonian takes on the simple time-independent form of :

$$= B_1 \begin{pmatrix} 0 & \exp(-i\phi)/2 \\ \exp(i\phi)/2 & 0 \end{pmatrix} \tag{3.0.13}$$

This amounts to $R^{\cos(\phi)X + \sin(\phi)Y}$, a rotation about the axis $\cos(\phi)\sigma_X + \sin(\phi)\sigma_Y$ with the total angle of rotation R in radians equal to $g\mu B_1 t/h$. These pulses are used to directly drive rotations of states lying in the Bloch sphere.

3.1 Spin Hamiltonian

Coupled spins have modified Hamiltonian terms which characterise how they are coupled. The basic two-spin Hamiltonian exploited in this thesis is of the form:

$$\mathcal{H}_0 = \hbar(\omega_A \sigma_Z \otimes \sigma_I + \omega_B \sigma_I \otimes \sigma_Z + C^{AB}(\vec{\sigma} \cdot \vec{\sigma})) \tag{3.1.1}$$

$$\text{where } \vec{\sigma} \cdot \vec{\sigma} \equiv \sigma_X \otimes \sigma_X + \sigma_Y \otimes \sigma_Y + \sigma_Z \otimes \sigma_Z \tag{3.1.2}$$

In the high-field limit[2] if spins A and B differ, $\vec{\sigma} \cdot \vec{\sigma} \approx \sigma_Z \otimes \sigma_Z$ and the (potentially anisotropic) magnitude of C^{AB} determines its strength, given in Hz. If spin A and B

---

[2] If the spins differ, this approximation is valid by the direct application of first-order perturbation theory: $\langle\psi_i|\sigma_X \otimes \sigma_X|\psi_i\rangle = \langle\psi_i|\sigma_Y \otimes \sigma_Y|\psi_i\rangle = 0$ for eigenstates $\{|\psi_i\rangle\}_i$. When the spins are the same, degenerate perturbation theory is required and this approximation breaks down.

are nuclei, this term is called the J coupling, and arises from interactions mediated by the exchange coupling (via wavefunction overlap) to the electrons orbiting the molecule [ADP51, Lev01]. If spin A is an electron and spin B is a nucleus, this term is either the *hyperfine* interaction, denoted by $\mathcal{A}$, which comes about from the direct exchange coupling of a nucleus to an orbiting electron [Lev01], or the Coulomb interaction of the two dipoles. For completeness, if both spins are electrons, this term can be either be the dipole-dipole coupling $\mathcal{D}$ or the exchange coupling $\mathcal{J}$ [SJ08a]. The effects of these couplings on the transition frequencies for a spin-1/2 electron, spin-1/2 nucleus system can be seen in Figure 3.3.

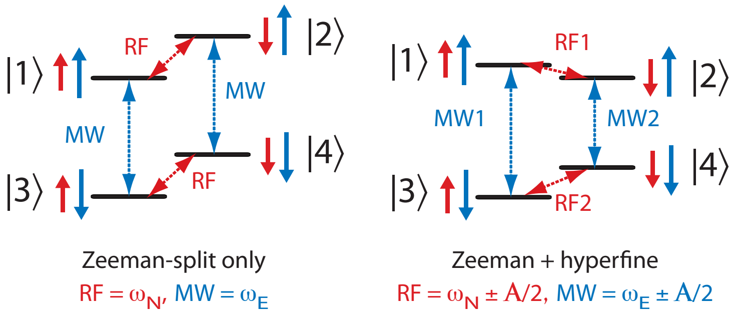

Figure 3.3: **Example energy level diagrams for spin-$\frac{1}{2}$ electron-nucleus systems.** If the electron and the nucleus are uncoupled, the levels are still be Zeeman-split, amounting to the energy level diagram on the left, where the blue (red) corresponds to electronic (nuclear) states and transitions. The electron and nucleus can be unselectively controlled using microwave (MW) and radio-frequency (RF) frequencies (ω_E and ω_N) as shown. Alternatively, a system coupled via a hyperfine interaction $\mathcal{A}$ breaks this symmetry, which permits selective operations according to distinct nuclear and electronic frequencies. In both diagrams the nuclear splitting is greatly exaggerated for clarity.

The initial state of a spin system in thermal equilibrium given by:

$$\rho_{\text{thermal}} = \frac{1}{\mathcal{Z}} \exp(-\beta \mathcal{H}) \tag{3.1.3}$$

for $\beta = (k_B T)^{-1}$ the Boltzmann factor, $\mathcal{H}$ the system's Hamiltonian and $\mathcal{Z}$ the canonical partition function. In the high temperature limit ($\beta \to 0$) this can be approximated as $\frac{1}{\mathcal{Z}}(\sigma_{\mathbb{I}} + \beta \mathcal{H})$. The pseudopure approximation simplifies this further so that $\rho_{\text{thermal}} \approx \beta \mathcal{H}$.

Commercial technology is able to produce homogeneous magnets up to approximately 23 T, where $g\mu|\vec{B_0}| = \hbar\omega$ of ^{1}H yields a transition frequency of 1 GHz. Megahertz frequencies like those used in NMR are often labelled RF for radio-frequency. Electrons operate at much higher microwave (MW) frequencies; in a magnetic field of 3.5 T the operating frequency is on the order of a challenging 100 GHz. For a fixed temperature, the thermal polarisation limitation for nuclei is the magnetic field strength; for electrons it is high frequencies required to perform pulsed magnetic resonance.

3.2 MEASURING SPINS

Both EPR and NMR measure ensembles by detecting small oscillating magnetic fields perpendicular to B_0. NMR uses a *pickup coil*, a solenoid which coaxially encircles the sample; coherent rotating transverse magnetisation creates a weak field which drives a current through the coil connected to the spectrometer [Lev01]. EPR uses a resonator with a magnetic standing wave mode at the desired frequency; coherent rotating transverse magnetisation weakly excites the resonator's mode which is detected in the spectrometer.

When a spin is in thermal equilibrium in a magnetic field, it is aligned (or anti-aligned) along σ_Z, and this weak moment is dwarfed by the large static magnetic fields and so cannot easily be directly detected. The spin must be driven out of equilibrium for detection. A simple pulse about a given axis at the transition frequency separating the two spin eigenstates can rotate the spin into the $\{\pm\sigma_X, \pm\sigma_Y\}$ plane perpendicular to the $\pm\sigma_Z$ axis, which provides the transverse magnetisation required for detection. Hence, the available observables in magnetic resonance are σ_X and σ_Y (often called *in-phase* and *quadrature* signals, respectively[3]). In this picture, the net magnetisation of an ensemble maps naturally onto a vector in the Bloch sphere.

Such a readout pulse rotates the entire ensemble of spins at that transition frequency, both the aligned and anti-aligned spin populations, and so upon rotation the total transverse magnetisation is proportional to the net population difference between the two

---

[3] An on-resonance signal is detected by mixing the weak spin signal with a reference measurement frequency split into two orthogonal components: a signal 'in phase' and a 90° shifted 'quadrature' signal. Hence both x and y net magnetisation in the rotating frame can be measured in a single shot.

eigenstates. The *unobservable* component — the population common to both eigenstates — thus remains undetected using this measurement technique.

3.3 A SINGLE PULSE

An on-resonance $(\frac{\pi}{2})^Y$ pulse rotates a σ_Z state vector perfectly into the state σ_X which rotates coherently in the plane at the transition frequency. In the rotating frame, the coherence remains perfectly still in the state σ_X. Two sorts of decay contribute to an exponential loss of signal over time, which are given the labels T_2 and T_2^*. A coherence has some fundamental lifetime given by T_2. Magnetic field inhomogeneities introduce a separate effect; a range of Zeeman splittings (and hence rotation frequencies) 'fan out' the individual magnetic moments in the plane which over time average out all net in-plane magnetisation. This second coherence limit is given by T_2^*. Consequently a $(\frac{\pi}{2})^Y$ pulse results in an in-phase decaying signal with a decay rate of $\min\{T_2, T_2^*\}$. This signal is called a *free induction decay* (FID).

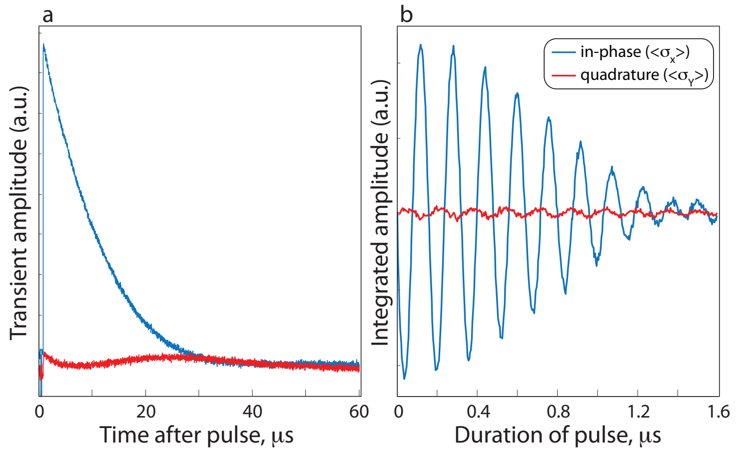

Figure 3.4: **Electron free induction decay (FID) and Rabi oscillations.** With a single R^Y pulse, one can observe the free induction decay of an ensemble of spins, in this example electron spins in ^{28}Si:P. The T_2^* of this FID is 15μs. If one varies the duration of the first pulse and integrates over the first 4μs of the FID, one can observe oscillations about the Bloch sphere, according to $+\sigma_Z \rightarrow +\sigma_X \rightarrow -\sigma_Z \rightarrow -\sigma_X$. This allows us to identify the correct length of a π^Y or $(\frac{\pi}{2})^Y$ pulse, given this microwave power.

A rotation R^Y less than $(\frac{\pi}{2})^Y$ also generates a detectable FID with an initial amplitude proportional to $\sin(R)$. If one were to record the FID amplitude for incrementally longer pulse lengths, one would observe *Rabi oscillations.* This sinusoidal curve also persists but is limited by the microwave pulse inhomogeneities (or 'B_1' inhomogeneities) across the ensemble. A range of rotation strengths 'fan out' or *dephase* the individual magnetic moments in the plane perpendicular to the axis of rotation (See Figure 3.4). This decaying sinusoid can be used to calibrate the precise length and power of $(\frac{\pi}{2})$ and π pulses.

Once a suitable power and length is chosen, it is also possible to scan all the available transitions in an ensemble within certain frequency and field ranges. Using EPR, it is easiest to keep the frequency fixed and vary the magnetic field strength to bring each of these transitions into resonance; for NMR it is easiest to excite a wide range of transitions simultaneously at a fixed magnetic field. The full set of transitions recorded in this way is called the sample's *spectrum.* A field-swept spectrum of a sample can reveal electronic g-factors and their orientation dependence, linewidths and broadening mechanisms, hyperfine couplings and more [FYPM54]. An example spectrum can be seen in Figure 3.5.

A single on-off pulse (or *square pulse*) has a range of frequency components. It is easiest to understand the frequency response of a system by a pulse if one considers its Fourier transform. In frequency space, a square pulse of length t is a sinc function with adjacent zeros at $\pm 1/t$, which is defined as its *bandwidth.* This implies that a spin can be excited by an off-resonant pulse so long as the pulse's frequency profile covers that particular transition frequency. When one views a frequency sweep (or field sweep) of a system, one measures the convolution of the underlying spectrum of the sample with the Fourier transform of the pulse within an experimentally determined detection window. Longer pulses are more selective than short pulses, and very selective pulses can be used for conditional quantum operations. If spin A is coupled to another spin B with a coupling of C^{AB} Hz, the qubit transitions for spin A will be separated by C^{AB} Hz in frequency space depending upon the state of spin B. A pulse with a bandwidth of $1/C^{AB}$ that is resonant with one of these transitions is able to manipulate spin A conditional upon the state of B. In general, if one wishes to rotate a spin with frequency f_1 and not rotate a spin with frequency f_2, one can place the first zero of the sinc function at f_2 with a

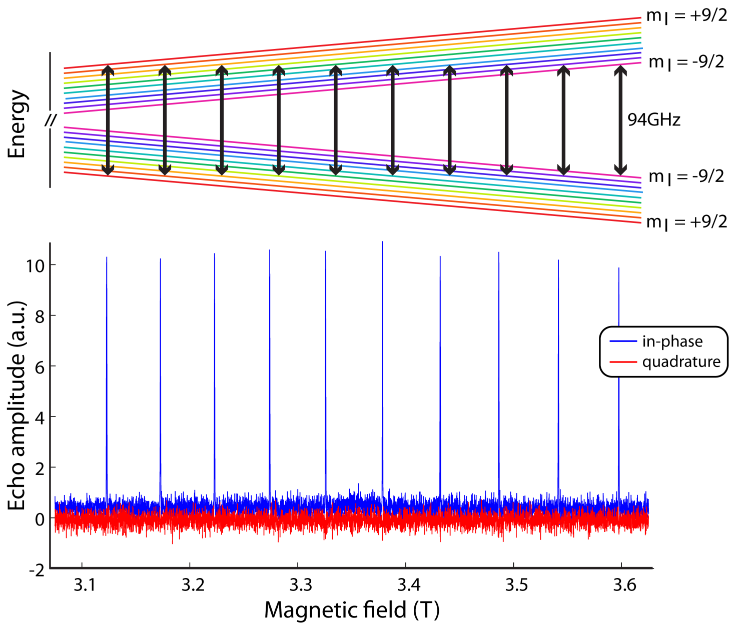

Figure 3.5: **Field sweep spectrum.** By applying a fixed microwave frequency (in this instance, ≈ 94 GHz) and sweeping the magnetic field, one can locate the available transitions in the spin system. In the case of an electron spin ($m_S = 1/2$) associated with a bismuth nuclear spin ($m_I = 9/2$) in ^{28}Si, one can see a distinct electronic transition ($\Delta m_S = 1$) for each of the ten nuclear spin configurations, and these are spaced by the two spins' hyperfine coupling of 52.6 mT (equivalently 1.475 GHz).

square pulse of frequency f_1 and length of $1/|f_1 - f_2|$.

A $\pi/2$ rotation of length t and amplitude A can also be performed with a pulse of length $t/2$ and amplitude $2A$. Consequently, if high enough power pulses are available, a single $\pi/2$ pulse can have a bandwidth much larger than the full spectrum of the sample. This allows for Fourier transform spectroscopy, the default excitation scheme used in NMR, where a single pulse applies simultaneously to all spins of the same isotope. Although these manipulations are fast and allow for many quantum operations within the spin lifetime, conditional operations must be done indirectly [Jon11].

3.4 Spin-echoes

The dephasing effects attributed to T_2^* decay can often be distinguished from T_2 effects with a two-pulse sequence called a *spin-echo*. Immediately after a coherence-generating

$(\frac{\pi}{2})^X$ pulse, all spins begin in the plane with a shared phase. Each spin then precesses slowly in the plane at some positive or negative rate commensurate with its detuning δ relative to the reference frame. If after a time τ, each spin now having accumulated its own phase $\delta\tau$, a π^X pulse is applied, the phase of that spin's coherence becomes $\pi - \delta\tau$. The coherence continues to acquire phase at a rate of δ, and so after a second pause of τ, each spin shares the in-plane phase of π, which would form a detectable signal called an *echo*. This *refocusing* technique effectively decouples the ensemble from its inhomogeneous environment, and is essential for maintaining long-term coherent control of an ensemble of spins. A visual representation of this refocusing technique is shown in Figure 3.6. The advantage of measuring population differences with echoes is that for τ sufficiently large there are no pulses (and their associated detector protection delays) interfering with the spin signal and a clear amplitude can be measured.

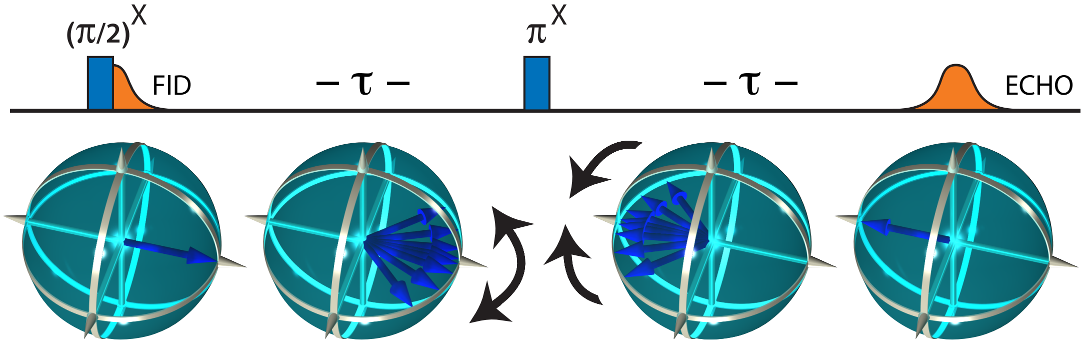

Figure 3.6: **Refocusing inhomogeneities.** Each spin in an ensemble experiences a slightly different magnetic field, and so at a time τ after a coherence-generating pulse each spin has acquired a given phase offset with respect to the chosen rotating frame. A π pulse has the effect of reversing this temporary dephasing by effectively switching positive acquired phases into negative ones. The spins with the largest positive offsets continue to evolve the most quickly with respect to the rotating frame, recombining with the spins with the smaller offsets to form a coherent echo.

An inhomogeneous background magnetic field results in a range of Zeeman splittings across the sample, and if these inhomogeneities are static on the timescale of the spins' lifetime they can be refocused with appropriate π pulses. The sample's field-swept spectrum has *inhomogeneously broadened* transitions reflecting this. The width of these transitions at half-maximum is called a transition's *linewidth*. In contrast, dynamic environmental changes such as field and frequency fluctuations cannot be refocused because the magnetic environment and hence the detuning δ is not the same before and after the refocusing pulse. The changing magnetic environment means that the frequency of an individual spin may drift within the measured linewidth; this is called *spectral diffusion*. Static inhomogeneous broadening can be distinguished from dynamic inhomogeneous broadening through *hole-burning* sequences. A pulse more selective than the linewidth of a static inhomogeneously broadened transition can 'burn' amplitude away from that subset of spins, demonstrating coherent control of that stable subset.

In addition to the range in Zeeman splittings (through an inhomogeneous B_0), the inhomogeneity of B_1 across the ensemble can lead to unintentional FIDs and echoes which reduce the overall fidelity of a sequence. For example, a calibrated refocusing pulse can still be imperfect and generate an FID, and two perfect $(\frac{\pi}{2})^X$ pulses can generate an echo. To understand the latter semi-classically, a $(\frac{\pi}{2})^X$ pulse can be seen to flip precisely half of the ensemble, and so the half of the coherences formed by the first $(\frac{\pi}{2})^X$ pulse are refocused into an echo. In a similar vein, three-pulse sequences can form *stimulated echoes* [Hah50]. Two pulses separated by τ encode some proportion of generated coherences which have been fanning out for a time τ into populations of the two eigenstates. At some time later (less than T_1), a third pulse transforms these populations into coherences of opposing phase which continue to evolve at different rates, generating a small echo after the same time τ after the third pulse. Echos can easily overlap one another, and if pulse timings are not carefully chosen stimulated echoes can corrupt the final outcome of a quantum algorithm.

3.5 Measuring relaxation

3.5.1 T_2 measurements

The amplitude recovery of the spin-echo sequence ($(\frac{\pi}{2})^X : \tau : \pi^X : \tau :$ echo) is ultimately limited by the decoherence of the spin T_2. In this way τ can be extended to measure the rate of decoherence of the system. The decay of signal is a lower bound for the true T_2 of an individual spin; field fluctuations (among many other processes) during the sequence can lead to shorter ensemble decay times. Because a spin is a magnetic moment, the application of a π pulse itself changes the nearby spins and hence the local magnetic field. The effect, called *instantaneous diffusion*, can be averted by refocusing fewer and fewer spins (applying weaker and weaker refocusing pulses), which in the limit of an infinitely weak refocusing pulse simulates a single-spin environment. Example data displaying this trend is shown in Figure 3.7. Using these techniques, among others, electrons in ^{28}Si:P have been shown to display T_2 times exceeding seconds [TTM+11].

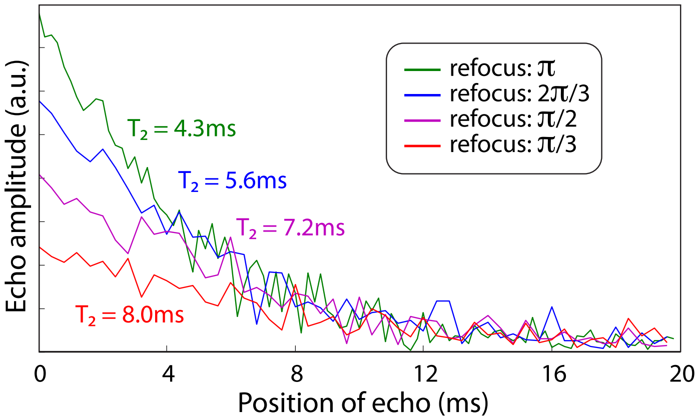

Figure 3.7: **T2E curves for different refocusing angles.** At 9.6 GHz and at 7 K, electrons in a ^{28}Si:P sample can be used to illustrate the principle of instantaneous diffusion. By extending the delay τ in a spin-echo experiment, one can measure a T_2 value. If one chooses a refocusing pulse which flips fewer spins, each spin's local environment is less likely to differ due to the refocusing pulse, and so relaxation times which simulate a lower donor density can be extracted. (The applied refocusing pulses' rotation angles are approximate.)

Maintaining stable magnetic environments on the order of seconds is challenging. Often the simple two-pulse spin-echo sequence is less effective than similar sequences which refocus more frequently on shorter time intervals. Members of this class of sequences are CP, CPMG and XYXY sequences [MTA+05b], which use repeated combinations of $\{\pi^{\pm X}, \pi^{\pm Y}\}$ pulses to refocus spins over time intervals shorter than the correlation time of the field fluctuations. Of course the natural concern for such repetitive sequences are the stimulated echoes they generate; 'long tail' effects occur giving rise to falsely optimistic

T_2 times. Evidence for this can be seen from the difference in T_2 times for σ_X and σ_Y input coherences; a general magnetic environment decoupling sequence revealing the bare T_2 time would not prefer a particular coherence as input. The XYXY sequence does not suffer from this error as it is symmetric about σ_X and σ_Y. Although XYXY is sensitive to rotation errors, once calibrated properly it can be used to extract long T_2 times by decoupling the spin from its slowly time-varying environment.

3.5.2 T_1 MEASUREMENTS

Each experimental run, or *shot*, assumes a thermal equilibrium initial state, and so it is important to measure the spin-lattice relaxation time T_1 to determine how long one must wait before the system can again be assumed to be in thermal equilibrium. If one does not wait sufficiently long enough, the polarisation will be somewhat reduced and the transition is said to be *saturated*. One way to measure this polarisation recovery time is to monitor the amplitude of a spin-echo experiment with a fixed τ as one varies the *shot repetition time* (SRT) of the experiment. The echo amplitude grows with the shot repetition time with the profile of an inverted decaying exponential, and this recovery rate is T_1. For shot repetition times exceeding many T_2^* this strategy is accurate because after each shot the state is left with the same evenly distributed populations due to the spin-echo experiment. Instead of a single spin-echo to divide populations, one can alternatively *saturate* the transition by repeatedly driving spin-echo experiments with a shot repetition time much shorter than T_1, leaving the state in an entirely mixed form.

A three-pulse sequence can also be used to determine T_1 without varying the shot repetition time if one adopts a shot repetition time much longer than T_1. At the outset of each experiment the populations of an initial thermal state are inverted with a π pulse, and after a time τ the population difference is measured with a spin-echo sequence. The time τ can be varied to recover the inverted decaying exponential and hence T_1 time for that transition.

Although population differences are measured via spin-echo sequences, ultimately the observables in magnetic resonance are σ_X and σ_Y, and these measurements are not projective. Due to this fact, coherent manipulations of the state after measurement are possible (and useful!). An echo can be again refocused so that it can be later coherently rotated back into a state approximately equal to the thermal equilibrium state. Given a system with sufficiently long T_2 times and high-fidelity pulses, the technique of returning the state to its thermal equilibrium state after measurement, sometimes known as a ‘tidy’ sequence, has two principle advantages. The first is the reduction of the required shot repetition time far below T_1, which is useful when manipulating spin transitions with long T_1 times. The second is to minimise effects which depend upon a nonequilibrium spin state; we will see in Chapter 5 how the act of leaving spins in an even mixture after a spin-echo sequence can influence the unsaturated equilibrium state.

3.6 Nuclear control and decoherence

In addition to the direct T_1 and T_2 pulse sequences above, T_1 and T_2 values can also be measured indirectly with the aid of a coupled spin. Such techniques are prevalent in EPR, where both nuclei and electrons can be coherently controlled but can often only the electron can be measured.

One can detect the frequency of nuclear transitions via the electron using pulsed electron-nuclear double resonance (ENDOR) techniques [Feh56]. In the high-temperature approximation, an electron is polarised $\approx 10^3$ times more than any nucleus it is coupled to, and so the population difference across a nuclear transition is generally insufficient for detection using the electron. To overcome this, populations can be selectively inverted to give nuclear transitions the polarisation of an electron. After this, an RF pulse can be used to modulate the amplitude of a following spin-echo detection provided the pulse frequency matches the transition frequency.

This basic Davies ENDOR sequence applied to a hyperfine-coupled spin-$\frac{1}{2}$ electron, spin-$\frac{1}{2}$ nucleus system can be presented in multiple ways; a pulse sequence combined with an energy-level representation of the following matrix representation is seen in Figure 3.8. For this system we adopt a basis consistent with the remainder of this thesis, $|m_I, m_S\rangle = \{\left|+\frac{1}{2},+\frac{1}{2}\right\rangle, \left|-\frac{1}{2},+\frac{1}{2}\right\rangle, \left|+\frac{1}{2},-\frac{1}{2}\right\rangle, \left|-\frac{1}{2},-\frac{1}{2}\right\rangle\} := \{|1\rangle, |2\rangle, |3\rangle, |4\rangle\}$. Adopting the pseudopure approximation and assuming on-resonant control of transition $\{1, 3\}$, Davies ENDOR operates as:

$$\rho_{\text{thermal}} \approx \begin{pmatrix} 0 & 0 & 0 & 0 \\ 0 & 0 & 0 & 0 \\ 0 & 0 & \frac{1}{2} & 0 \\ 0 & 0 & 0 & \frac{1}{2} \end{pmatrix} \tag{3.6.1}$$

$$\pi^X_{1,3}\ \rho_{\text{thermal}}\ {\pi^X_{1,3}}^\dagger \approx \begin{pmatrix} \frac{1}{2} & 0 & 0 & 0 \\ 0 & 0 & 0 & 0 \\ 0 & 0 & 0 & 0 \\ 0 & 0 & 0 & \frac{1}{2} \end{pmatrix} \tag{3.6.2}$$

$$\pi^X_{3,4}\ \pi^X_{1,3}\ \rho_{\text{thermal}}\ {\pi^X_{1,3}}^\dagger\ {\pi^X_{3,4}}^\dagger \approx \begin{pmatrix} \frac{1}{2} & 0 & 0 & 0 \\ 0 & 0 & 0 & 0 \\ 0 & 0 & \frac{1}{2} & 0 \\ 0 & 0 & 0 & 0 \end{pmatrix} \tag{3.6.3}$$

Hence, when the nuclear $\pi^X_{3,4}$ pulse is sufficiently off-resonance that it applies a negligible rotation, the state remains as Equation 3.6.2 and reveals a spin-echo population difference along the transition $\{1,3\}$ that is negative but equal to a full thermal amplitude. When the $\pi^X_{3,4}$ is on-resonance it moves surplus populations entirely into a single nuclear configuration ($m_I = +\frac{1}{2}$) and the spin-echo population difference along the transition $\{1,3\}$ is measured as zero. Note that, if the nuclear pulse had instead been along the $\{1,2\}$ transition, the surplus populations would have been instead moved into the ($m_I = -\frac{1}{2}$) configuration, yet the population difference along the transition $\{1,3\}$ would still be measured as zero.

The ENDOR pulse sequence modifies nuclear populations and so to assume a starting state of thermal equilibrium one must wait longer than the nuclear spin-lattice relaxation time T_{1N}. T_{1N} can be orders of magnitude longer than T_{1E} and extends the required shot repetition time of the experiment accordingly. In order to avoid such unnecessary delays, nuclear tidy π pulses are used after measurement to redistribute surplus populations evenly across nuclear configurations [TMAL06]; regular T_{1E} processes can then equilibrate the state relatively quickly. Of course, both nuclear and electronic tidy pulses can be

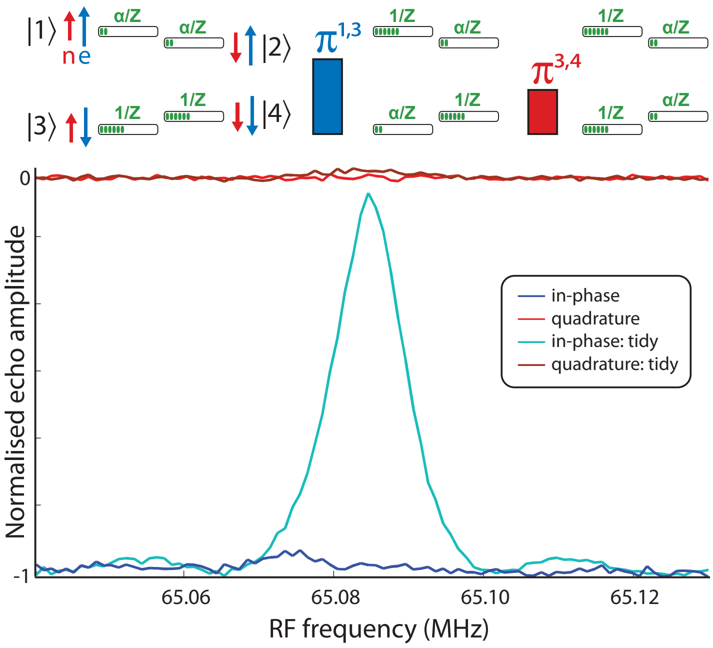

Figure 3.8: **An ENDOR sequence and spectrum with and without a tidy pulse.** The top panel illustrates the ENDOR sequence, where $\mathcal{Z}$ is the partition function, α is determined by the field and temperature, and the green counters represent populations. From an initial thermal state one can swap the electron's polarisation with the nucleus with two π pulses. With an off-resonant RF frequency, an ENDOR sequence results in a negative echo when compared to an optimised spin-echo sequence, as observed in the bottom panel. With a tidy pulse, the state returns to thermal equilibrium after each shot and so sweeping the RF frequency reveals the nuclear transition (convolved with the frequency profile of the square pulse, which in frequency space is a sinc function). If there is no tidy pulse, the ENDOR sequence reveals very little about the nuclear structure because the nuclear state is largely mixed; it can not be considered to be in thermal equilibrium at the start of each shot.

employed to return the state to thermal equilibrium after each measurement, allowing for a shot repetition time much faster than both T_{1E} and T_{1N}. A second benefit of this technique is that it is able to probe spin-dependent dynamics less perturbatively in circumstances where the act of leaving the spins mixed after a spin-echo measurement influences the system's dynamics. This principle is used in Chapter 5 to measure the nuclear polarisation enhancement more faithfully.

One could measure T_{1N} by monitoring the recovered signal as one varies the shot repetition time of the ENDOR experiment. Similarly, one could saturate the nuclear transition via ENDOR and then wait for a variable length of time before performing an ENDOR experiment to measure the recovered signal. After measurement, saturation-recovery can begin anew. These measurements are faithful but slow when T_{1N} times exceed minutes, as is the case for donors in silicon at low temperatures [FG59].

It is worth noting that the *cross relaxation* time T_{1X} between levels 1 and 4 can be shorter than the direct nuclear relaxation time T_{1N}, and if T_{1E} is shorter than both, the nucleus equilibrates with a time constant of T_{1X}. Consequently, measuring T_{1N} with these approaches amounts to measuring the shorter of $\{T_{1X}, T_{1N}\}$ when coupled to a fast-relaxing electron spin [FG59].

A more sophisticated, faster T_{1N} measurement sequence involves re-using the existing polarisation rather than re-initialising the system after every measurement. The key is to interpret the ENDOR sequence as a polarisation-SWAP operation between the electron and the nucleus. The first ENDOR sequence polarises the nucleus. After a waiting period, measurements are made by SWAPing the decayed polarisation into the electron and measuring population differences using a spin-echo followed by tidy pulses. After measurement, the existing polarisation can be coherently SWAPed back to the nucleus to continue its decay. Rotation errors on this SWAP-measure-SWAP operation produce a lower bound for the true T_{1N}, but if one can determine the fidelity of this operation (say by repeating it many times on a timescale $<< T_{1N}$ to observe fidelity-driven decay) its effects can be removed during data analysis. Saturation-recovery and shot repetition time sequences measure T_{1N} on the order of $(T_{1N})^2$, whereas this new SWAP-recovery sequence measures T_{1N} on the order of T_{1N}.

The nuclear coherence lifetime T_{2N} differs from T_{1N} because it is limited by the electron: T_{2N} is limited to $2T_{1E}$ [MTB$^+$08]. On this timescale, however, stimulated echoes are present and care must be taken to record only the designated nuclear coherence. Interestingly, even though there is often no fixed phase relationship between the microwave and radio-frequency pulses at the outset of a single shot, a coherence generated in the nucleus and then moved into an electronic coherence for readout would have the phase of that microwave signal. This allows for a number of various T_{2N} pulse sequence measurements, including ones where the coherence is generated in the nucleus or alternatively the coherence is both generated and measured using the electron spin [MTB+08]. A sample T_{2N} measurement is shown in Figure 3.9.

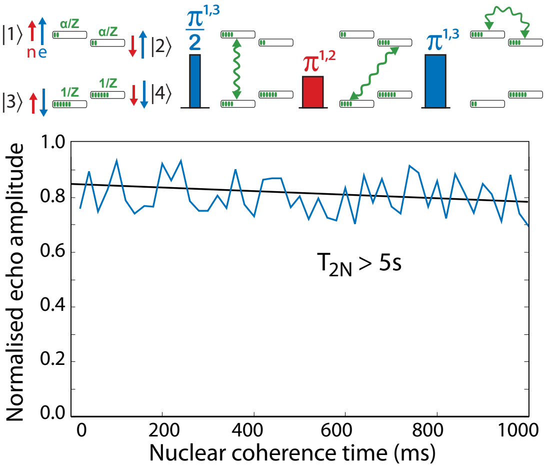

Figure 3.9: **Nuclear T_2 sequence.** A nuclear coherence can be made and measured through a coupled electron spin. The topmost sequence illustrates the first half of this sequence. From an initial thermal state one can form an electronic coherence and then map it into a nuclear coherence with two π pulses. After this, a refocusing pulse (or another decoupling sequence) can be applied, and then by applying the sequence in reverse the coherence can be mapped back onto the electron for readout. By extending the time the nuclear coherence is held, one can measure T_{2N}, with a sample dataset using ^{28}Si:P up to 1 second taken at 4.5 K and 0.35 T, normalised to a spin-echo of the same τ value. This pulse sequence was tested for stimulated echoes by removing the nuclear pulses and observing no echo. Assuming a monoexponential decay, a fit to this data reports a T_{2N} value greater than 5 seconds with 95% confidence.

To create and encode an electronic coherence into a nucleus, one can perform the following sequence [HGM86, MTB+08]. Beginning with a $(\frac{\pi}{2})^X_{1,3}$ pulse, the coherence can be swapped into the chosen nuclear transition (here assumed to be $\{1 : 2\}$) with a $\pi^X_{1,2}$ pulse followed by a $\pi^X_{1,3}$ pulse. As with any ensemble of qubits, after a time τ this nuclear coherence will have dephased due to inhomogeneities; a refocusing $\pi^X_{1,2}$ pulse returns the spins into a coherent state after another time τ so that the spins can be

SWAPed back into an electronic coherence for spin-echo or FID detection. The input coherence phase correlates with the measured echo phase, and any spurious echoes can be removed by taking the difference of two T_{2N} measurements with respect to different input phases [MTB$^+$08]. Modifications exist for this basic T_{2N} sequence. Instead of encoding an FID into a nuclear coherence one can perform a spin-echo experiment at the outset to encode an echo into a nuclear coherence free of electronic dephasing; one can also opt for XYXY-type nuclear decoupling strategies in place of a single refocusing pulse.

3.7 MANIPULATING COHERENCES

Refocusing or decoupling strategies for general states are straightforward extensions of the single-coherence methods introduced already. If a two-qubit spin state contains a two-qubit coherence (either a *double quantum coherence* $|DQC\rangle = |00\rangle^{AB} \langle 11|^{AB}$ or a *zero quantum coherence* $|ZQC\rangle = |10\rangle^{AB} \langle 01|^{AB}$, so called because of the angular momentum difference between the two superposition components), both qubits need to be refocused. The simplest refocusing strategy for these states is to apply single π pulses to both qubits simultaneously, midway through the total delay τ. One can alternatively apply two refocusing pulses to qubit A placed at times $\tau/4$ and $3\tau/4$, and one to qubit B at time $\tau/2$.

To discuss the effects of various decoupling strategies we can label stages of a sequence according to the relative phase of a spin perfectly on-resonance with a spin of positive detuning Δ. A π pulse would reverse the sign of the relative phase, switching a ‘positive’ label to a ‘negative’ label[4]. These labels can be used for each qubit throughout a given sequence to quickly determine which effects are decoupled. For example, under both schemes described above, both qubit A and qubit B are dephasing ‘positively’ for half the total delay, and dephasing ‘negatively’ for the other half; both qubits are therefore decoupled from the environment and refocus into an echo. The latter refocusing approach has the distinguishing feature that qubits A and B are additionally decoupled from each other as well; for precisely half the time the evolution of the two spins differ in parity, as

---

[4] The terms ‘positive’ and ‘negative’ are arbitrary; any fixed convention applies.

Pulse sequence:

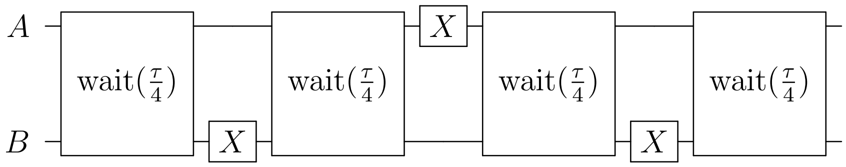

Equivalent parity chart:

Coherence \ Time	$\tau/4$	$\tau/4$	$\tau/4$	$\tau/4$
Qubit A	+1	+1	-1	-1
Qubit B	+1	-1	-1	+1
Product AB	+1	-1	+1	-1

Table 3.1: **A general refocusing strategy.** To maintain a state subject to various static inhomogeneous couplings for a time τ, one can reverse environmental effects with a refocusing sequence of well-chosen π pulses. One can arbitrarily assign a direction of coupling to each qubit to track its evolution through the refocusing sequence, where a π pulse reverses its direction. These directions can be presented in the form of a parity chart to simplify analysis. To decouple a set of qubits from a static environment, the time-weighted sum of the rows must equal zero. To decouple two qubits from one another, the time-weighted sum of the product of the two rows must also equal zero; they must spend half the time evolving 'against' one another.

seen by the parity chart in Figure 3.7. A general decoupling strategy seeks to decouple spins from internal interactions such as these, and measuring the fundamental effective T_2 of such coherences requires full decoupling strategies. This basic principle guides the construction of refocusing strategies for more complicated mixed states consisting of multiple coherences [LCYY00].

Managing multiple coherences for many-qubit systems involves tracking how each qubit positively and negatively dephases under a particular sequence, both with respect to the background environment and with respect to each other. By induction one can verify that a naïve refocusing strategy of N coupled qubits requires $\sum_{j=0}^{N-1} 2^j = 2^N$ pulses, where adding a qubit simply adds refocusing pulses midway through all the previously applied pulses. This exponential requirement can luckily be reduced to only $2N^2$ gates if the parity charts are chosen wisely: it is a problem isomorphic to finding orthogonal matrices whose elements are ±1 [LCYY00]. Immediately, one can see that systems which do not need many-qubit refocusing strategies have a quadratic advantage over fully-coupled systems with always-on couplings. It is therefore of interest to investigate systems with on-demand couplings as candidate quantum architectures, or at least identify conditional operations that do not rely upon coupling-limited delays during which coherences need to be refocused.

3.7.1 Selective operations

Electron-nuclear couplings can be tens of MHz (even greater than GHz, as is the case of bismuth donors in silicon). In such an environment a square pulse is able to selectively address an individual transition with pulses on the order of 100 ns or less. In contrast, nuclear-nuclear J-couplings are typically smaller than a few hundred Hz [Lev01], and the corresponding selective pulses require millisecond pulses or longer which may not be experimentally possible. Alternatively, the couplings between different spins can be used for conditional operations even when the couplings are much narrower than the bandwidth of available pulses [JM98]. As an example, we demonstrate how to perform conditional operations upon two coupled spins using only delays and unconditional operations.

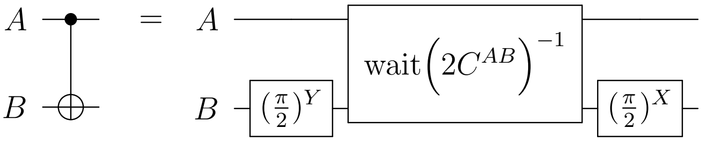

(3.7.1)

Figure 3.10: **Conditional gates through unconditional operations.** A CNOT gate can be implemented with unconditional operations by allowing the coupling of the system to evolve the state. The sign of the acquired phase of B depends upon the state of A, and after a time $\left(2C^{AB}\right)^{-1}$ the two cases differ in phase by π. At this point the coherence can be rotated back into a population which is conditional upon the state of A.

To first order, each of the dominant spin-spin couplings introduced in Section 3.1 between spin A and spin B are of the form $C^{AB}\sigma_Z^A\sigma_Z^B$. Such a coupling imposes a cyclic evolution according to $\sigma_Z^A\sigma_X^B \Rightarrow i\,\sigma_{\mathbb{I}}^A\sigma_Y^B \Rightarrow -\sigma_Z^A\sigma_X^B \Rightarrow -i\,\sigma_{\mathbb{I}}^A\sigma_Y^B$. Using this mechanism, a CNOT operation between A and B can be applied with the sequence $(\frac{\pi}{2})^Y_B$: wait$(1/2C^{AB})$: $(\frac{\pi}{2})^X_B$. This can be visualised by considering the evolution of σ^B_X coupled to either σ^A_Z (an alternative label for $|0\rangle$) or $-\sigma^A_Z$ ($|1\rangle$) individually. If coupled to σ^A_Z, σ^B_X evolves 'positively' with respect to its rotating reference frame, and if coupled to $-\sigma^A_Z$, σ^B_X evolves 'negatively'. After a time $1/2C^{AB}$ these two cases have a phase of π radians relative to each other; a final pulse of σ^B_X returns the coherence into a population conditional upon the state of σ^A. This was the method used to apply CNOT gates in the first magnetic resonance quantum algorithms [JM98] and for the whole of Chapter 4, and this sequence also forms the basis for the SEDOR sequence used in Chapter 7.

These CNOT gates can be used as entangling operations like any other conditional gate. With a leading unselective $(\frac{\pi}{2})^Y_A$ operation applied to the input $|0\rangle^A|0\rangle^B$ state, this process looks like:

$$|0\rangle_A|0\rangle_B \tag{3.7.2}$$

$$(\frac{\pi}{2})^Y_A \Rightarrow \frac{1}{\sqrt{2}}(|0\rangle_A + |1\rangle_A)|0\rangle_B \tag{3.7.3}$$

$$(\frac{\pi}{2})^Y_B \Rightarrow \frac{1}{2}(|0\rangle_A + |1\rangle_A)(|0\rangle_B + |1\rangle_B) \tag{3.7.4}$$

$$\text{wait}(1/2C^{AB}) \Rightarrow \frac{1}{2}[|0\rangle_A(|0\rangle_B + i|1\rangle_B) + |1\rangle_A(|0\rangle_B - i|1\rangle_B)] \tag{3.7.5}$$

$$(\frac{\pi}{2})^X_B \Rightarrow \frac{1}{\sqrt{2}}(|0\rangle_A|0\rangle_B + |1\rangle_A|1\rangle_B) \tag{3.7.6}$$

Therefore the couplings in the system itself allow for two-qubit selective operations, however they are time-limited by the coupling strength of the spins in the same way that selective pulses are bandwidth-limited.

When these delays are much longer than T_2^*, one must compensate for dephasing by refocusing during the delay. In this event one would like the spins to decouple from the environment but not from to each other; π pulses on both spins midway through the delay allows the coupling to continue to acquire a conditional phase, whereas a full refocusing scheme of wait$(1/8C^{AB})$: π^X_B : wait$(1/8C^{AB})$: π^X_A : wait$(1/8C^{AB})$: σ^X_B : wait$(1/8C^{AB})$ refocuses the effects of the spin-spin coupling and no conditional gate is applied.

§ 4. Quantum Metrology

In a locally homogeneous magnetic field, an isolated spin precesses with a frequency given by its Zeeman energy splitting. This frequency depends only on the spin species and the local magnetic field. Magnetic resonance techniques are able to measure the frequency of precession of an ensemble of known identical spins quite precisely, from which it is possible to deduce the local magnetic field.

More generally, the time-evolution operator of an isolated particle with a σ_Z Hamiltonian is given by:

$$U(t) = \exp(-i\zeta\sigma_z t/2) = \begin{pmatrix} \exp(-i\zeta t/2) & 0 \\ 0 & \exp(i\zeta t/2) \end{pmatrix} \tag{4.0.1}$$

where ζ is a constant specific to the Hamiltonian and hence experimental environment. In this situation, a qubit in the state $\frac{1}{\sqrt{2}}(|0\rangle + |1\rangle)$ evolves according to $\frac{1}{\sqrt{2}}(|0\rangle + \exp(i\zeta t)\,|1\rangle)$ (ignoring global phases). Observing this evolution over time, we are able extract the value ζ. In particular settings, ζ contains interesting information about the environment (such as distance travelled, magnetic field magnitude, gravitational strength, and more) that are not precisely known experimentally. Measuring ζ amounts to estimating these values. From the central limit theorem, the maximum precision of such a measurement taken over many averages (the standard deviation of measured values of ζ) scales according to 'Standard Quantum Limit scaling' [LSS92], which varies as $\Delta/\sqrt{N\nu}(|\lambda_1 - \lambda_0|)$ for N the number of copies of probe particles, Δ^2 the variance of the measurement for each probe per unit time, $(|\lambda_1 - \lambda_0|)$ the Hamiltonian's eigenvalues and ν the number of measurement repetitions [GLM06].

Now consider the entangled state $\frac{1}{\sqrt{2}}(|000...000\rangle + |111...111\rangle)$ with N identical qubits. The Hamiltonian evolves this state over time as $\frac{1}{\sqrt{2}}(|000...000\rangle + \exp(iN\zeta t)\,|111...111\rangle)$ [JKF$^+$09]. This means that such a state's relative phase evolves N times more quickly when compared to a solitary unentangled qubit. The maximum precision of such a measurement scales as $\Delta/N\sqrt{\nu}(|\lambda_1 - \lambda_0|)$ for N qubits [GLM06]. This is known as 'Heisenberg scaling', meaning that such sensitivities scale alongside the physical limits allowed by the Uncertainty Principle [BIWH96], recovering the time-energy uncertainty relation (hereafter referred to as the *Heisenberg limit*[1]) in the event that $\Delta = \hbar/2$.

It therefore appears as if entanglement is a natural and powerful resource for enhancing sensors, specifically using large states such as $\frac{1}{\sqrt{2}}(|000...000\rangle + |111...111\rangle)$, referred to as 'NOON' [WPA$^+$04], 'GHZ' [GHZ89] or 'cat' [KLMT00] states. In an optical environment, entanglement-enhanced sensors have been applied to interferometry [WPA$^+$04], where slight changes in a path length were discerned more sensitively with a four-photon entangled states over that of four lone, solitary photon qubits.

Although entanglement-enhanced optical interferometry was a powerful demonstration of quantum metrology, the method employed relied upon probabilistic operations. This means that increasing the size of the entangled state decreases the probability of success. Photon loss occurs throughout the entire experiment as well. Because of these characteristics, it has been shown that photons are not the best candidates for entanglement-enhanced technologies. For a given photon loss rate there is a maximum entangled state limit beyond which the information lost due to photon loss are not sufficiently compensated by the benefits of a few large entangled states [JKF$^+$09, BDDW09].

Other forms of quantum entanglement which are not subject to loss in the same way as photons, such as spins probed using magnetic resonance [JKF$^+$09, SJK$^+$10], use the entanglement resource more productively, even though NMR works in a regime of very low polarisation. Molecules controlled and measured using portable NMR systems are presently in use as local magnetometers in industry; this work characterises the quantum enhancements available for such measurements.

---

[1] These concepts of quantum metrology limits and scalings are often confused in the literature, where $1/N$ scaling is termed the 'Heisenberg limit' and $1/\sqrt{N}$ is termed the 'Standard Quantum Limit'.

4.1 Quantum metrology with mixed states

To quickly generate large states such as $\frac{1}{\sqrt{2}}(|000...000\rangle + |111...111\rangle)$, it is advantageous to choose molecules with a high degree of magnetic symmetry. The sensor molecules were chosen to have a *star topology*: a central spin-active nucleus (labelled A) distinct from, and coupled to, many magnetically equivalent outer spin-active nuclei (labelled B). The magnetic equivalence of the outer nuclei allows an experimentalist to address all external spins identically and easily, streamlining the NOON state creation. Example star-topology molecules able to support NMR-based quantum metrology include the 9 (hydrogen) +1 (centre phosphorus) spin TriMethylPhosphate (TMP), 12+1 spin TetraMethylSilane (TMS), and 27+1 Tris-(TrimethylSilyl)Phosphine (TTMSP)[2]. Visualisations of these molecules are shown in Figure 4.1.

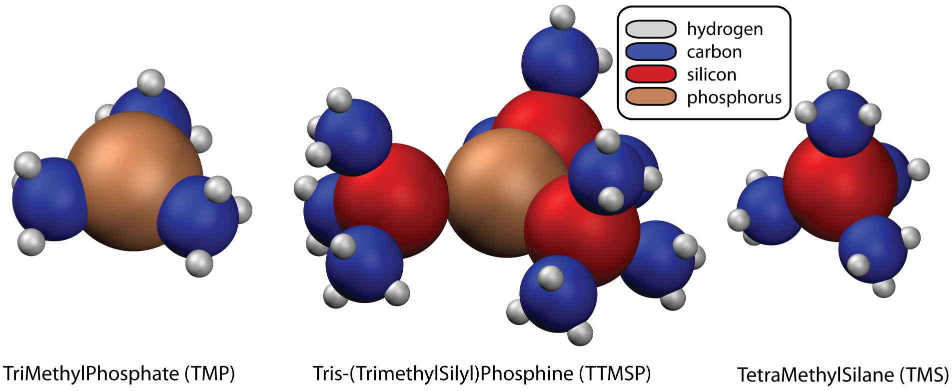

Figure 4.1: **Star topology sensors for quantum metrology.** Each of the illustrated chemicals have been used to demonstrate NMR-based entanglement-enhanced metrology. Each molecule was selected for its star topology: a central spin-active nucleus labeled A which is distinct and equivalently coupled to a collection of outer spin-active B nuclei.

To generate a NOON state with a star topology from the input pure state $|0\rangle^A |000...000\rangle^B$, one applies a coherence-generating $\frac{\pi}{2}^Y$ pulse on the centre spin A transforming the state into $\frac{1}{\sqrt{2}}(|0\rangle^A + |1\rangle^A) |000...000\rangle^B$, followed by a CNOT gate conditional upon A. The NOON state is left free to measure the magnetic field for a time τ, resulting in a state

---

[2] The work in this thesis will make use of TMS and TMP, the binomial distribution of spins is such that not all lines are visible in TTMSP spectrum without hundreds of averages per experiment.

$\frac{1}{\sqrt{2}}(|0\rangle^A|000...000\rangle^B + \exp(iN\zeta\tau)\,|1\rangle^A|111...111\rangle^B)$. To read out this phase, a reversal of the previous CNOT maps the acquired phase onto a coherence on spin A for readout, according to the state $\frac{1}{\sqrt{2}}(|0\rangle^A + \exp(iN\zeta\tau)\,|1\rangle^A)\,|000...000\rangle^B)$. Observed in a magnetic resonance spectrum, a pure-state sensor would be a single coherence (a single peak in the spectrum of spin A), whose phase would evolve at a rate of $N\zeta$.

Although elegant in its experimental simplicity, liquid-state NMR is a strongly mixed-state environment which introduces certain complications, drawbacks and advantages. Without a pseudopure preparation of the state, a $(\frac{\pi}{2})^Y_A$ pulse applied to a thermal state generates $N+1$ spectrum peaks, separated in frequency by the J-coupling J^{AB}, corresponding to the thermal (roughly binomial) distribution of up and down spins in the nearby B nuclei. We can assign a number, ℓ , to each of these lines corresponding to their *lopsidedness*, that is $\ell = u - d$ where u and d are the number of intramolecular up and down B spins, respectively. If the basic sensor sequence had been applied to a pseudopure state rather than the thermal state there would be one outermost peak to observe in the final spectrum. The alternative option of post-selecting the desired peak offers benefits. In addition to being computationally equivalent upon the peak of interest, the readout signal is stronger and the sequence time is shorter. A crucial advantage of this approach uses the fact that most of the internal peaks also pick up phase beyond the scaling of the Standard Quantum Limit proportional to their lopsidedness. The application of the sensor sequence to the internal lines generates states that are not quite 'NOON' states, and it is for this reason the term 'Many-Some, Some-Many' (or 'MSSM') was introduced [JKF$^+$09] to describe these states.

In this scheme the rate of phase acquisition by a peak identified by its lopsidedness ℓ is given by

$$\phi/\tau = \delta B(\ell\gamma_B + \gamma_A) + (\ell\delta_B + \delta_A) \tag{4.1.1}$$

for δB the field offset being measured, δ_A, δ_B the rotating frame magnetic field offsets for spin types A and B, τ the evolution delay and γ_A, γ_B the gyromagnetic ratios for spins A and B, respectively. It is usually assumed that an experimentalist can set $0 = \delta_A = \delta_B$.

For a given τ, each of the $N+1$ lines acquire a distinct phase ϕ. One could fit one of these lines to determine its acquired phase ϕ which in turn could be used to estimate a value for δB given that γ_B and γ_A are fundamental constants known with good precision. Alternatively, a line could be monitored as τ was varied over multiple shots, and its phase would oscillate with its corresponding frequency given by $\delta B(l\gamma_B + \gamma_A)/2\pi$. This signal could be Fourier-transformed to reveal a value for δB. Although the analysis is simpler in the latter method, it assumes environmental stability and requires many shots, leading to a smaller sensitivity enhancement per unit time. An experimental demonstration of both processing methods applied to data acquired by the TMS sensor is seen in Figure 4.2.

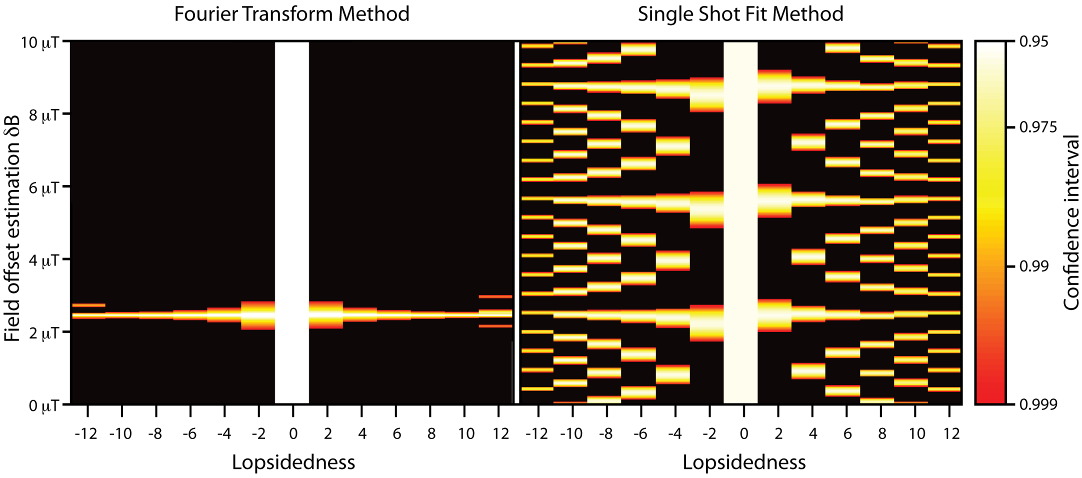

Figure 4.2: **Fourier transform and single-shot fit experimental processing methods.** In the left panel, a direct Fourier transform of a set of experimental field measurements over 512 equally spaced τ values reveals a field offset measurement for each line on the ^{29}Si spectrum of TMS. On inspection one can see that the outermost lines reveal a more sensitive measurement than the inner lines with a smaller lopsidedness. A normal-distribution fit of the Fourier-transformed line results in a confidence interval for each field estimate. In the right panel, a single τ slice can be fit to reveal a similar field estimate; at each fixed field offset one can fit the spectrum and record the fit's χ^2 value which in turn can be used to determine a confidence interval of the field estimate. Although the latter method is susceptible to aliasing, the inner lines reduce this aliasing dramatically and the information can be extracted in a single shot as opposed to over 512 scans.

We can extract many times more information with a single scan by considering all the peaks in the spectrum. A single NOON state sensor can easily encounter aliasing issues; an observer can not distinguish between 2π and 4π degree phase rotations which corresponds to very different magnetic fields. In effect one already needs to know the approximate field offset to be certain of one's results. A full arsenal of MSSM states, each peak corresponding to a lopsidedness value within $-N$ to N, provides a mechanism to largely avoid such problems. Each MSSM state acquires its own phase, and this complete set of output phases, its *signature*, is far less easily aliased. A ϕ degree phase rotation on the outermost peak is easily distinguished from an aliased 2ϕ degree rotation on the outermost peak by observing the phases of the inner MSSM states (See Figure 4.2). In fact, with an N-qubit quantum sensor, the complete signature corresponding to a ϕ phase rotation on the outermost peak could only be aliased with a rotation of $\phi + 2kN\pi$ for some integer k [SJK+10]. Alternatively phrased, these MSSM phase signatures have both the true upper limit in local phase distinguishability as well as the benefits of global distinguishability. Such anti-aliasing effects are a desirable property of these highly mixed symmetric sensor molecules.

4.2 RESOURCE ANALYSIS

Although mixedness in the observable component of the sample can be advantageous for anti-aliasing purposes, it seems to be a distinct disadvantage when considering the 'lost potential' of the unobservable component which makes up more than 99.9% of the sample in liquid-state NMR. Such a presentation of the resource is false. I will now show that the sensitivity increase of pseudo-entangled NOON states in NMR-based magnetometry can scale according to $\Delta/N^{3/4}\sqrt{\nu}(|\lambda_1 - \lambda_0|)$ for N qubits, and consequently that liquid-state NMR star-topology sensors with a binomial distribution of mixed states are able to outperform the Standard Quantum Limit scaling using unambiguously zero entanglement.

Given a defined set of resources — a certain measurement apparatus, a fixed type of particle, a set number of allowed repetitions, a given length of time — each of $\{\Delta, \nu, |\lambda_1 - \lambda_0|\}$ remain fixed, and the Heisenberg scaling in sensitivity is achieved if the precision of the parameter estimation scheme scales with $1/N$. This scaling of resources — and not the absolute variation of an individual measurement — is the metric used to determine any 'parameter-estimation speedup' offered by quantum metrology. All else being equal, a single electron with an accurately known g-factor can reveal a greater absolute sensitivity in a fixed unit of time than an optimal single pure entangled NOON state of 650 ^{1}H nuclei, simply due to differing gyromagnetic ratios (and hence differing $|\lambda_1 - \lambda_0|$). Yet for a sufficiently large enough N, an N-spin nuclear NOON state will outperform an ensemble of N isolated electron spins.

The low polarisation of the centre spin, in combination with the measurement of population differences, affects how these resources are considered. The sensitivity of the measurement — the variance of the estimate — does not vary with polarisation, however the low polarisation requires a large number of repetitions, given by ν, for detection. For a fixed ν, a pseudo-entangled NOON state could in principle scale with N according to the Heisenberg scaling in precision in the same way that entangled NOON state could. Having said this, for all else being equal, a more polarised (i.e. entangled) NOON state could require fewer ν to reveal this estimate.

Even though the low polarisation does not limit the scalability of star-topology liquid-state NMR sensors, the inherent binomial distribution of initial states does. The components of the sensor admitting maximum sensitivity — the outermost NOON lines — are only populated to one part in $1/2^N$, which only allows for slight asymptotic benefits when weighted with the sensitivities of the anti-aliasing, more populated MSSM lines. These precisions can be quantified explicitly.

The measurement error is bounded by the Cramer-Rao generalised uncertainty relation[3]

$$(\delta\zeta)(\delta\mathcal{H}) \geq 1/2\sqrt{\nu} \tag{4.2.1}$$

for $\delta\mathcal{H}$ the variance of the Hamiltonian acting upon the probe particles and $\delta\zeta$ the minimised variance of the measurement of ζ, the parameter under investigation [GLM06]. This expression can be generalised in a number of ways to include the full Fisher information in the state [BCM96], to account for noise and decoherence [SGMF10], to include the relative cost of all resources [TPS$^+$11], to optimally estimate time-dependent parameters [TWC$^+$11], or to properly account for the effects of post-selection, backaction and qubit loss [RPP$^+$07, BDDW09].

---

[3] This relation is a more general form of the Heisenberg Uncertainty Principle [STA59].

The Standard Quantum Limit scaling is reached with N isolated probe qubits in a superposition of eigenstates corresponding to the minimum and maximum eigenvalues:

$$(\delta\mathcal{H}_{\text{SQL}})^2 = \sum_{k=1}^{N} (|\lambda_1 - \lambda_0)|/2)^2 \tag{4.2.2}$$

$$\Rightarrow \delta\zeta \geq 1/\sqrt{N\nu}(|\lambda_1 - \lambda_0|) \tag{4.2.3}$$

The value of $\delta\mathcal{H}$ is maximised with N probe spins in a NOON state, so that $\delta\mathcal{H}_{\text{NOON}} = |(\lambda_{1111...111} - \lambda_{000...000})|/2 = |\ell_{\text{NOON}}(\lambda_1 - \lambda_0)|/2$, which gives an optimal variance $\delta\zeta = 1/N\sqrt{\nu}(|\lambda_1 - \lambda_0|)$. At this point it should be noted that there exist maximally entangled states of zero lopsidedness (such as a zero quantum coherence) that would not exceed nor even approach the scaling of the Standard Quantum Limit.

The value of $(\delta\mathcal{H})^2$ for a star-topology liquid state NMR sensor of N particles weighted according to its binomial distribution is given by:

$$(\delta\mathcal{H})^2 = \sum_{\ell=\{-N,-N+2,...,N\}} \binom{N}{(N+\ell)/2} \frac{(\ell|\lambda_1 - \lambda_0|/2)^2}{2^N} \tag{4.2.4}$$

For sufficiently large N, the binomial distribution coefficient can be approximated by the normal distribution:

$$\binom{N}{K}\frac{1}{2^N} \approx \sqrt{\frac{2}{\pi N}} \exp\left(\frac{(K - N/2)^2}{N/2}\right) \tag{4.2.5}$$

substituting, this with $K = (N + l)/2$ yields:

$$(\delta\mathcal{H})^2 = \frac{|\lambda_1 - \lambda_0|^2}{4} \sum_{\ell=\{-N,-N+2,...,N\}} \ell^2 \sqrt{\frac{2}{\pi N}} \exp\left(\frac{-\ell^2}{2N}\right) \tag{4.2.6}$$

If N is odd, then the centre line ($\ell = 0$) contributes no measurement precision. Hence without loss of generality we can assume N is even, recognise symmetry about $\ell = 0$ and evaluate for $x = \ell/2, x \in \{1, ..., N/2\}$ to get

$$(\delta\mathcal{H})^2 = \frac{|\lambda_1 - \lambda_0|^2}{4} \sum_{x=1}^{N/2} 8\sqrt{\frac{2}{\pi N}} \left[x^2 \exp\left(\frac{-2x^2}{N}\right)\right] \tag{4.2.7}$$

We define $\chi = x/N$ and note that in the limit of large N, $d\chi = dx/N = 1/N$ and we can approximate the above sum as a definite integral:

$$(\delta\mathcal{H})^2 = \frac{|\lambda_1 - \lambda_0|^2}{4}\frac{8\sqrt{2}N^{5/2}}{\sqrt{\pi}}\int_0^{1/2} d\chi\, \chi^2 e^{-2N\chi^2} \tag{4.2.8}$$

$$(\delta\mathcal{H})^2 = \frac{|\lambda_1 - \lambda_0|^2}{4}\frac{\sqrt{2}N^{5/2}}{\sqrt{\pi}}\frac{\left(\sqrt{2\pi}\mathrm{erf}(\sqrt{N/2}) - 2e^{-N/2}\sqrt{N}\right)}{N^{3/2}} \tag{4.2.9}$$

$$(\delta\mathcal{H})^2 \propto \frac{2N|\lambda_1 - \lambda_0|^2}{4} \text{ for large N.} \tag{4.2.10}$$

Therefore $(\delta\mathcal{H})^2$ scales with N (see Figure 4.3), and so a precision for ζ scales according to $1/N^{1/2}$ — at the Standard Quantum Limit scaling using entirely separable resources, but ultimately not near the Heisenberg scaling.

In this respect, moving to a higher polarisation can assist in a way more fundamental than increasing signal and reducing the effects of instrument noise; by allowing the state to be preferentially initialised into the NOON state one can recover the Heisenberg $1/N$ scaling. Alternatively, in the following section I introduce and analyse a preparation scheme that can be used to obtain $1/N^{3/4}$ scaling with room-temperature nuclear polarisation.

Other magnetic resonance sensors could in principle overcome the star topology's high-temperature limitations and scale according to the Heisenberg scaling. In a single-sensor temporal ensemble, one has the opportunity to project the state into a pure state in advance of field sensing by measurement. From this known initial state one could potentially manipulate the state into one wielding maximal sensitivity. The resource analysis and pulse sequences presented here would apply equivalently to a single sensor where ν would represent the number of measurement repetitions, which would minimise the sensor backaction on the environment. An example single-system two-qubit sensor that could benefit from this approach are electron-nucleus qubit pairs in nitrogen-vacancy (NV) centres in nano-diamonds (as readout spins) coupled to external electrons stationed on the nano-diamond's surface. This entanglement-boosted sensor could be placed at an AFM tip, a technique under development, to quickly enhance the sensitivity of the NV centre.

The above discussion of scalability has tacitly assumed that decoherence is not correlated with the sensor size N. If instead the dephasing time τ_N^* of a pure NOON state scales with N, such that $\tau_N^*/\tau_1^* = N^{-p}$ for some $0 < p \leq 2$, a different picture emerges [SGMF10]. If $1 \leq p \leq 2$, the quantum method almost never outperforms the classical method in sensitivity due to loss of signal[4], and if $0 \leq p < 1$ there exists an optimal field-measurement time τ such that the precision scales like $1/N^{1-p}$. In the 13-spin TMS cat state metrology experiments, p was measured to be ≈ 0.11. This reduces the overall scaling bound to $\approx 1/N^{2/5}$ — below the scaling of the Standard Quantum Limit.

4.3 BOOSTING SENSITIVITY VIA STATE PREPARATION

The basic sensor sequence was designed with NOON states in mind, and although it performs admirably when applied to the inner MSSM lines, the sequence was not designed to optimise the performance of the total mixed-state sensor. To do so, consider the thermal distribution in the basis $\{|0\rangle^A, |1\rangle^A\} \otimes \{|K\rangle^B\}_{\{K=0,\ldots N\}}$. The population ratio between the ground state $|0\rangle|0\rangle$ and $|0\rangle|K\rangle$ is given by $\binom{N}{K}\exp(-\gamma_B\mu_N B_0/k_B T)^K := \binom{N}{K}\Gamma_B^K$. Similarly the population ratio between $|0\rangle|K\rangle$ and $|1\rangle|K\rangle$ is given by Γ_A. Consequently the unnormalised diagonal thermal density matrix can be expressed as:

$$\rho_{\text{thermal}} = \sum_{\{K=0,\ldots N\}} \binom{N}{K}\Gamma_B^K|0K\rangle\langle 0K| + \sum_{\{K=0,\ldots N\}} \binom{N}{K}\Gamma_B^K\Gamma_A|1K\rangle\langle 1K| \tag{4.3.1}$$

In this presentation we can see that the readout spin A is approximately binomially distributed with a polarisation difference proportional to $(\Gamma_A - 1)$. To maximise the overall sensitivity of A we should consider ways to simultaneously make use of Γ_B^K — a resource that in general scales quite favourably with N. To introduce the term Γ_B^K into a population difference measurement on A a conditional operation is required. The simplest of these, a CNOT pulse on B conditional on the state of A at the outset of the sequence, optimises the performance of the sensor [MWCV10]. It transforms the thermal populations into

$$\rho_{\text{primed}} = \sum_{\{K=0,\ldots N\}} \binom{N}{K}\Gamma_B^K|0K\rangle\langle 0K| + \sum_{\{K=0,\ldots N\}} \binom{N}{N-K}\Gamma_B^{N-K}\Gamma_A|1K\rangle\langle 1K| \tag{4.3.2}$$

---

[4] With full FID measurements this is strictly true; if one could reset and re-run the experiment after having gathered the leading 'useful' component of the FID slight enhancements with $p > 1$ are possible.

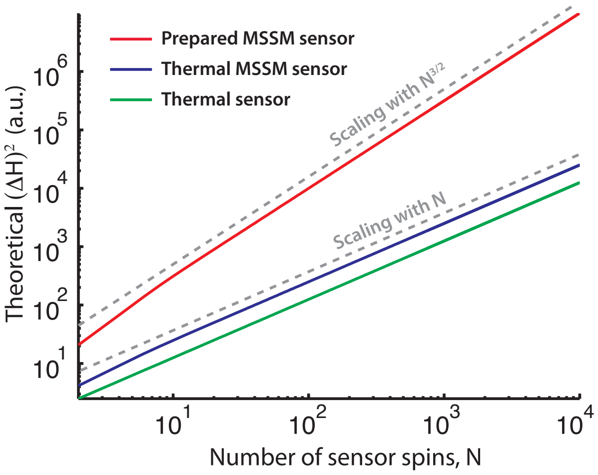

Figure 4.3: **Enhancing sensor sensitivity through state preparation: theory.** The theoretical value for $(\delta\mathcal{H})^2$ for the thermal sensor and the prepared sensor scales with N and $N^{3/2}$, respectively, leading to a sensivitiy scaling of $1/\sqrt{N}$ and $1/N^{3/4}$, respectively. By preparing the thermal state into the pseudo-entangled MSSM state, one outperforms the unentangled spin resource but $(\delta\mathcal{H})^2$ still scales with N. By preparing the MSSM sensor one surpasses the scaling of the Standard Quantum Limit with unambiguously zero entanglement.

Consequently the amplitude magnification of the population difference along a particular line indexed by K (and lopsidedness $\ell = N - 2K$) is given by

$$A(K) = \frac{\binom{N}{N-K}\Gamma_B^{N-K}\Gamma_A - \binom{N}{K}\Gamma_B^K}{\binom{N}{K}\Gamma_B^K\Gamma_A - \binom{N}{K}\Gamma_B^K} \tag{4.3.3}$$

$$= \frac{(\Gamma_B^\ell\Gamma_A - 1)}{(\Gamma_A - 1)} \tag{4.3.4}$$

To constant order in Γ_A, Γ_B (valid for low polarisations), this becomes

$$A(\ell) = (1 + \gamma_R \ell) \tag{4.3.5}$$

where $\gamma_R = \gamma_B/\gamma_A$ is the ratio of the two species' gyromagnetic ratios.

This means the outermost lines — the most sensitive components of the sensor with the poorest thermal populations — are those most amplified by the CNOT operation[5]. This amplification was measured experimentally in the thirteen-spin TMS sensor where

---

[5] In the case of $N = 1$ with NMR, this is known as Insensitive Nuclei Enhanced by Polarisation Transfer (INEPT) [Sør89, MF79].

$|\gamma_R| \approx 5$, and the integrated intensities of the outermost lines displayed an approximately sixty-fold increase over the thermally-polarised measurement as expected. From this amplified state the original NOON sequence can be applied, with a rate of phase acquisition proportional to ℓ as before. This amplification can be seen in Figure 4.4.

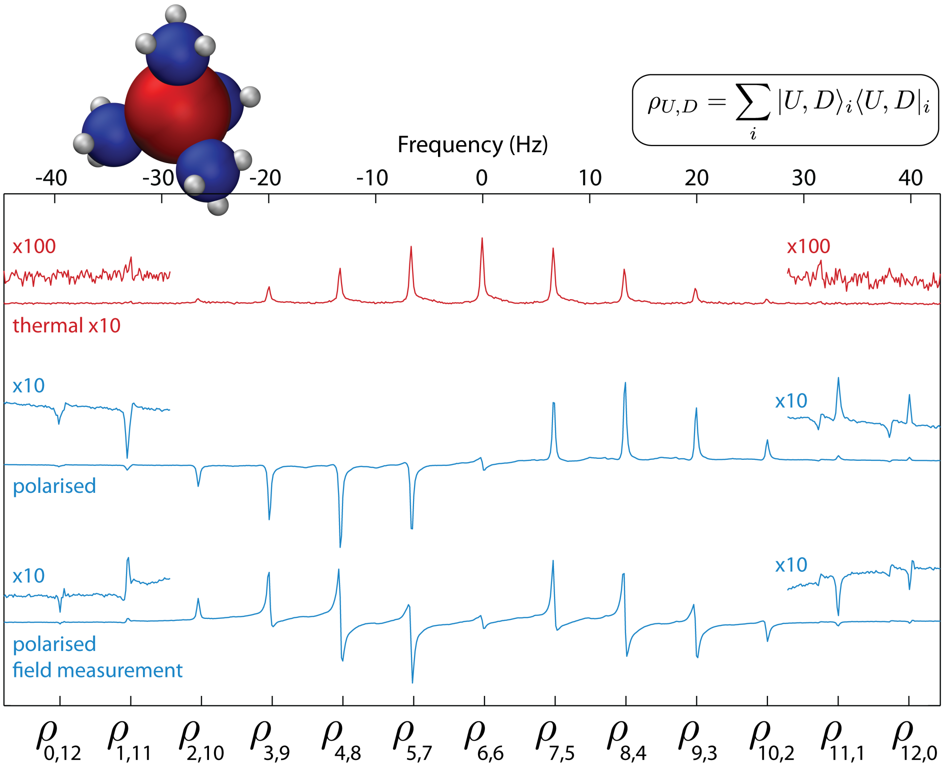

Figure 4.4: **Enhancing sensor sensitivity through state preparation: experiment.** The top trace is a single shot spin-echo readout of TMS (shown above) in a thermal equilibrium state. Each of the star-topology sensors admit a simple state preparation sequence which not only amplifies the overall signal by $|\gamma_R|$ (≈ 5 for TMS), but also by each peak's lopsidedness, as seen in the middle trace. This prepared state can be used for field measurement as shown in the bottom trace, where the acquired phase on each peak can be used to deduce the field offset.

As one would anticipate, by linearly amplifying the MSSM lines according to their lopsidedness, one obtains an enhanced overall sensitivity. The expression for $(\delta\mathcal{H})^2$ with this primed sensor, approximating $A(\ell) \approx \gamma_R \ell$ is given by:

$$(\delta\mathcal{H})^2 = \frac{|\lambda_1 - \lambda_0|^2}{4} \sum_{x=1}^{N/2} 8\gamma_R \sqrt{\frac{2}{\pi N}} \left[x^3 \exp\left(\frac{-2x^2}{N} \right) \right] \tag{4.3.6}$$

As before, let $\chi = x/N$ and note that in the limit of large N, $d\chi = dx/N = 1/N$ to arrive at the integral:

$$(\delta\mathcal{H})^2 = \frac{|\lambda_1 - \lambda_0|^2}{4} \frac{8\gamma_R \sqrt{2} N^{7/2}}{\sqrt{\pi}} \int_0^{1/2} d\chi \, \chi^2 e^{-2N\chi^2} \tag{4.3.7}$$

$$(\delta\mathcal{H})^2 = \frac{|\lambda_1 - \lambda_0|^2}{4} \frac{\gamma_R \sqrt{2} N^{7/2}}{\sqrt{\pi}} \frac{(2 - e^{-N/2}(N+2))}{N^2} \tag{4.3.8}$$

$$(\delta\mathcal{H})^2 \propto N^{3/2} \gamma_R 2\sqrt{2/\pi} \frac{|\lambda_1 - \lambda_0|^2}{4} \text{ for large N.} \tag{4.3.9}$$

This expression leads to a sensitivity scaling of $1/N^{3/4}$ — midway between the Standard Quantum Limit scaling and the Heisenberg scaling of $1/N$, or for the case where the dephasing rate $p > 0$, a scaling of $1/N^{3/4-p}$. This shows that entanglement is not necessary for metrology enhancements beyond classical limitations, which agrees with independent findings elsewhere [BDF$^+$08].

4.4 Protecting against error

Above we explored how a modified sequence can increase a sensor's precision. Next we further develop the sequence to simultaneously increase its accuracy.

Instrumentally, there is always some error associated with imperfect frequency detunings. Equation 4.1.1 assumes that the frequencies of the A and B channels are precisely on resonance ($\delta_B = \delta_A = 0$) with their respective nuclei at the nominal field strength. Recall that, without this assumption,

$$\phi/\tau = \delta B(\ell\gamma_B + \gamma_A) + (\ell\delta_B + \delta_A) \tag{4.4.1}$$

where δ_B and δ_A are the frequency offsets of the nuclei at the nominal field. One can mitigate the errors generated by these terms by systematically removing them. One of these offsets (here assumed to be δ_B) can be eliminated by shifting the nominal field, but it is only possible to remove both terms if the frequencies are set perfectly. An imprecisely known rotating frame offset leads to inaccurate field estimations, as seen in Figure 4.5. This requirement can be removed by *disentangling* the centre spin during the phase acquisition delay [SJK$^+$10]. Two methods for achieving this are introduced in Figure 4.6.

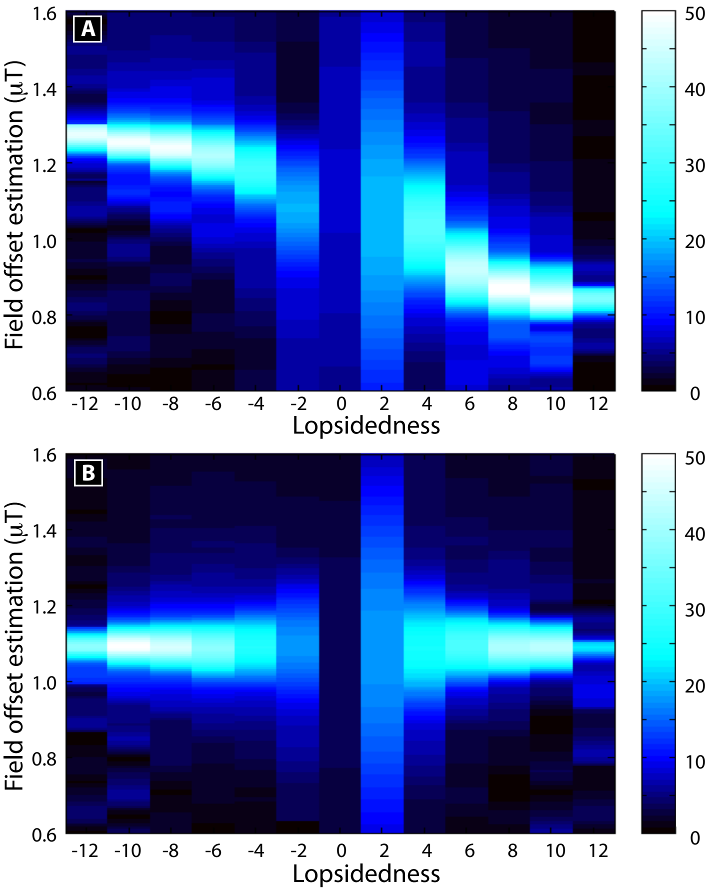

Figure 4.5: **Errors and disentangling spins.** The colour axis applied to each peak reflects its amplification with respect to a thermal binomial amplitude. The field measurement itself is more sensitive, but the accuracy of the measurement can still be corrupted through incorrectly set rotating frames, and shown in the top panel. If the centre A spin can be disentangled from the field measurement B spins during the sequence, these offset differences become irrelevant and a more accurate estimation is recovered, as shown in the bottom panel.

Consider how the sequence I acts upon the state $|0\rangle_A |0\rangle_B^{\otimes(N-1)}$. A Hadamard gate followed by a CNOT gate conditional upon spin A transforms the initial state into $|0\rangle_A |0\rangle_{\mathrm{H}}^{\otimes(N-1)} + |1\rangle_A |1\rangle_B^{\otimes(N-1)}$. It is here that we can disentangle the central A spin from our large cat state by applying a NOT gate to A in the second term, giving

$$|0\rangle_A |0\rangle_B^{\otimes(N-1)} + |0\rangle_A |1\rangle_B^{\otimes(N-1)} = |0\rangle_A \left(|0\rangle_B^{\otimes(N-1)} + |1\rangle_B^{\otimes(N-1)} \right) \tag{4.4.6}$$

so that only the B spins acquire field-dependent phases.

Basic Sequence:

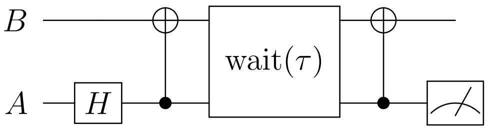

(4.4.2)

Primed Sequence:

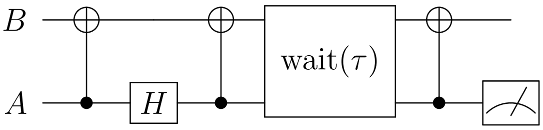

(4.4.3)

Disentangling Sequence I:

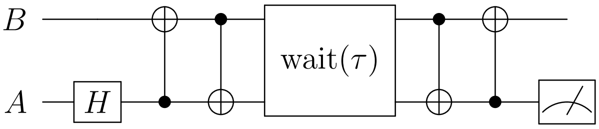

(4.4.4)

Disentangling Sequence II:

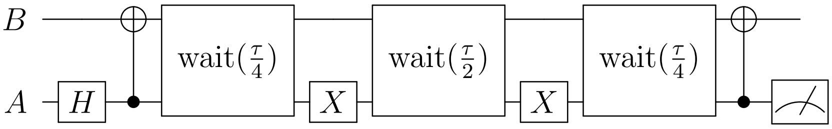

(4.4.5)

Figure 4.6: **Quantum metrology sequences.** The basic sequence for implementing quantum metrology is introduced in the top panel. This sequence is improved by priming the state with a leading CNOT gate, as shown in the second panel. Disentangling sequences can be used to remove the errors connected with different rotating frames set for the A and B spins. The simple disentangling sequence I can be used for sensors with an odd number of outer B spins. A more general disentangling sequence II can be used for both even and odd spin systems. The priming CNOT and disentangling sequences are compatible and can be applied simultaneously.

It might seem that this approach would require a multiply-controlled NOT gate (a generalised Toffoli gate), but this is not strictly required. It is only necessary to apply a NOT gate to the second term and not to the first term. This could be achieved with a modified CNOT gate [Jon01], with an evolution time chosen to match $(2NJ^{AB})^{-1}$, corresponding to the separation between the outermost lines in the A spin spectrum.

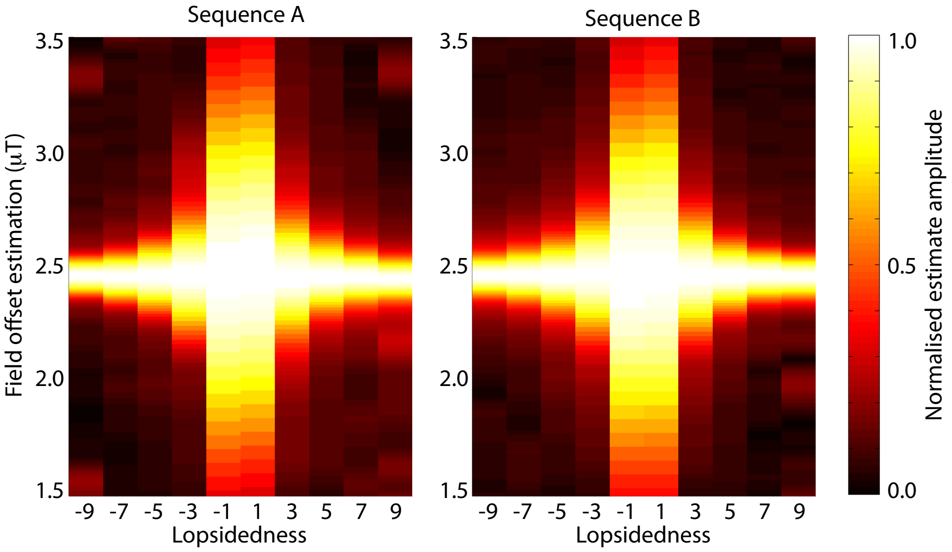

Figure 4.7: **Comparing the two disentangling sequences.** Both disentangling sequences I and II were applied to the TMP sensor to confirm their experimental equivalence. In both instances, large (1 kHz) offsets were applied to the central A spin, and the Fourier transform method was used to extract the field estimate.

Unfortunately, the phases acquired by the inner MSSM lines become difficult to decipher if this is applied.

Any odd multiple of $(2NJ^{AB})^{-1}$ can also disentangle the two outermost lines, and so in the case where there are an odd number of B spins, this can be accomplished with a regular CNOT gate of delay $1/2J^{AB}$. This approach works with a general set of MSSM lines; a conventional CNOT gate (shown as sequence I in Figure 4.6), disentangles every MSSM line. This approach does not work for systems with an even number of B spins. An alternative, simpler method (sequence II in Figure 4.6) uses echoes to refocus the A spin rather than disentangling it, and this can be applied to both even and odd systems. Under both sequences the acquired phase is measured by applying the sequence in reverse and recording the spectrum of the central A spin.

To test this approach, we applied a small offset to the A spin and implemented a full field estimation with the original pulse sequence and with the modified sequence II. As shown in Fig. 4.5, the field estimation now gives different results for different lines in the multiplet if the original sequence is used, but these imperfections are removed by the modified sequence. Sequences I and II were both successfully implemented [SJK^{+}10]

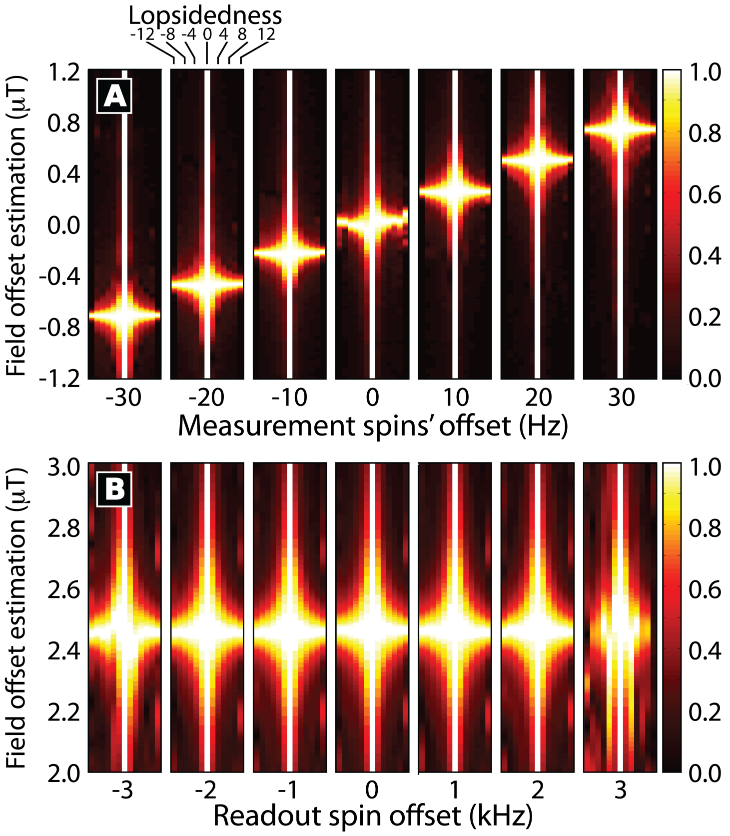

Figure 4.8: **Robustness of sensor disentangling sequence.** To demonstrate the robustness of the disentangling sensor sequence II, we tested it with a range of A and B spin detunings. Each panel in both figures is labelled according to its deliberate detuning. In the top figure, the B spin detunings amount to a different field offset estimation as predicted; in the bottom figure the range of A spin detunings display no corruption of that field estimation within the bandwidth of the applied pulses (±2 kHz).

with the same environmental parameters on the original odd spin system, TMP (See Figure 4.7).

Using TMS, we verified the robustness of the second disentangling sequence by testing it against a range of deliberate B spin detunings to ensure that the accuracy of the sensor was unaffected by the disentangling sequence. We then repeated the phase estimation with a wide range of A spin detunings (See Figure 4.8) and obtained indistinguishable field estimations up to the point where the pulses' bandwidths compromised the fidelity of the sequence. This confirmed that the disentangling sequence is robust against very large offset errors, making the sensor more reliable and easier to deploy.

§ 5. State Preparation

In general, the thermal state is not necessarily the optimal initial state to meet the goals of a given quantum sequence. We have seen how unitary state preparation can have a considerable impact on the quality of the output in Section 4.3; in this chapter we will explore preparation strategies employing nonunitary processes for quantum information.

The collection of available nonunitary processes are material-dependent and fall into the categories of passive relaxation processes and active user-driven processes such as optical illumination or continuous microwave irradiation. By identifying and understanding the specific mechanisms underlying these (often temperature, orientation and field-dependent) processes, one can optimally prepare the state, maximise the available T_2 times (to boost overall sequence fidelity) and minimise the repetition rate of the sequence.

In this chapter the qubits under investigation are dilute ($< 10^{15}$ cm^{-3}) donor atoms, namely ^{31}P ($m_I = 1/2, \mathcal{A} = 117.53$ MHz) and ^{209}Bi ($m_I = 9/2, \mathcal{A} = 1.4754$ GHz), hosted in crystalline silicon. These donors have energy levels in the semiconductor band gap of silicon, sitting slightly under the conduction band with binding energies of 45 meV and 70 meV, respectively. These are hydrogen-like defects in an indirect semiconductor host, and although the ideas developed here are largely tailored towards group V donors in crystalline silicon, many of these relaxation mechanisms have a broader applicability to semiconductor defects or hydrogenic sites in general.

5.1 Spin-lattice relaxation in silicon

The rate of a particular nonunitary T_1 process which moves a qubit from one time-independent Hamiltonian $\mathcal{H}_0$ eigenstate, $|0\rangle$, into another, $|1\rangle$, comes about from Fermi's Golden Rule applied to processes which are slower than coherences' lifetimes. This determines the transition probabilities via the mixing of the two $\mathcal{H}_0$ eigenstates under the perturbed Hamiltonian $\mathcal{H} = \mathcal{H}_0 + \mathcal{H}_1$, both directly to each other ($\langle 1|\mathcal{H}_1|0\rangle$) through first-order processes and via other intermediate states ($\langle 1|\mathcal{H}_1|2\rangle\langle 2|\mathcal{H}_1|0\rangle$) as second-order processes, where $|2\rangle$ may lie outside the restricted Hilbert space of interest. The perturbation $\mathcal{H}_1$ can include information about the frequency and strength of user-driven active processes, spin-spin and spin-orbit couplings, the density of thermally-generated phonons, field fluctuations and more.

To employ relaxation processes for optimal state initialisation, they should be well understood. Relaxation rates in ^{28}Si:P vary tremendously with field and temperature, which can also play a part in the optimisation process of a particular quantum algorithm. There are three main T_{1E} relaxation processes which dominate in different magnetic field and temperature ranges: the direct process, the Orbach process, and the Raman process. Each of these processes rely upon phonons that are either directly or indirectly resonant with the energy splitting of the electron.

To understand which indirect processes can play a role, one must understand the energy level structure of donors in unstrained silicon. The ground state of hydrogenic donors form just below the conduction band minimum, which in k-space is sixfold degenerate about the $k = 0$ point, along all crystal axes equivalent to the (1,0,0) crystallographic direction. This implies that the donors' electronic energy states are formed out of six equivalent ellipsoids about the $k = 0$ point, and because all electronic wavefunctions must conform to the tetrahedral symmetry of the lattice, the 1s ground state is sixfold degenerate as well. The six 1s states can be broken apart into singlet, doublet and triplet states. The singlet is an even superposition of all six ellipsoids (a member of the "A" symmetry point group), triplets are an odd superposition of two coaxial ellipsoids (and are themselves threefold degenerate (of the "T$_2$" point group), and the doublets are the two remaining antisymmetric orthogonal combinations (of the "E" point group). The singlet, doublet and triplet states each experience a different potential due to the nucleus; both phosphorus and bismuth have low-lying 1s:A states which, when split due to the Zeeman interaction, make up the qubit ground state. Due to parity it is only the 1s:A state which experiences a hyperfine splitting with the nucleus.

These energy level considerations are important because at higher temperatures the

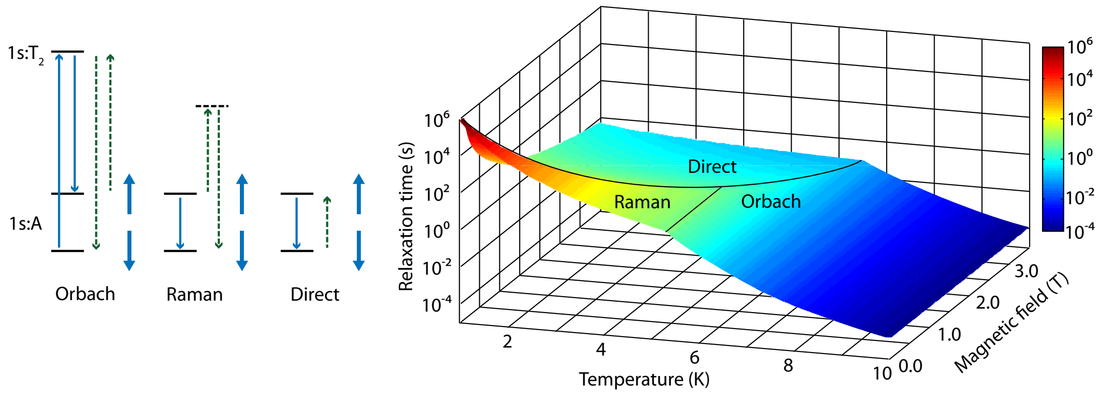

Figure 5.1: **Phase diagram of electron spin-lattice relaxation in ^{28}Si:P.** Raman, Orbach and direct relaxation processes each drive electronic relaxation by exchanging energy with phonons. In each instance, a change in the electron spin (indicated by blue arrows) occurs alongside an equal and opposing change of total phonon energy (indicated by green dashed arrows). These three processes dominate at different temperatures and magnetic fields; an approximate phase diagram for ^{28}Si:P illustrates these regions. The colouring and vertical scale indicates the relaxation time, plotted on a logarithmic scale as shown. Bismuth donors also adhere to these three processes, however the Raman region is thought to dominate this range of fields and temperatures.

electron can be excited into the next lowest-lying 1s state, 1s:T$_2$, by absorbing a phonon. It can later relax back into either the spin-up or spin-down 1s:A state by emitting a second phonon, which indirectly allows T_{1E} relaxation. This process is known as the *Orbach* process. The density of phonons at the *crystal field splitting*, the energy difference Δ between 1s:A and 1s:T$_2$, determines the probability of this two-phonon process, and consequently the rate scales according to $1/T_{1E} \propto \exp(-\Delta/T)$. Phosphorus donors have $\Delta = 11.6$ meV, and bismuth donors have $\Delta = 34$ meV; this contributes to a much longer T_{1E} time for bismuth donors over phosphorus donors in the Orbach regime. The Orbach process is independent of field, concentration (below $\approx 10^{16}$ donors cm^{-2}) and orientation. For phosphorus and bismuth donors, this process dominates above the temperatures of 6 K and 26 K, respectively [Cas67].

In addition to the case where two sequential first-order perturbations (phonon absorption and emission) flip the electron spin, a phonon can alternatively undergo a single second-order process and change the electron's spin state by scattering off the electron spin via a virtual excited state. In this instance the phonon's change in energy equals the Zeeman spin splitting of the 1s:A orbital state. The phonons which contribute are not limited to those with an energy of Δ; any phonons can contribute to this process provided that the change in energy equals the Zeeman splitting. This process is known as the *Raman* process, and scales according to $1/T_{1E} \propto (\alpha T^9 + \beta B_0^2 T^7)$. As with the Orbach process, the T^9 Raman component is independent of field, concentration and orientation. For phosphorus donors, $1/T_{1E} \propto T^9$ in the temperature range of 2.5 K – 6 K [Cas67] at 9.5GHz (0.35T). The relaxation rate $1/T_{1E}$ of bismuth donors in natural silicon have been shown to display a T^7 dependence in the temperature range of <8 K – 26 K at 9.5 GHz [GWR$^+$10, CJ63].

The *direct* process is a first-order process whereby phonons with the same energy as the 1s:A Zeeman splitting are directly absorbed and emitted. This process depends upon the magnetic field ($1/T_{1E} \propto B_0^4 T$) and crystal orientation. The direct process dominates at the lowest temperatures where these low-energy excitations are more populated than the larger ones necessary for Raman or Orbach excitation. For phosphorus donors, this process dominates below 2.5 K at 9.5 GHz and at correspondingly higher temperatures when working with higher magnetic fields. The crossing-point for bismuth donors has not yet been identified, although evidence suggests that it lies lower than 5 K at 240 GHz (8.4T) [MWS$^+$10]. A visual representation of these three mechanisms and the resulting relaxation times for Phosphorus donors is seen in Figure 5.1.

5.1.1 CROSS RELAXATION

Although group V donors in silicon each respond to the effects of Orbach, Raman and direct relaxation, the specific values for T_{1E} between donors can vary widely even when compared at the same magnetic fields, temperatures and orientations. Similarly the other T_1 processes in the system, namely the nuclear relaxation rate T_{1N} corresponding to $|\Delta m_S| = 0, |\Delta m_I| = 1$, and the cross relaxation rate T_{1X} corresponding to the 'flip-flop' transition $\Delta m_S \mp 1, \Delta m_I \pm 1$ and the remaining rate T'_{1X} corresponding to the 'flip-flip' transition $\Delta m_S \pm 1, \Delta m_I \pm 1$ (see Figure 5.2), differ dramatically between bismuth and phosphorus donors. Specifically, phosphorus donors exhibit weak cross relaxation compared to T_{1E}, whereas bismuth donors show much stronger cross relaxation compared to T_{1E}.

This can be understood by examining the transition probabilities due to the hyperfine interaction. The hyperfine term is not diagonal in the spin product basis but rather of the form $\sigma_X \otimes \sigma_X + \sigma_Y \otimes \sigma_Y + \sigma_Z \otimes \sigma_Z$. Such a term contributes to transition probabilities across T_{1X} transitions. By diagonalising the full Hamiltonian at various frequencies one can calculate the resulting mixture of spin product terms in the proper eigenbasis of the full Hamiltonian. At 9.5 GHz and 95 GHz phosphorus eigenstates across T_{1X} transitions are 1% and 0.1% spin mixtures, respectively, whereas bismuth donors are 16% and 1.6% spin mixtures. Even at 240 GHz, bismuth eigenstates across T_{1X} transitions are 0.6% spin mixtures.

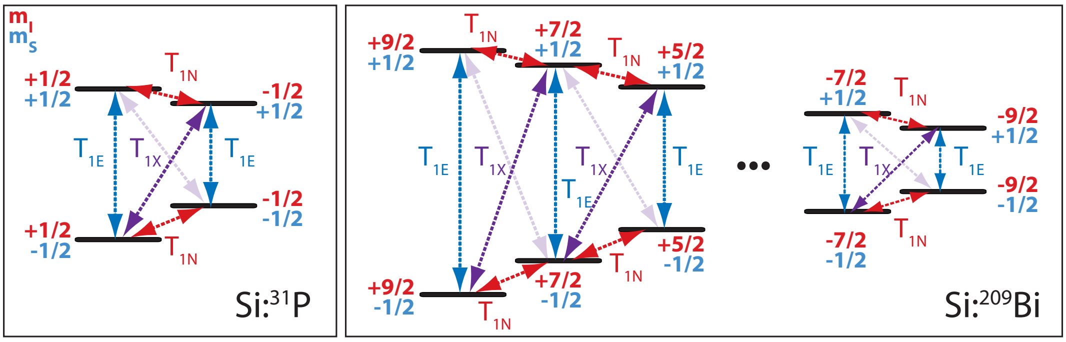

Figure 5.2: **Cross relaxation with donors in silicon.** Spin eigenstates are designated by their m_S (blue) and m_I (red) values. The T_{1E} and T_{1N} single spin-flip transitions are indicated by blue and red arrows, respectively. In addition there exists cross relaxation mechanisms which simultaneously flip a nucleus and an electron. The dark purple $\Delta m_S \mp 1, \Delta m_I \pm 1$ 'flip-flop' T_{1X} transitions conserve angular momentum and connect eigenstates that are slightly mixed due to the hyperfine interaction. Consequently, relaxation along flip-flop transitions is more likely than across the related $\Delta m_S \pm 1, \Delta m_I \pm 1$ 'flip-flip' transitions. To illustrate this, flip-flip transitions are paled in comparison to flip-flop transitions in the energy level diagrams of both phosphorus- and bismuth-doped silicon.

We can use both the relative strength or absence of T_{1X} for efficient state initialisation. Both when $T_{1X} >> T_{1E}$ and $T_{1X} \approx T_{1E}$ the electron polarisation can be used to temporarily enhance the system's nuclear polarisation while largely maintaining its electron polarisation. This amounts to an overall lower spin entropy, corresponding to a higher purity initial state, which brings more quantum states within reach given a fixed thermal spin entropy. These enhancements can be quite significant; at low temperatures the reduction in spin temperature can nearly double the purity of the state.

5.1.2 NUCLEAR SPIN-LATTICE RELAXATION IN ^{28}SI:P

The T_{1X} process is comparatively not well understood in this dilute, low-temperature regime. NMR detection is not sensitive enough to detect such low concentrations, and so pulsed EPR techniques of measuring T_{1X} must be used. The principle difficulty in measuring T_{1X} are the long timescales involved; T_{1X} exceeds hours at low fields and temperatures. These long relaxation times are not to be avoided: if the sequences are designed to return the state to thermal equilibrium there are minimal repetition rate limitations, and long timescales are an opportunity for exceptionally long T_{2N} times. Recent results indicate that ^{28}Si:P nuclei exhibit T_2 times exceeding 150 s [The11] which is at least an order of magnitude larger than current competing qubits' best T_2 times. Understanding the mechanisms driving nuclear relaxation is important not just for identifying an optimal working point; it may be possible to manipulate these mechanisms to further improve the nuclear qubit. This section explores nuclear relaxation in ^{28}Si:P. A ^{28}Si-enriched bismuth sample is currently in preparation, and comparative measurements of T_{1X} are a subject of future study.

As explained in Section 3.6, pulsed techniques measure the shorter of the two relaxation times $\{T_{1N}, T_{1X}\}$, at a given field and temperature. In contrast, continuous-wave measurements are in principle able to determine the ratio of T_{1X}/T_{1N} through the amplitude of polarisation buildup of Overhauser nuclear polarisation, which is discussed in Section 5.2.1. Evidence of this polarisation buildup [FG59] at 1.25 K and 9 GHz suggests that $T_{1X} << T_{1N}$, and this tacit assumption is made for ^{28}Si:P in the discussions to follow. Further study confirming this relationship as a function of field and temperature may provide insight into the nuclear spin dynamics of donors in silicon.

In ^{28}Si:P, preliminary results have shown that T_{1X} is approximately 10 – 1000 times greater than T_{1E} in the temperature range of 1 K – 8 K at a frequency of 9.5 GHz. Specifically, $T_{1X}/T_{1E} \approx 700$ in the Orbach regime and $T_{1X}/T_{1E} \approx 2T^2$ at temperatures below this (See Figure 5.4). We will consider each of these regimes in turn.

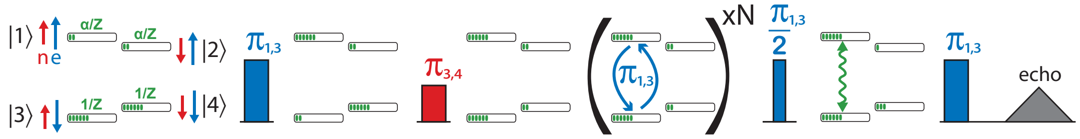

Figure 5.3: **Sequence to test nuclear relaxation via the electron's time-varying spin state in ^{28}Si:P.**

Given that the nuclear relaxation time roughly follows the electronic relaxation time in the Orbach regime, a natural hypothesis is that a change in the electron spin orientation corresponds to a time-varying local magnetic field which, with some probability, flips the nuclear spin through the T_{1X} transition. This hypothesis could be tested by driving the electron with an increasing number of electronic π pulses after an ENDOR sequence without a tidy pulse in the saturation regime (T_{1E} << shot repetition time << T_{1X}). Such a sequence attempts to drive nuclear relaxation through an increasing number of electron spin flips. Explicitly, this sequence is given in Figure 5.3.

For $N = 0$, this sequence reveals a negative echo in the saturation regime. If the changing electron magnetic moment relaxes the nucleus, a recovered ENDOR signal should be observable as N gets sufficiently large. This test was performed and no observable nuclear relaxation was observed for up to 2^{10} electronic π pulses, indicating that the source of nuclear relaxation is not directly due to the electron's time-varying spin state in the Orbach regime.

Alternatively, the nucleus could be relaxing due to the electron's time-varying orbital spin state. The nucleus experiences Orbach, Raman and direct electronic relaxation differently. Notably, in the Orbach process, the electron moves briefly into the 1s:T$_2$ level which does not have a hyperfine interaction. In the direct and Raman processes, the hyperfine value remains constant. To investigate the relationship between hyperfine modulation and nuclear relaxation, one can forcibly modulate the hyperfine through the application of light.

5.1.3 Optically-driven relaxation of ^{28}Si:P

If the wavelength of the light is restricted to energies much less than the bandgap of silicon (< 1.17 eV or wavelengths > 1060 nm), the donors' electrons absorb the photons and are excited into the conduction band. These carriers exist for some time in the conduction band during which they undergo spin relaxation which is faster than the dark T_{1E} processes due to their spin-orbit interaction. When the conduction electrons recombine with ionised donors they effectively relax the electron ensemble. This relaxation process differs significantly from the Orbach process, however in principle a comparison of T_{1X} and T_{1E} with and without the application of ionising laser light as a function of temperature can help determine if the hyperfine modulation is contributing to nuclear relaxation in ^{28}Si:P. A summary of spin-lattice relaxation times measured both in the dark and illuminated with 1550 nm laser light can be seen in Figure 5.4.

Although the ratio of $(T_{1X}/T_{1E})_{1550}$ roughly matches $(T_{1X}/T_{1E})_{\text{dark}} \approx 700$ in the Orbach regime, these data can be used to argue that the enhanced relaxation due to 1550 nm illumination in the Orbach regime is not directly due to hyperfine modulation. The first evidence in support of this is the temperature dependence of $(T_{1X})_{1550}$. Given a constant laser power incident on the sample, a constant number of donors should be ionised because the *capture rate constant* — the probability of a ionisation event — is independent of temperature. Assuming the same incident power at each point, this indicates that roughly the same number of donors would be ionised at each temperature and so the ionisation step is not itself responsible for the shorter $(T_{1X})_{1550}$. The second stage in the ionisation process — the expected time for which a nucleus remains ionised and experiences no hyperfine interaction — is a function of the recombination rate of the carriers. This rate is proportional to the velocity of the carriers which does depend upon the temperature according to $T^{1/2}$ [LH61], however this weak scaling is insufficient to explain the strong temperature dependence of $(T_{1X})_{1550}$ in the Orbach or Raman regimes.

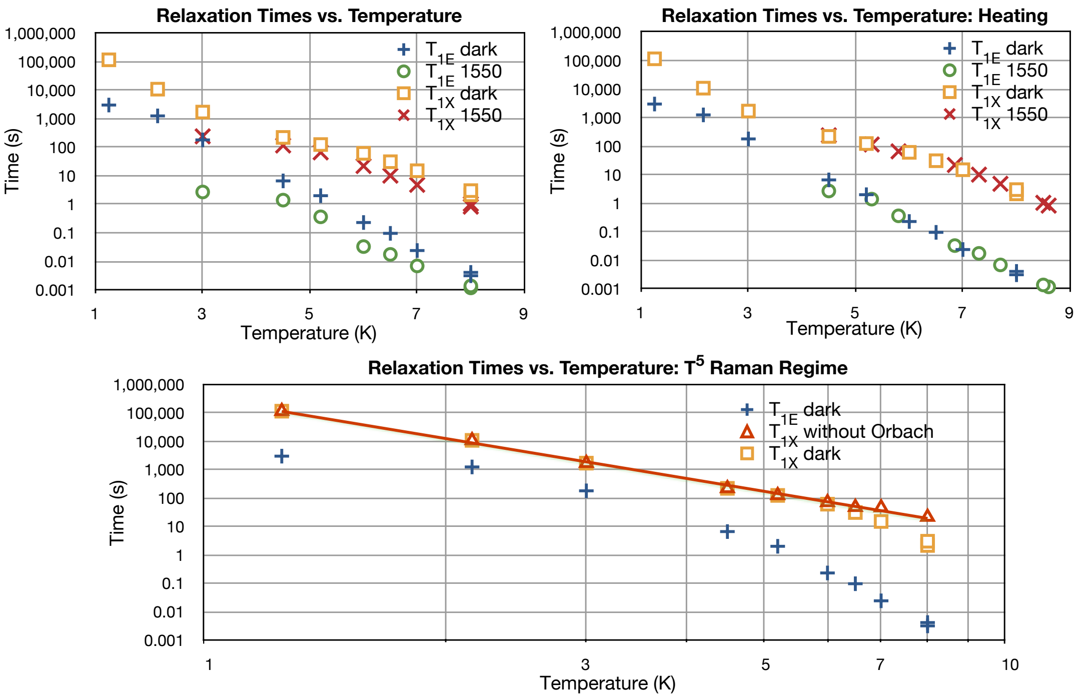

Figure 5.4: **Spin relaxation times in the dark and under ionising illumination in ^{28}Si:P.** Left: unprocessed measurements of T_{1X} and T_{1E} at 9.5 GHz and various temperatures either in the dark or under ionising illumination are shown in the left panel. The T_{1X} and T_{1E} points at 1.2 K and 2.16K are from the reference [HS60] and [FG59] taken at a frequencies of 9.5 GHz and 9.0 GHz, respectively. All other points were taken over two experimental runs where each run used a fixed illumination power, and these two incident powers were calibrated at 8 K as shown. Right: the same data with the ionised measurements corrected for heating according to the measured value of T_{1X} through a linear interpolation/extrapolation of the two closest dark T_{1X} data points. These corrections, which range from 0.5 K to 0.8 K, account for all the illuminated data points apart from the point taken at 3 K. Bottom: the T^5 dependence of T_{1X} is observed in the Raman regime (below 6K). A fit of direct, Raman and Orbach contributions to T_{1E} reveals that in the Orbach regime, $T_{1X} \approx 700 T_{1E}$, and by removing the T_{1X} Orbach term one observes the T^5 dependence over the full temperature range.

The second piece of evidence involves the dynamics of the faster $(T_{1E})_{1550}$ when the light is turned off — the measured T_{1E} time does not return to the dark value immediately and instead a recovery time exceeding seconds is observable. Because the lifetime of conduction electrons is on the order of at most a few μs [LH61], this indicates that the dominant effect of 1550 nm light on ^{28}Si:P in the Orbach regime is one of heating. To test this, a data point was repeated where the cooling power of the cryostat bath was near its maximum and near its minimum, where the bath heater was corrected to match the value of $(T_{1E})_{\mathrm{dark}}$. When the cooling power was high, a reduction of 2.2 was recorded for both T_{1E} and T_{1X}, whereas a low cooling power resulted in a reduction of 4.7 and 4.5, respectively. This indicates that the relaxation enhancement can be adjusted as a function of the cooling power of the bath.

If one assumes that the primary relaxation contribution of ionising light is due to heating, then one should recover the dark T_{1E} and T_{1X} curves if one corrects for the effects of heating. As a simple approximation, the lattice temperatures for the points taken under illumination can be corrected by matching the measured value of T_{1X} under illumination through a linear interpolation/extrapolation of the two closest dark T_{1X} data points, and then applying this same calculated correction to T_{1E}. This adjustment indeed recovers the dark T_{1E} and T_{1X} trend in the Raman and Orbach regimes, as shown in Figure 5.4. Interestingly, the single point in the direct regime is the only one to report a higher $(T_{1X}/T_{1E})_{1550}$ ratio than expected at its 'corrected' temperature ($\approx$ 82), and it agrees with the ratio on the cusp of the direct and Raman regimes ($\approx$ 88). More investigation at these low temperatures is required to see if this ratio remains constant throughout the entire direct regime and if T_{1X} scales according to $T^{1/2}$. If so, it would support the hypothesis that the donors are relaxing due to the ionisation process in this regime and not simply due to heating the lattice.

Although T_{1X} has not been independently measured under ionising illumination, T_{1E} has been measured under a constant level of incident 2000 nm light at temperatures between 1.2 K and 4.2 K by Levitt and Konig [LH61]. T_{1E} was shown to be constant in this region for dilute phosphorus concentrations in natural silicon, on the order of 10 seconds. Although this value cannot be directly compared with present results due to the unknown difference in incident laser power and known difference in wavelength, it is relatively consistent with the data presented in this work.

T_{1X} has been measured in the dark at very low temperatures for other group V donors in silicon. The observation that the ratio T_{1X}/T_{1E} fits to a T^2 dependence in the Raman regime is not unprecedented for group V donors. The ratio of T_{1X}/T_{1E} has been studied for arsenic donors in silicon over a temperature range of 2.2 K – 5 K (within the electronic Raman regime for arsenic) and experiments have also shown a T^2 scaling [CJ63], although this relationship has not been explained. Correcting for the effects of an Orbach mechanism scaled by 700, this $T_{1X} \propto T^{-5}$ trend extends slightly into the Orbach regime, and down in temperature well into the electronic direct regime (below 2.5 K). At the lowest temperatures (1.25 K), studies have shown [HS60] that there is no predicted B^2 magnetic field dependence at this temperature from 5 mT to 1 T, indicating that a modified Raman process is responsible for this regime, rather than a direct process.

Although more study is required to conclude which processes are driving nuclear relaxation in the Raman and Orbach regimes, the evidence suggests that it is not directly due to the time-varying electronic spin state. It remains possible that the time-varying electronic orbital state contributes to nuclear relaxation in the Orbach regime, but this has not been confirmed or denied by ionisation studies due to the effects of heating. While these studies continue it is nevertheless useful to make use of the reduced relaxation times to quickly prepare the electron-nucleus system into a known initial thermal state.

Moreover, if we turn to a regime of high electronic polarisation, say at 95 GHz (3.5 T), illumination can be used to additionally obtain a *hyperpolarised* state: a state whose spin entropy is dramatically reduced compared to that of the thermal state. In the context of ensemble quantum computing, the purity of the initial state is often the principle corrupting contribution to the result of a quantum algorithm. Identifying and understanding hyperpolarisation schemes for donors in silicon is therefore of fundamental computational interest.

5.2 Hyperpolarisation in silicon

5.2.1 Indirect hyperpolarisation in ^{28}Si:P

There are a number of known methods for hyperpolarising donors in silicon using indirect processes, and nearly all attempts to explain these methods exploit the asymmetry in cross relaxation strengths. The resulting nuclear polarisation can be positive (preferring the $M_I = +I$ state) or negative ($M_I = -I$). These methods often fall under the broader category of *dynamic nuclear polarisation* (DNP), wherein the polarisation of the electron is transferred to the nucleus. Many of the following DNP demonstrations in ^{28}Si:P, whose results are summarised in Figure 5.5, have therefore been performed in a regime of high electronic polarisation: either at low temperatures, high magnetic fields or both.

Dynamic nuclear polarisation was first identified by Overhauser in 1953 [Ove53]. Overhauser's insight into spin dynamics was the observation that T_{1X} processes distribute populations according to a Boltzmann spin temperature across the T_{1X} transitions regardless of the electronic polarisation across the T_{1E} transitions. Notably, if the electronic spin temperature was kept artificially high by saturating all electronic transitions, the electronic populations would be evenly mixed and yet the T_{1X} process would distribute populations across T_{1X} transitions according to the expected spin temperature: that of the electron. The result of this effect is positive nuclear hyperpolarisation. The relaxation time T_{1X} determines the length of time required for the nucleus to acquire its maximum polarisation under this method, which can be as large as the polarisation of an electron in the limit that $T_{1X} << T_{1N}$. Nuclear-only T_{1N} processes reduce the maximum achievable steady-state nuclear polarisation by redistributing nuclear populations evenly, and so a measurement of this steady-state amplitude places a lower bound on the ratio T_{1N}/T_{1X} (See Appendix A). This *Overhauser DNP* was used to measure T_{1X} before the use of tidy pulses [FG59], and although slow, it does not require a high degree of electronic polarisation to be observed.

More generally, any method able to maintain a spin temperature difference between T_{1X} and T_{1E} transitions can in principle generate a form of Overhauser DNP. A possible method of maintaining this difference is by applying a DC electric field across the sample. The resulting distribution of carriers can be described by an effective temperature, and the term *hot electrons* is used to describe carriers with kinetic energies much greater than would be expected given the temperature of the phonons in the lattice. Carriers also have a spin temperature which does not necessarily equal their kinetic temperature, but is approximately equal to the electronic spin temperature of the donors. It has been

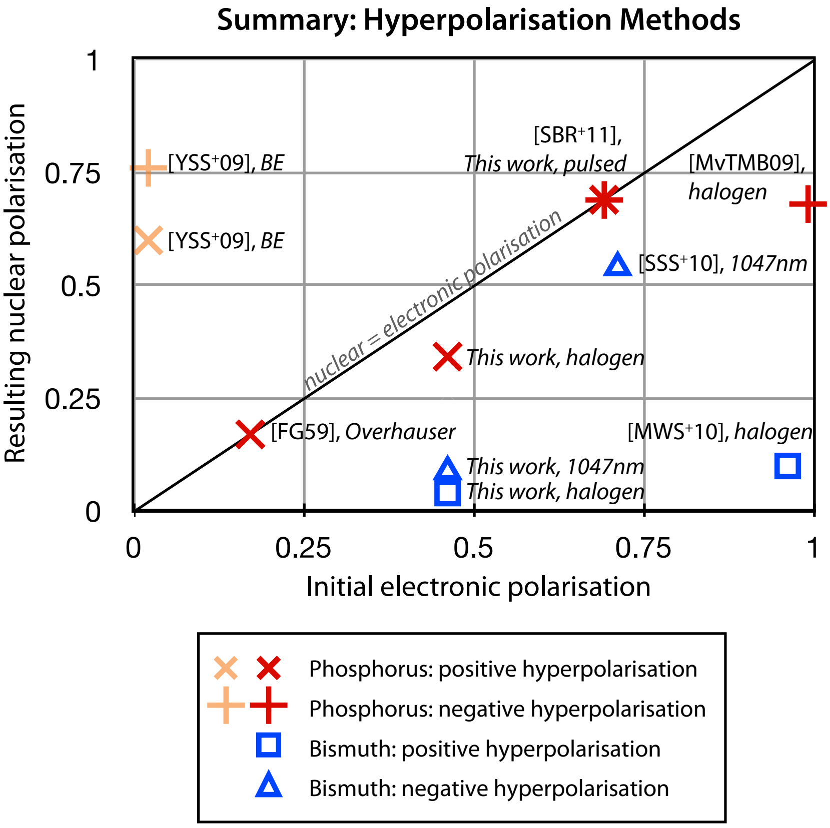

Figure 5.5: **Nuclear polarisation records for phosphorus and bismuth donors starting from various initial electron polarisations.** A variety of techniques exist which are able to hyperpolarise the nuclear spin. The DNP methods partially transfer the electrons' polarisation to the nuclei (shown in red for phoshorus, blue for bismuth). The upper bound for this class of processes, indicated on the graph, is where the nuclei attain the intial polarisation of the electrons. An alternative method which drives spin-dependent bound exciton transitions (shown in orange for phosphorus), relies upon selective ionisation and relaxation rates to attain a high degree of nuclear polarisation; this process is independent of the electrons' intial polarisation and is included for completeness to compare with DNP techniques.

proposed [Feh59] that the excess kinetic energy of the carriers can be donated to donors by driving transitions which conserve angular momentum such as T_{1X}, leading to a heightened steady-state spin temperature relative to T_{1E}. This proposal was tested experimentally, and although the spin and kinetic temperatures of the conduction electrons differed by two orders of magnitude, hyperpolarisation was not observed [Feh59]. One explanation for this is that the generated carriers were too few in number ($\approx 10^8 - -10^{10}$ cm^{-2}) to be effective against a far greater number of donors ($\approx 10^{16}$ cm^{-2}). A complete predictive model relating the T_{1X} spin temperature to the density and kinetic temperature of the hot carriers, which would support this argument, has yet to be published.

A significantly faster optical hyperpolarisation process makes use of the very narrow optical linewidths of ^{28}Si:P to achieve eigenstate-selective excitation of the donor ground state into a *bound exciton* (BE) state [YSS+09]. A BE state is not an orbital state but rather the combination of the donor with a *free exciton* (FE): a conduction band electron coupled to a valence band hole. The two electrons of the BE form a spin singlet, removing the electrons' paramagnetic contribution to the BE energy levels. Instead, it is the spin-$\frac{3}{2}$ hole which splits the energy levels of the BE. These levels can be inferred by scanning the frequency of a laser across the available bound exciton transitions. By analysing this absorption profile, one can determine the frequency that selects a particular donor ground state and excites it into a desired BE hole state, subject to selection rules ($\Delta m_S = \pm 1$). The bound exciton is generally short-lived; one of the two electrons quickly recombine with the hole and the other electron is excited into the conduction band. After the ionised donor recaptures a spin-up or spin-down electron the cycle is complete. This cycle effectively removes electrons from systems with a given spin orientation and substitutes an electron spin with a random spin state. After a short time this builds up a positive or negative nuclear polarisation as T_{1X} redistributes populations according to the eigenstate being ionised. Nuclear polarisations of up to 76% have been observed after 1 second of illumination at low fields (0.043 T) and low temperatures (1.4 K).

Similar optically-induced negative nuclear hyperpolarisation up to -68% has been observed using broadband halogen light [MvTMB09] in natural silicon, starting from a state of high electronic polarisation (8.5 T and 1.4 K – 3 K). White halogen light is made up of many frequencies and so generates carriers with a range of energies in the conduction band, in addition to ionised donors, ionised acceptors and free excitons. A proposal [MvTMB09] for understanding the negative nuclear hyperpolarisation generated by halogen light invokes a temperature difference between the spin temperature of the conduction electrons and that of the lattice phonons. It was supposed that the lattice phonons, which drive

T_{1X} and $(T_{1E})_{\text{dark}}$ processes, have a constant temperature (fit to 2.7 K) over the bath temperature range of interest for a fixed illumination strength, and that the conduction electrons have a relatively colder spin temperature which matches the spin temperature of $(T_{1E})_{\text{light}}$ as well as the bath temperature[1].

This model is inconsistent with halogen light-induced positive hyperpolarisation of phosphorus donors observed at 3.5 T and 4.5 K. As with the 8.5 T data, an overall reduction of amplitude is observed, indicating some combination of an elevated electron spin temperature and a steady-state ionised proportion of donors, the former being the more plausible effect under halogen illumination. If one assumes that the spectrum of the two halogen sources are similar and that the effects are unrelated to the isotopic impurities of natural silicon or electrical contacts used for the experiments at 8.5 T, one can compare the salient features of these two experiments. For the two-temperature model to match the opposing directions of hyperpolarisation at 8.5 T and 3.5 T, the conduction electrons would necessarily have a relatively warmer or colder spin temperature compared to the phonon temperature depending upon the magnetic field, and the origin of this cannot easily be accounted for.

The positive hyperpolarisation can be understood on its own in the context of an Overhauser effect. The visibly higher spin temperature across T_{1E} transitions, as measured by the reduction in total integrated signal, need not apply to T_{1X} transitions which can generate a positive hyperpolarisation as Overhauser predicted. The reduction in total integrated signal could account for, and even predict the amount of, nuclear hyperpolarisation. From Equation A.1.12, a heightened spin temperature with a reduced integrated spectrum intensity R normalised relative to the thermal state (in this example, 0.46) and a thermal electron polarisation of $\mathcal{P}$ (in this example, 0.48%) generates a positive nuclear Overhauser polarisation of $\frac{R-1}{R-(1/\mathcal{P})} = 33\%$, which agrees with the experimental results shown in Figure 5.9, however a complete model requires a mechanism to explain and predict the heightened spin temperature across T_{1E} transitions as a function of field

---

[1] it is unclear why the temperature of the bath does not match the temperature of the lattice but rather does match the spin temperature of the conduction electrons, and it is also unclear how the conduction electrons could ever be colder than the phonons in the lattice.

and temperature. Moreover such a model would need to explain the hyperpolarisation reversal at 8.5 T if it cannot be accounted for by variables such as the spectrum of the halogen source or biased electrical contacts on the sample. To test this hypothesis, and learn more about the dynamics of halogen light-induced hyperpolarisation, one can consider the effects of halogen light on other donors such as bismuth. The effects of halogen illumination upon phosphorus and bismuth donors are presented in Section 5.2.3.

5.2.2 PULSED HYPERPOLARISATION

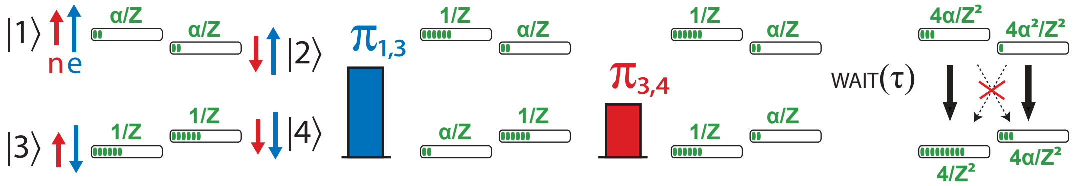

Figure 5.6: **Pulsed hyperpolarisation in ^{28}Si:P.** A two-pulse sequence can transfer the electronic polarisation to the nucleus. After a waiting time greater than a few T_{1E}, the electron regains its own polarisation to arrive at a hyperpolarised state. Cross relaxation would only serve to limit the polarisation of the nucleus and so it is advantageous to use a sample such as ^{28}Si:P which has relatively weak cross relaxation compared to its electronic relaxation. Both positive and negative nuclear polarisation is possible in this manner: by changing the second selective pulse to the $\{1, 2\}$ nuclear subspace, an equal and negative nuclear polarisation is observable.

The above examples of nuclear hyperpolarisation in ^{28}Si:P each make use of nonequilibrium rates generated by the continuous application of microwaves, light, or electric fields. It has been known for a long time [Feh56] that pulsed methods including the Davies ENDOR sequence are able to transfer the polarisation of an electron to a coupled nucleus[2]. It is possible to exploit the relative absence of cross relaxation to polarise both the electron and nuclear spin in a single shot and with high efficiency [SBR$^+$11]. Pulsed hyperpolarisation of the nuclear spin, as illustrated in Figure 5.6, can be understood

---

[2] A related hyperpolarisation method under the name *PONSEE* [MvTA$^+$07] makes use of a selective electronic pulse in addition to continuous radio-frequency waves resonant with a selective nuclear transition to obtain comparable results.

as a polarisation transfer from the thermally polarised electron spin with an ENDOR sequence, followed by a delay wait(τ) which is substantially longer than the electron spin relaxation time. During this delay the electron spin relaxes back to thermal equilibrium [FG59, MvTMB10]. On this timescale, other relaxation processes such as pure nuclear spin flips, or electron-nuclear T_{1X} flip-flops are orders of magnitude slower and can be neglected. A distinguishing feature of pulsed techniques is that they do not depend upon the T_{1X} process (which often become weaker with increasing magnetic field): pulsed hyperpolarisation is in fact more effective when applied to systems with relatively weak cross relaxation, as is the case for ^{28}Si:P.

In the ^{28}Si:P spin basis introduced in Section 3.6, the implementation of the hyperpolarisation sequence upon the first-order Boltzmann thermal state is given by:

$$\begin{aligned} \rho =& \frac{e^{-\hbar\omega_e S_z/k_B T}}{\mathcal{Z}} && (5.2.1)\\ =& \frac{1}{\mathcal{Z}}\left(\alpha|1\rangle\langle 1| + \alpha|2\rangle\langle 2| + |3\rangle\langle 3| + |4\rangle\langle 4|\right) && (5.2.2)\\ \pi_0^{1,3} \to \rho =& \frac{1}{\mathcal{Z}}(|1\rangle\langle 1| + \alpha|2\rangle\langle 2| + \alpha|3\rangle\langle 3| + |4\rangle\langle 4|) && (5.2.3)\\ \pi_0^{3,4} \to \rho =& \frac{1}{\mathcal{Z}}(|1\rangle\langle 1| + \alpha|2\rangle\langle 2| + |3\rangle\langle 3| + \alpha|4\rangle\langle 4|) && (5.2.4)\\ \tau_{\text{WAIT}} \to \rho =& \frac{4}{\mathcal{Z}^2}(\alpha|1\rangle\langle 1| + \alpha^2|2\rangle\langle 2| + |3\rangle\langle 3| + \alpha|4\rangle\langle 4|) && (5.2.5) \end{aligned}$$

where $\alpha = e^{-\hbar\omega_e/k_B T}$ and $\mathcal{Z} = 2(1+\alpha)$, T is temperature in Kelvin and ω_e the resonant frequency of the electron spin.

A useful way to characterise the performance of a hyperpolarisation sequence is to calculate how it affects the spin entropy of the system. Recall from Section 2.3.2 that the linear entropy is given by

$$S_L(\rho) \equiv \frac{\mathcal{N}}{\mathcal{N}-1}(1 - \text{trace}[\rho^2]) \tag{5.2.6}$$

and so the linear entropies of the thermal and hyperpolarised states are given by

$$S_L(\rho_{\text{thermal}}) = \frac{2(1+4\alpha+\alpha^2)}{3(1+\alpha)^2} \tag{5.2.7}$$

$$S_L(\rho_{\text{hyperpol}}) = \frac{16\alpha(1+\alpha+\alpha^2)}{3(1+\alpha)^4} \tag{5.2.8}$$

which is shown in Figure 5.7. The spin entropy calculated in Equation 5.2.8 is minimal with respect to the available relaxation processes within 1s:A. In the limit of $\alpha \to 0$, this sequence generates a pure initial state. It is an optimal example of ‘open-system algorithmic cooling’ [SMW05], which is a class of pulse sequences able to temporarily enhance a state’s purity beyond that of its thermal state.

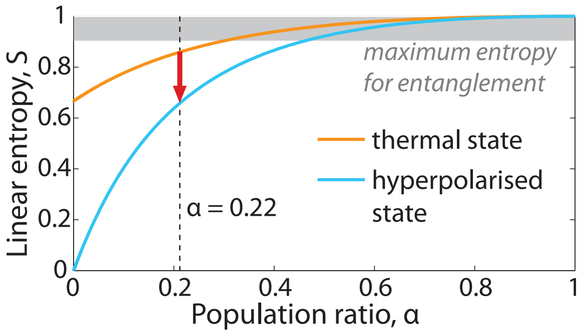

Figure 5.7: **Linear spin entropy reduction due to pulsed hyperpolarisation.** As calculated in Equation 5.2.8, the linear spin entropy of a state able to support pulsed hyperpolarisation can be optimally reduced. This implies that no initial nuclear polarisation is required for an arbitrarily pure intial state generated under this scheme. Hyperpolarisation can nearly double the state’s purity at low temperatures, and optimally reduce the spin temperature at higher temperatures, as indicated by the red arrow (corresponding to the lowest α obtained in the data collected for this thesis). For reference, entangled quantum states only exist in a regime of low spin entropy as indicated by the grey text.

In regimes where $T_{1E} << T_{1X}$, such as the Orbach regime at 9.5 GHz, this sequence allows for the choice of positive or negative nuclear polarisation equal to the thermal electronic polarisation, and is limited only by pulse imperfections. In other regimes, such as the direct regime at 9.5 GHz, the ratio of T_{1X}/T_{1E} is as low as 10 which limits the quality of hyperpolarisation. One way to improve upon this would be to selectively apply ionising light during the delay. As shown in Section 5.1.3, ionising light reduces T_{1E} and correspondingly the overall time required to generate a hyperpolarised state as well, which can be tuned by adjusting the incident laser power. More importantly, under ionising light in this regime the ratio of T_{1X}/T_{1E} is larger by an order of magnitude, which also improves the final quality of the hyperpolarised state.

5.2.3 Optically-driven Si:^{209}Bi hyperpolarisation

Although phosphorus dopants ($I = 1/2, \mathcal{A} = 117.53$ MHz) in silicon have been studied extensively in the context of quantum information, it is only recently that alternative dopants in silicon such as bismuth ($I = 9/2, \mathcal{A} = 1.4754$ GHz) have attracted the attentions of the spin qubit community[3] [SSS$^+$10] .

Bismuth dopants are computationally attractive for three principle reasons. First, the ten nuclear sublevels of bismuth can be used to encode three *logical* qubits: virtual qubits able to perform equivalently under all operations except selective projective readout. Three virtual nuclear qubits in addition to an electron qubit can be used to perform error detection [NC00] or entanglement purification [Cam07]. Secondly, the binding energy of bismuth is larger than that of phosphorus, and given a fixed donor concentration this corresponds to a smaller wavefunction overlap with nearby donors. At comparable fields and temperatures in natural silicon, this smaller overlap accounts for a 30% longer T_{2E} lifetime compared to phosphorus donors [GWR$^+$10]. Lastly, the large hyperfine constant can be advantageous: it potentially allows for sub-nanosecond selective electron spin manipulation at the expensive of larger admixtures (and hence faster T_{1X} relaxation), and these admixtures can play a role in efficient indirect dynamic nuclear polarisation.

Halogen light-induced DNP is observable in Si:^{209}Bi at 8.5 T [MWS$^+$10]. At 3 K the electronic polarisation amounts to over 95%, and the application of halogen light results in a strong nuclear positive polarisation. The spin-echo amplitudes corresponding to different electron transitions across the spectrum display a geometric increase corresponding to a polarisation increase of approximately 10% between neighbouring transitions. The important difference between this and the halogen hyperpolarisation of phosphorus donors at similar fields and temperatures is the direction of polarisation. In contrast, halogen measurements were performed at 3.5 T and 4.5 K (yielding an electron polarisation of 48%), are shown in Figure 5.9. These measurements confirm the direction of hyperpolarisation with a similar polarisation of 4% between neighbouring transitions, which is

---

[3] Other group V dopants, such as arsenic ($I = 3/2$) and antimony (^{121}Sb has $I = 5/2$ and 57% abundance,^{123}Sb has $I = 7/2$ and 43% abundance) are also possible candidate spin qubits, however arsenic suffers from the complicated spin dynamics associated with the fact that $T_{1E} > T_{1X}$ at standard fields (0.3T to 0.8T) and low temperatures [CP58].

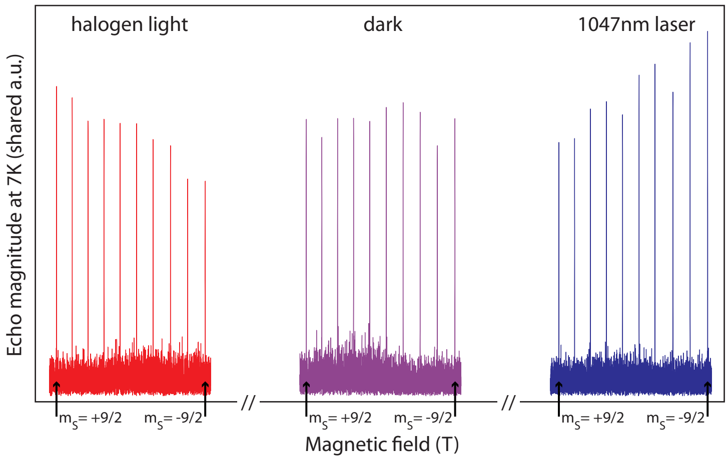

Figure 5.8: **Bismuth donors in silicon under illumination.** At 3.5 T and 7 K, corresponding to an electronic polarisation of 32%, a small positive and negative hyperpolarisation can be observed with the application of either halogen or 1047nm illumination, respectively. A change in the overall integrated intensity, corresponding to a change in electronic polarisation, is also observable at this temperature.

consistent with $\frac{R-1}{R-(1/\mathcal{P})} = 4\%$ for an estimated 5% reduction in integrated signal intensity compared to a dark scan. Phosphorus donors exhibit a different direction of halogen light-induced hyperpolarisation between 3.5 T and 8.5 T whereas bismuth donors do not. It is possible this reversal depends upon the relative strength of the hyperfine and nuclear Zeeman energies. Phosphorus donors at 8.5 T have a nuclear Zeeman energy which exceeds its hyperfine energy; this relation is reversed at fields below 6.7 T. Bismuth donors' nuclear Zeeman energy does not exceed its hyperfine energy until 106 T.

Ionising laser light also generates positive hyperpolarisation at 3.5 T, albeit with a lower overall amplitude. It is unclear which other wavelengths in halogen light contribute to positive hyperpolarisation, which is a subject of future study. Critical wavelengths, such as near-bandgap radiation (1047 nm) decidedly do not contribute to the positive hyperpolarisation of bismuth donors; indeed this wavelength has quite an opposite effect.

When the light is tuned to 1047 nm, the direction of hyperpolarisation changes. At intermediate fields (2 T) and low temperatures (1.5 K) an estimated negative hyperpolarisation of 54% between neighbouring transitions is observable through optical absorption spectroscopy [SSS$^+$10]. Experiments at 3.5 T and 4.5 K, which have a smaller electron polarisation of 46%, also confirm this direction of hyperpolarisation with a -8(1)% polarisation increase between neighbouring transitions. It should be noted that this effect was not conclusively saturated with the available range of optical power. The onset of this hyperpolarisation is fast: on the order of a few seconds for 3.5 T, and even faster at 2 T.

It has been proposed that this negative hyperpolarisation is due to the way that the donor electrons and free exciton electrons form the singlets present in bound exciton states: a second-order relaxation or recombination process involving the donor flip-flop process takes place because first-order processes requiring electrons to be of opposite spin are unlikely in a regime of high electronic polarisation. To conserve angular momentum, a nucleus is simultaneously 'flipped' in tandem with an electron 'flop', this preferentially aligns bismuth nuclei into the $m_I = -\frac{9}{2}$ state. A similar degree of polarisation is observed with phosphorus nuclei, where attempts were made to replicate the temperature and amount of incident irradiation.

The dependence of this process on electron polarisation can be tested by occasionally flipping the spin state of the electron directly and observing the resulting dynamics. By inverting the electron qubit frequently (but less frequently than T_{1E}), the likelihood of a singlet recombination process increases which should over time reduce the steady-state nuclear polarisation. Indeed the very act of measurement with a spin echo affects the likelihood of a singlet recombination by leaving the ensemble in a completely mixed state. By simply varying the shot repetition time one observes a change in nuclear polarisation. This is not due to electronic saturation — in each instance the minimum repetition time exceeds $5(T_{1E})_{\text{light}}$ — however the donors whose electrons are captured as bound excitons and then left ionised require time to neutralise and again contribute to the paramagnetic signal. This can be most clearly observed by varying the shot repetition time of an inversion-recovery T_{1E} measurement, as shown in Figure 5.10.

The degree of 1047 nm-induced hyperpolarisation is reduced with fast shot repetition times, which is consistent with a long-lived ionisation stage of the BE hyperpolarisation process. This gives insight into the spin dynamics of the system however it also highlights the need to distinguish between various, possibly competing, optical and microwave effects.

If the measurements are taken with continuous-wave microwave experiments the microwaves' influence on the optically-induced nuclear polarisation through electronic saturation is unavoidable. If pulsed measurements are taken one can return the electron to its initial state to remove the effects of the microwave pulses on the time-averaged spin state. Indeed this was used for all the indirect hyperpolarisation data presented in this Chapter. A spin-echo sequence which immediately returns the electron to the initial state more closely matches the optical measurements where no microwaves are applied at all, however a key difference between a magnetic resonance spin-echo measurement followed by tidy pulses and optical measurement remains: in the former the field is changed to bring each of the transitions into resonance, whereas the field is fixed in the latter. This implies that the spin temperature of the conduction band could depend upon the transition under observation, and all the halogen hyperpolarisation experiments to date have been under these conditions.

Further study of these systems are required to understand the hyperpolarisation dynamics of donors in silicon, for they provide a simple and efficient tool for state initialisation with only a moderate amount of electronic polarisation. There are two future experiments that would help discriminate between different polarisation mechanisms. The first is halogen illumation with a constant background magnetic field afforded by optical readout. To avoid corrupting the optical detection with the broadband excitation, appropriate filters upon the halogen should be used. This has the advantage of potentially identifying the frequencies responsible for halogen hyperpolarisation, and to observe their effects above and below 6.7 T. The second experiment is 1047 nm-induced hyperpolarisation at 8.5 T for phosphorus donors: it is presently unknown if the direction of hyperpolarisation changes in a regime where the nuclear Zeeman dominates the hyperfine coupling. These two initiatives are important to improve the processing power of donor qubits in silicon: if armed with a detailed, predictive model of these dynamics, an optimal point in parameter space can be chosen to quickly initialise qubits into a state of minimal spin entropy.

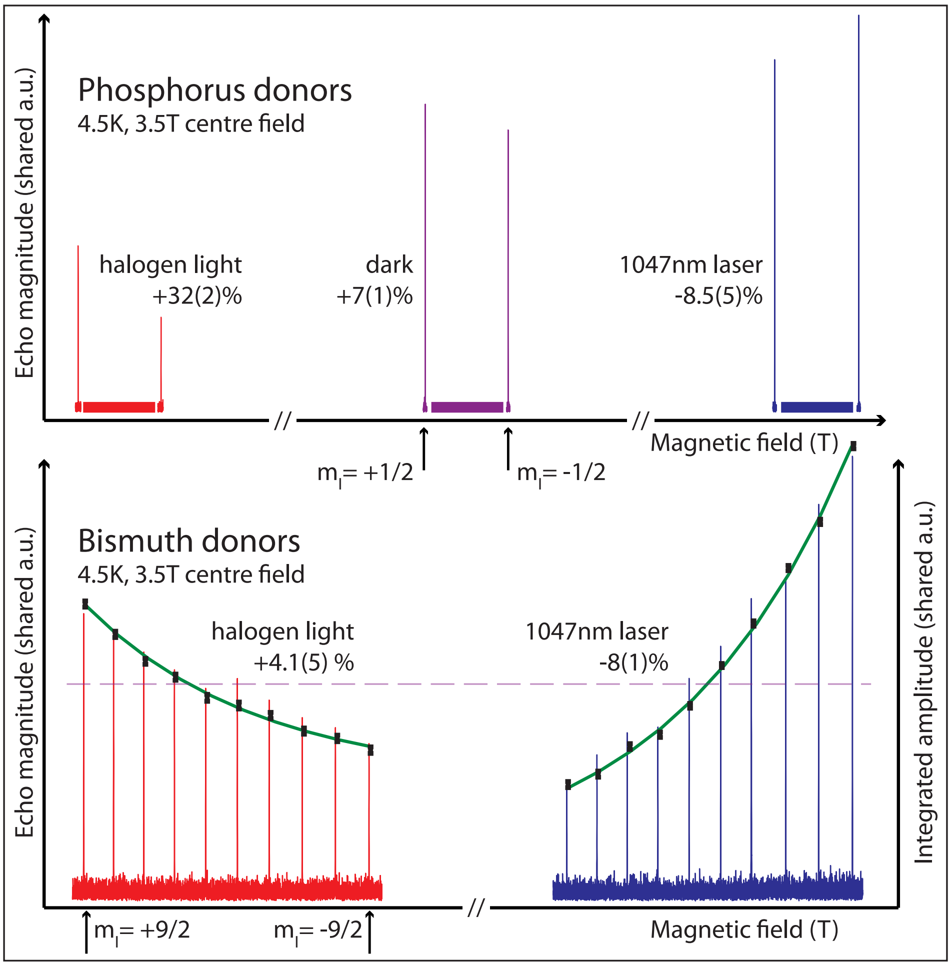

Figure 5.9: **Phosphorus and bismuth optically-induced hyperpolarisation.** At 3.5 T and 4.5 K, bismuth and phosphorus donors were subjected to similar halogen and 1047 nm light intensities and an echo-detected field sweep was collected. In both instances, halogen light induces a positive nuclear hyperpolarisation and 1047 nm light induces a negative nuclear hyperpolarisation. Precise polarisations were determined by integrating over the entire line of interest and calculating the errors and line-over-line polarisation either directly or with a geometric fit as shown. The noise intensities for phosphorus donors are represented by solid bars as a visual aid. Halogen light was roughly nine times more effective with phosphorus, whereas 1047nm light showed no discernable difference between phosphorus and bismuth. A change in overall intensity, corresponding to a change in electronic polarisation, is observed in comparison to the dark value (for bismuth, the dashed line estimate is taken from the $m_I = -\frac{9}{2}$ and $m_I = +\frac{9}{2}$ electron transition spin-echo amplitude). The polarisation of the dark phosphorus scan is not presently understood, although a smaller positive polarisation (2(1)%) has been observed at 8 K.

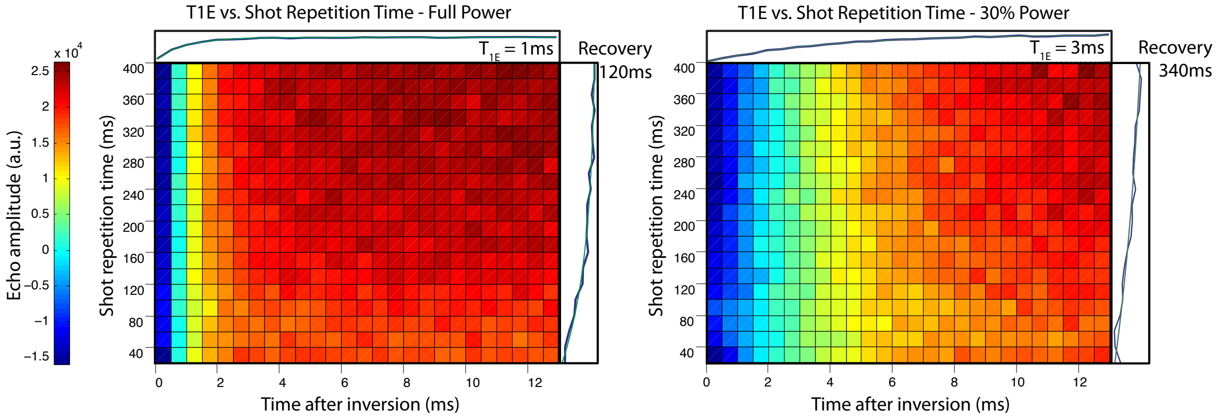

Figure 5.10: **Bismuth donors' $(T_{1E})_{\textbf{light}}$ on the $m_I = +\frac{9}{2}$ transition as a function of shot repetition times for two different incident laser powers.** By reducing the laser power roughly by a factor of three, the enhanced relaxation rate drops similarly. The total shot repetition time, which is longer than both measured relaxation rates, affects the amplitude of the recovered echo. The recovery rate of these amplitudes can be fit to a common 'infinite time' echo amplitude measured with 10 seconds between shots, and one finds that this rate also drops with the drop in the incident laser power. This is all consistent with a model where some donors relax by exchanging their spin state with carriers, and some donors relax through the capture of bound excitons followed by ionisation. Both such processes would vary with the incident laser power as observed, however effects due to heating have not yet been ruled out.

§ 6. QUANTUM STATE TOMOGRAPHY

The success of a quantum algorithm depends as much on faithful measurement as it does on initialisation and control. Measurements can be made to reconstruct the unique density matrix describing a quantum state; this process is known as quantum state tomography[1]. State tomography varies according to the set of direct experimental observables and the indirect methods used to supply the remaining information. For the purposes of this Chapter I will discuss quantum state tomography using single-transition readout as is common in EPR, although the ideas generalise naturally to broadband readout available in NMR.

Any quantum algorithm able to support exponential speedup encodes its result into a small number of qubits designated for measurement. Quantum algorithms which require full tomography for readout cannot scale favourably due to the exponential number of measurements required to reconstruct the full density matrix. For diagnostic purposes, however, the ability to completely reconstruct a quantum state is invaluable, for it can be used in whole or in part to test any characteristic of the state.

6.1 OBSERVABLE AND UNOBSERVABLE COMPONENTS

The set of direct observables in magnetic resonance are net magnetisation measurements in the plane perpendicular to z, the axis of the background magnetic field. Signal amplitudes measured using magnetic resonance are proportional to population differences, not absolute populations as is the case with alternative measurement techniques including optics [SSY$^+$11] or single electron transistors [MPZ$^+$10]. Therefore a critical challenge

---

[1] Other forms of quantum tomography include *quantum process tomography* whereby one uniquely determines the matrix corresponding to a given control operation, and secondly *quantum measurement tomography* whereby one determines the precise action of measurement upon a system.

for faithful quantum state tomography using ensembles in magnetic resonance is to precisely determine both the observable and the identity ("unobservable") component of the density matrix.

The four entries in the observable component of an arbitrary 2x2 single-qubit density matrix can be easily reconstructed with two population measurements and one coherence measurement of both x and y data. The first population measurement records the population difference between eigenstates $|1\rangle$ and $|2\rangle$, which can be measured with a calibrated spin echo sequence. To normalise this first measurement to a known echo amplitude, the second population measurement records the amplitude of a spin echo sequence applied to a known reference state, such as a thermally populated state. After normalisation, the appropriate addition of a scaled identity matrix ensures the populations sum to one. The coherence described in the entry $|1\rangle\langle 2|$, which is assumed to be forming a coherent echo at the outset of the tomography process, can be inferred by the in-phase and quadrature echo amplitudes following a refocusing π pulse. This also is normalised to the echo amplitude of the thermal state, and because the density matrix is Hermitian both off-diagonal components are uniquely determined. This single-qubit tomography process is straightforward yet not particularly robust against errors such as pulse imperfections or stimulated echoes.

The scaled identity component must be added to the observable density matrix because the state preparation sequence can mix the state relative to the thermal state. Importantly, this 'trace correction' is distinct from the identity component corresponding to the initial polarisation of the thermal state. After reconstructing the trace one observable matrix ρ_{ob} as above, the full density matrix can be constructed by knowing the Hamiltonian of the system and the field and spin temperature at the time of measurement. As a first approximation, Equation 3.0.1 can be incorporated into Equation 3.1.3

to find:

$$\rho_{\text{thermal}} = \frac{1}{\mathcal{Z}} \exp(-\beta g \mu |\vec{B}_0| \sigma_Z / 2) \tag{6.1.1}$$

$$= \frac{1}{\exp(-\beta g\mu|\vec{B}_0|/2) + \exp(\beta g\mu|\vec{B}_0|/2)} \begin{pmatrix} \exp(-\beta g\mu|\vec{B}_0|/2) & 0 \\ 0 & \exp(\beta g\mu|\vec{B}_0|/2) \end{pmatrix} \tag{6.1.2}$$

$$= \frac{1}{1+\alpha} \begin{pmatrix} \alpha & 0 \\ 0 & 1 \end{pmatrix} \quad \text{for } \alpha = \exp(-\beta g\mu|\vec{B}_0|) \tag{6.1.3}$$

$$= \sigma_{\mathbb{I}} \frac{2\alpha}{1+\alpha} + \frac{1-\alpha}{1+\alpha} \begin{pmatrix} 0 & 0 \\ 0 & 1 \end{pmatrix} \tag{6.1.4}$$

The first term is the identity component which can be estimated according to the measured values of β, g and $|\vec{B}_0|$. The second term is the observable component of the thermal state, and by replacing this trace-one density matrix with the experimentally reconstructed state ρ_{ob}, one reconstructs the full density matrix.

6.1.1 Spin temperature

Unfortunately estimating the identity component in the above fashion is susceptible to error. Temperature readings and magnetic field measurements may not represent the true lattice environment, and evidence for this can be found in Section 5.1.3 where $(T_{1E})_{\text{dark}}$ was shown to depend upon the cooling power of the bath. Moreover the lattice temperature does not necessarily agree with the spin temperature of the system. An accurate measurement of the identity component is critical to an accurate tomography process, and so if possible it is important to identify ways of revealing the spin temperature using the spins themselves. To estimate the "unobservable" component using spins, one must exploit a nonunitary process able to transform part of the identity component into an observable component for measurement. Chapter 5 discussed many such processes, the most well-understood of these being pulsed hyperpolarisation in ^{28}Si:P.

The effects of pulsed hyperpolarisation applied to well-characterised systems such as ^{28}Si:P can be used to calculate bounds on the spin temperature of the system. It was explained in Section 5.2.2 that the hyperpolarisation sequence is able to reduce the spin temperature of ^{28}Si:P below that of the thermal state; this reduction necessarily comes at the expense of the “unobservable” component as seen by the amount of population common to all four levels in the hyperpolarised state shown in Figure 6.1. Although the ratio between spin-echo amplitudes on the two electronic transitions in the hyperpolarised state is still given by $\alpha : 1$, the echo amplitude, which measures the difference between these two levels, differs. Indeed the spin-echo enhancement of the hyperpolarised state corresponds to $2/(1+\alpha)$, and an accurate measurement of this enhancement reveals the initial electronic spin temperature.

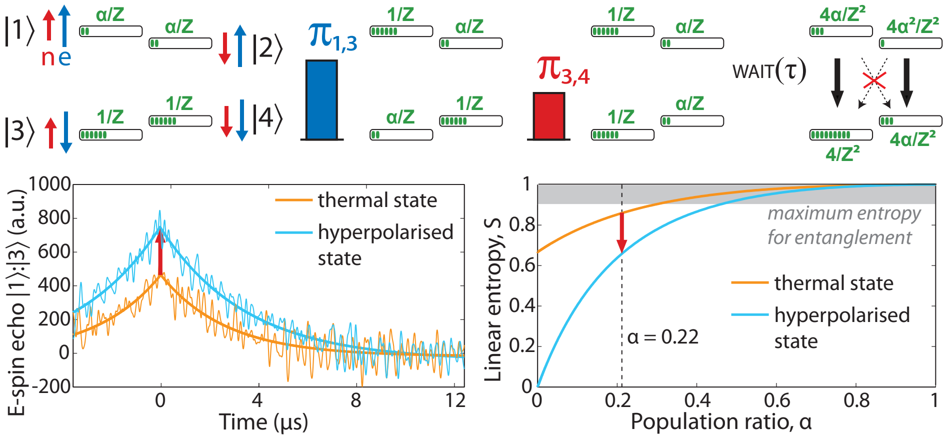

Figure 6.1: **Spin temperature measurement.** The hyperpolarisation sequence serves a dual purpose: it provides a conservative estimate for α through the observable enhancement of the echo amplitude compared to that of the thermal state. This enhancement is given by $2/(1+\alpha)$ and is made possible through the reduction of linear spin entropy below that of the thermal state. The particular enhancement observed here, 1.643(2), corresponds to an upper bound of $\alpha \leq 0.217(2)$, which is consistent with the experimental conditions of 3.56 T and 2.8 K.

The echo amplitude enhancement is a strictly conservative measure of the initial spin temperature: it places a lower bound on the true polarisation of the electron as imperfections such as pulse errors or residual relaxation processes only lead to a lower apparent state purity. Applying this measure to the enhanced echo amplitude shown in Figure 6.1, which was fit to 1.643(2), α has an upper bound $\alpha \leq 0.217(2)$, which corresponds to a polarisation of at least 64%. The estimate of the electronic spin temperature given by magnetic field and temperature measurements (2.8 K and 3.56 T) yields a similar electronic spin polarisation of 67%. On the other nuclear subspace, the electronic transition $\{2, 4\}$ registers a corresponding reduced spin echo, with an intensity of $2\alpha/(1 + \alpha)$ compared to the thermal state. Because effects such as pulse errors are also able to reduce an echo's intensity, the change in this echo amplitude would not be a strictly conservative spin temperature estimate as is the case with the enhanced spin-echo amplitude across the $\{1, 3\}$ transition.

The uncertainties involved with this measurement deserve consideration. Uncertainty arises from the signal to noise ratio of the two echoes and the confidence of the fit used to determine their amplitudes. To improve the signal to noise ratio, one must repeat the measurement many times. In doing so one must wait many T_{1X} to ensure both the electron and the nuclear spins are fully relaxed. To avoid the effects of drifting environmental variables during these long times, measurements of the hyperpolarised echo should be alternated with thermal state spin echo measurements. To extract the amplitude uncertainty of the fits of the resulting echoes, one can perform a fit function for each fixed amplitude value in a designated range and record the χ^2 value of the fit. The uncertainty of the fit corresponds to the 95% confidence interval determined by these χ^2 values. With these error considerations taken into account, the appropriate weighting of the identity component and observable component are known, and all that remains in the tomography process is to reconstruct the observable density matrix.

6.1.2 MEASURING POPULATIONS

Measuring the populations of an arbitrary multi-qubit density matrix is a straightforward extension of the single-qubit example given above. The first measurement is to determine a reference echo amplitude from a known initial state such as the state at thermal equilibrium. This reference measurement allows for all future population-difference measurements to be normalised accordingly. Subsequently, populations of the state under investigation can be measured by applying high-fidelity π pulses to move various populations into an observable: namely, a population difference between two eigenstates with a splitting equal to the measurement resonance frequency (hereafter referred to as the 'measurement transition'). The amplitudes of the resulting echoes form a simple set of linear equations from which absolute populations can be determined. To avoid T_1 and T_2 effects, all measurements are taken at a fixed time from the start of the tomography process and the same spin-echo delay is used in each experiment.

Recording the population differences between every pair of eigenstates yields an overdetermined system of linear equations whose solution can be approximated using a least squares solution. Alternatively, a smaller but complete set of measurements can be taken which minimises the total number of applied pulses, each of which potentially corrupt the accuracy of the tomography process. The resulting populations, using either method, must be corrected to have a trace of one by the appropriate addition of a scaled identity matrix to compensate for signal loss due to mixing. The trace-corrected observable density matrix can have negative populations; this occurs when population has been 'borrowed' from the identity component through a hyperpolarisation sequence. The final density matrix which includes the correct identity component cannot have negative populations.

The standard error of the echo amplitudes due to noise can be carried through the system of linear equations to form an uncertainty for each population density matrix element. In addition, a distinct concern surrounds the errors due to the tomography measurement itself. The corrupting effects of the pulses on the accuracy of the tomography can be estimated by first characterising the errors due to the pulses themselves. Pulse errors in magnetic resonance are due to MW and RF inhomogeneities in the sample space, and are manifested as variations in power (rotation angle) and phase (rotation axis) across the sample. The π pulses used to move populations do not rely upon an accurate rotation axis, however a spread in applied rotation angles can mix the state and reduce the resulting population difference amplitudes. Some populations, such as those belonging to the eigenstates forming the measurement transition, suffer less from these effects than those which have been moved by a longer sequence of π pulses, and so it is important to identify these errors where possible. The Rabi oscillations used to calibrate various π pulses in the system can be fit to determine the standard deviation of rotation angles due to a single π pulse. This information can be used to determine the error involved with each population measurement in the tomography process. Correspondingly, the error in each population density matrix element due to both noise uncertainties and pulse imperfections can be calculated.

6.1.3 Measuring coherences

Coherent superpositions are a more complicated matter because they need to be both moved and refocused into an echo along the observable measurement transition. At the outset of the tomography process all superpositions across the ensemble are assumed to be forming an echo; assuming otherwise implies that the tomography process must be customised to compensate for the dephased state under investigation.

Coherences which are not directly observable can in principle be measured by first projecting them into populations with a $\pi/2$ pulse and then moving them into the measurement transition. Although this avoids having to apply later refocusing pulses, the precise phase of the coherence is not known ahead of time and so the phase of the coherence must be inferred by projecting along two orthogonal axes. The maximum measured amplitude, scaled according to the thermal spin echo, and its corresponding phase are taken to represent the magnitude and phase of the coherence in question. This method relies upon the fidelity of its pulses for its accuracy; imperfections including both rotation angle and rotation axis errors can contribute to overestimates of the coherence's magnitude. In addition, stimulated echoes can contribute to this measurement, and so a more robust detection method is preferable where possible.

Instead of identifying a coherence through its projection onto a population, one can maintain it as a superposition and instead identify it through its exclusive degree of freedom: the phase relationship between two eigenstates. These phases can be manipulated without affecting populations through R^Z rotations. The phase of the coherence can be rotated incrementally per experimental shot, and after mapping it into the measurement transition with appropriate π pulses, the phase of the refocused echo varies accordingly. This allows for a conservative estimate the magnitude of the coherence in question by recording the oscillations of the final echo over time and analysing its frequency components with a complex Fourier transform. The magnitude of the Fourier transform at the assigned frequency corresponds to the magnitude of the coherence under investigation.

Other frequencies, such as zero-frequency baseline shifts from pulse errors and stimulated echoes, and other frequencies from other superpositions, do not contribute to the final coherence estimate. For this to hold true, each coherence must be assigned a distinguishable time-varying frequency.

As discussed in Section 2.2, R^Z rotations are not directly available operations, however composite dynamic or geometric pulses can produce the required effect. Depending upon which implementation is chosen, secondary $(R/2)^Z$ rotations are also applied between the target eigenstates and other eigenstates in the system. This is acceptable provided the net result of the total sequence of R^Z gates assigns a unique frequency to each coherence in the system, which corresponds to a diagonal unitary operator of the form:

$$\begin{pmatrix} e^{i\phi_1} & 0 & 0 & \cdots \\ 0 & e^{i\phi_2} & 0 & \cdots \\ 0 & 0 & e^{i\phi_3} & \cdots \\ \vdots & \vdots & \vdots & \ddots \end{pmatrix} \tag{6.1.5}$$

such that $(\phi_a - \phi_b) \neq (\phi_c - \phi_d)$ for all distinct identifiers $\{a, b, c, d\}$ where $(a, b) \neq (c, d)$. As an example, for a coupled spin-$\frac{1}{2}$ spin-$\frac{1}{2}$ system, this condition can be satisfied with two selective geometric rotations. The operations $\theta^Z_{3,1}$ and $\eta^Z_{3,4}$ combine to form the unitary

$$\begin{pmatrix} e^{-i\theta/2} & 0 & 0 & 0 \\ 0 & 1 & 0 & 0 \\ 0 & 0 & e^{+i\theta/2+i\eta/2} & 0 \\ 0 & 0 & 0 & e^{-i\eta/2} \end{pmatrix} \tag{6.1.6}$$

The value of θ is incremented by $\delta\theta$ on each shot of the experiment, with an effective frequency of $\nu_\theta = 2\pi/\delta\theta$ (and similarly for η, $\delta\eta$ and ν_η). With this unitary the resulting frequencies would include ν_η (for the $|1\rangle\langle 3|$ coherence), $-\nu_\theta - \nu_\eta$ (for $|2\rangle\langle 3|$) and $\nu_\eta - \nu_\theta$ for $|1\rangle\langle 4|$). In this example it is therefore important to choose ν_θ and ν_η such that $\nu_\theta \notin \{\pm\nu_\eta, \pm 2\nu_\eta, \pm\nu_\eta/2\}$ to ensure that the frequencies remain distinguishable. Quadrature measurement of the measured echo allows us to discriminate between the resulting positive and negative frequencies; projective tomography methods do not have this feature.

This example tomography scheme was applied to various single and double coherences in ^{28}Si:P to verify the scheme's ability to accurately measure their magnitudes [SBR+11].

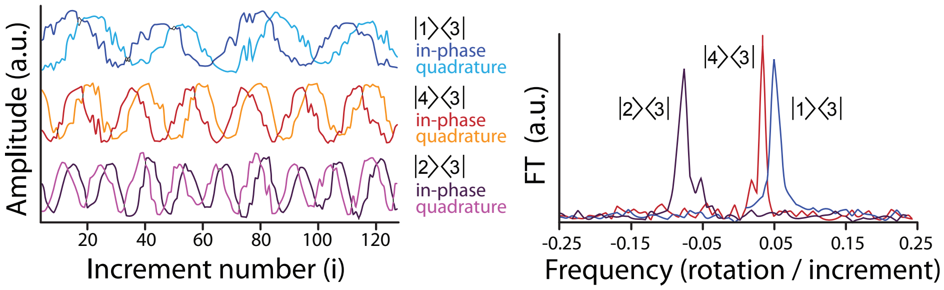

Figure 6.2: **Coherence tomography using R^Z rotations.** The phases given in the operator Equation 6.1.3 can be used to uniquely label each coherence in the system. To test this principle, two R^Z gates are used where the two rotation angles, η and θ are varied by different increments $\delta\eta$ and $\delta\theta$ as the experiment is repeated. Example oscillations are shown for three different coherences. The electron coherence $|1\rangle\langle 3|$, nuclear coherence $|4\rangle\langle 3|$ and double quantum coherence $|2\rangle\langle 3|$ each oscillate with a different frequency as determined by Equation 6.1.3 and the fixed increments $\delta\eta$ and $\delta\theta$. Fourier transforms of the oscillations with respect to increment number show peaks located at 0.050(8), 0.031(5) and -0.079(8), in agreement with the set frequencies $\nu_\theta = 0.05$ and $\nu_\eta = 0.03$.

The results of this can be seen in Figure 6.2. Fourier transforms of the oscillations with respect to increment number show peaks located at 0.050(8), 0.031(5) and -0.079(8), in agreement with the set frequencies $\nu_\theta = 0.05$ and $\nu_\eta = 0.03$. The presence of other Fourier peaks would be illustrative of pulse errors in the mapping sequence, but as seen in Figure 6.2 such errors are negligible.

The uncertainties and errors involved with these coherence measurements mirror the uncertainties and errors for the population measurements. The standard error due to noise in the Fourier-transformed signal must be taken into account while recording the integrated amplitude of the frequency peak of interest. Additionally, pulse errors can reduce the final echo magnitude which can in principle be accounted for. A spread in rotation angles compromises the accuracy of all tomography sequences, and can be corrected for by recording and fitting their Rabi oscillation profiles as above. Secondly, variations in the rotation axis of π pulses impart a range of unwanted phases upon coherences, and variations in the rotation axis of projective $\pi/2$ pulses amount to the projection of a subset of the ensemble. The effects of such errors can act constructively or destructively, leading to a large or negligible reduction in the final spin echo. Accurately correcting for them can be done through a careful diagnosis of the tomography process itself, however in instances where there is a high fidelity match between the target state and the measured density matrix one can consider the effects of such pulse errors negligible.

6.2 Compiling the density matrix

This measurement scheme scales favourably with the number of density matrix elements in the sense that it requires at most N R^Z rotations for N matrix elements, and considerably less if the gates used simultaneously impart R^Z rotations across multiple coherences at once. Once each of the elements have been compiled and combined with the spin temperature-dependent identity component, the resulting density matrix can be analysed and compared to the target density matrix.

There are two conventional measures of state fidelity, $\mathcal{F}(\rho_1, \rho_2) = \left(\mathrm{Tr}\left(\sqrt{\sqrt{\rho_2}\rho_1\sqrt{\rho_2}}\right)\right)^2$ or alternatively the more generous measure $\sqrt{\mathcal{F}(\rho_1, \rho_2)}$. When applied to physically allowed states, both measures are non-negative and reach a maximum value of 1 when $\rho_1 = \rho_2$. For the remainder of this thesis the more conservative measure is used unless otherwise specified.

6.2.1 Error analysis

The errors calculated for each density matrix element can be combined to determine the error on the state fidelity, as well as other state characteristics such as negativity, purity, subsystem projections, discord and more. In place of working through the error propagation of each of these calculations — some of which are non-algebraic — a routine, general Monte-Carlo sampling of matrices within all the error bounds can be used to determine the final errors.

The matrices generated by Monte-Carlo are chosen such that each element in a test density matrix deviates from the measured density matrix element by an amount chosen randomly from a normal distribution whose standard deviation matched that elements' error. After these pseudopure test matrices are generated, a random sampling from the errors involved with the spin temperature measurement and thermal reference echo are

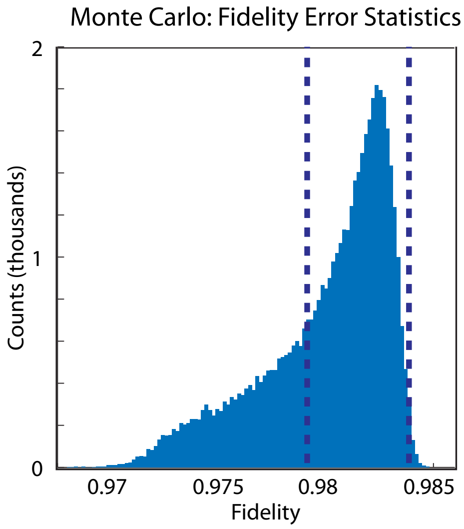

Figure 6.3: **Monte-Carlo error calculations.** When discussing a numerical property of a reconstructed density matrix, for example state fidelity, its error must be calculated from all of the uncertainties in the state, including any temperature measurements and thermal reference measurements. To determine how these uncertainties contribute to uncertainties in the final state fidelity, Monte-Carlo methods can be used to calculate sample matrices within all error ranges as described in the main text. The fidelity of these Monte-Carlo generated matrices with the desired target state can be recorded for a statistically sufficient number of samples. A example collection of such samples is shown above with a blue line indicating the standard deviation. This range can be used to quote the uncertainty of the state fidelity; this example displays a state fidelity of 98.2(2)% with its target state.

included to ensure that all uncertainties are accounted for in the final generated test matrix. These generated states must be physically valid, and so the off-diagonal deviations are chosen such that the state is Hermitian. The resulting states are not trace one in general and so are renormalised and then evaluated for physical validity. Unphysical matrices can be discarded and statistics on the remaining physical matrices can be collected to determine the uncertainty of any particular characteristic of the density matrix, with a sample fidelity error calculation shown in Figure 6.3. Calculating uncertainties in this way tacitly makes the simplifying assumption that the contributing errors are uncorrelated; this method could be refined given the ability to measure a full set of error correlations.

§ 7. ENTANGLEMENT

This chapter concerns the generation of entanglement in two very different spin ensembles. Section 7.1 discusses the generation of entanglement between electron and nuclear spins in ^{28}Si:P. Section 7.2 discusses the generation of pseudo-entanglement between two nuclear spins in a carbon fullerene system using the polarisation of a transient optically excited electron triplet. Quantum state tomography was used in both cases to characterise the degree of resulting entanglement.

7.1 NUCLEAR-ELECTRONIC ENTANGLEMENT USING ^{28}SI:P

Results presented in previous chapters indicate that ^{28}Si:P is an attractive system for the creation of spin ensemble entanglement: at high fields and low temperatures ^{28}Si:P is sufficiently polarised and supports this high-fidelity selective control required for accurate state generation and quantum state tomography. These characteristics are a direct result of the quality of the samples used; these samples are strain-free single crystal samples which have been isotopically enriched.

7.1.1 SAMPLE CHARACTERISTICS

Natural silicon is made up of two spin zero isotopes including ^{28}Si with 92.2% abundance and ^{30}Si with 3.1% abundance, and a spin-$\frac{1}{2}$ isotope ^{29}Si with a 4.7% abundance. The escalating interest in silicon-based devices for quantum computing has been further stimulated by the relatively recent discovery that isotopic enrichment dramatically narrows the linewidths of donors' electronic spin and optical transitions [KSM$^+$03]. The random distribution of spin-active ^{29}Si atoms can couple through a dipolar interaction with the donor qubits to reduce T_{2E}. By removing ^{29}Si as a source of inhomogeneous broadening, the linewidths of donors in silicon are limited only by the bandwidths of the applied pulses. Pulsewidth-limited transitions enhance the fidelity of quantum sequences in two ways: the decoherence due to T_{2E} over a certain pulse sequence duration is minimised, and the pulses themselves are each of a higher fidelity because the spin manipulation is highly uniform due to the well-defined transition frequency.

Nearby ^{29}Si nuclear spins can couple to donors, and in a similar manner the electrons of nearby donors can also couple to one another. In addition to reducing the concentration of ^{29}Si spins one can also reduce the concentration of donor spins to improve the electronic lifetime of the donor ensemble [TLAR03]. In the experiments reported here, the sample consists of a ^{28}Si-enriched single crystal with a residual ^{29}Si concentration of order 70 ppm. Phosphorus doping of $\sim 10^{14}$ cm^{-3} was achieved by adding dilute PH_3 gas during crystal growth; this method is less destructive to the quality of the lattice than other forms of doping such as ion implantation. Further information on the sample growth has been reported elsewhere [BPRA09].

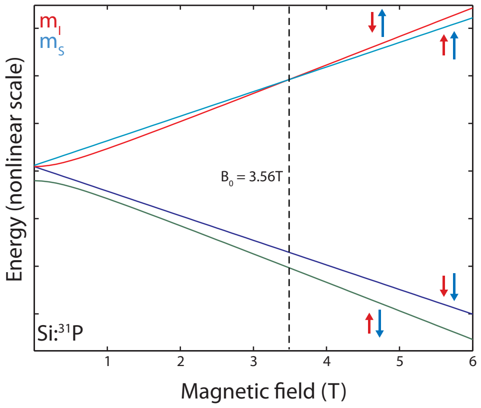

Figure 7.1: **Schematic energy diagram for Si:P.** A nonlinear energy-level diagram of the four eigenstates of ^{28}Si:P reveal the frequencies of the nuclear transitions, and display a zero-crossing at approximately 3.5 T. In this plot the electronic Zeeman interaction is scaled down to show the separate levels more clearly, while maintaining the critical field value at 3.4 T. The Hamiltonian used to generate this plot is $\mathcal{H}_0 = \hbar(\omega_A \sigma_Z \otimes \sigma_I + \omega_B \sigma_I \otimes \sigma_Z + C^{AB}(\vec{\sigma} \cdot \vec{\sigma}))$.

Armed with a high quality sample, the experimental challenge is to perform entangling operations and tomography in a regime of high polarisation. DNP methods can be used to enhance the natural polarisation of the system, however one must first minimise the thermal linear entropy by moving to high magnetic fields and low temperatures. Experiments were performed at 2.8 K using a pumped cyrostat, and at a magnetic field of 3.56 T. An additional experimental difficulty at this field using ^{28}Si:P is the resulting nuclear transition frequencies: the nuclear Zeeman splitting is approximately half of the hyperfine value at 3.56 T and so the one of the two transition frequencies $\omega_N \pm \mathcal{A}/2$ are approximately zero (see Figure 7.1). Unsuccessful efforts were made to drive this low-frequency transition; in all the following experiments only the $m_1 = -1/2$ transition was used to manipulate the state.

7.1.2 Entanglement thresholds

Once in this regime of high polarisation, a spin temperature measurement can be used to identify a maximum value for α, the population ratio between electron $|\uparrow\rangle$ and $|\downarrow\rangle$ states. This value determines which preparation strategies can be used to successfully generate entanglement. As an illustrative example, I compare the thermal polarisation requirements, expressed in terms of α, for generating an entangled quantum state with and without an initial hyperpolarisation sequence.

Entanglement is maximised in a mixed two-qubit density matrix by first minimising the linear entropy, and then generating an entangled coherence across the levels with the greatest and second-smallest population [WNG$^+$03, VAdM01]. The entangling sequence can be applied to the hyperpolarised state as given in Equation 5.2.5, and expressed in its density matrix form in the $\{|1\rangle, |2\rangle, |3\rangle, |4\rangle\}$ basis.

$$\rho_{\text{hyper}} = \frac{4}{\mathcal{Z}^2} \begin{pmatrix} \alpha & 0 & 0 & 0 \\ 0 & \alpha^2 & 0 & 0 \\ 0 & 0 & 1 & 0 \\ 0 & 0 & 0 & \alpha \end{pmatrix} \tag{7.1.1}$$

$$\left(\frac{\pi}{2}\right)^{1,3}_{\pi/2}, \pi_0^{3,4} \rightarrow \rho_{\text{hyper,ent}} = \frac{2}{\mathcal{Z}^2} \begin{pmatrix} 1+\alpha & 0 & 0 & 1-\alpha \\ 0 & 2\alpha^2 & 0 & 0 \\ 0 & 0 & 2\alpha & 0 \\ 1-\alpha & 0 & 0 & 1+\alpha \end{pmatrix} \tag{7.1.2}$$

The partial transpose of this matrix has a zero crossing when

$$\alpha^3 - (1-\alpha)^2/4 = 0 \tag{7.1.3}$$

or when $\alpha \approx 0.432$.

It is worth briefly considering the crossing-points for other preparation strategies, in each case using the optimal entangling sequence described above. A common preparation strategy in NMR chooses to mix the state in such a way that the state can be written as a sum of a perfectly mixed and perfectly pure state; this is called the *pseudopure* preparation scheme. Three examples include i) the pseudopure preparation scheme applied to the thermal state ii) the thermal state with no preparation and iii) the pseudopure preparation scheme applied to the hyperpolarised state. For i), the prepared pseudopure state has the form

$$\rho_{\mathrm{pp}} = \frac{1}{\mathcal{Z}} \begin{pmatrix} (1+2\alpha)/3 & 0 & 0 & 0 \\ 0 & (1+2\alpha)/3 & 0 & 0 \\ 0 & 0 & 1 & 0 \\ 0 & 0 & 0 & (1+2\alpha)/3 \end{pmatrix} \tag{7.1.4}$$

This initial state produces the maximal amount of entanglement when arranged in the form equivalent under local unitaries to

$$\rho_{\mathrm{pp,ent}} = \frac{1}{\mathcal{Z}} \begin{pmatrix} (4+2\alpha)/6 & 0 & 0 & (2-2\alpha)/6 \\ 0 & (1+2\alpha)/3 & 0 & 0 \\ 0 & 0 & (1+2\alpha)/3 & 0 \\ (2-2\alpha)/6 & 0 & 0 & (4+2\alpha)/6 \end{pmatrix} \tag{7.1.5}$$

The partial transpose of this matrix has a zero crossing when

$$2\alpha + \alpha^2 = 0 \tag{7.1.6}$$

and so the only ‘physical’ zero crossing occurs at $\alpha = 0$. Of course, these calculations assume that the nuclear spin polarisation is negligible; in the regime of $\alpha \approx 0$ the polarisation of the nucleus would have to be considered in this calculation. This would allow for a small but nonzero threshold for α depending upon the nuclear spin isotope.

For ii), the maximally entangled state is equivalent under local unitaries to

$$\rho_{\text{thermal,ent}} = \frac{1}{\mathcal{Z}} \begin{pmatrix} (1+\alpha)/2 & 0 & 0 & (1-\alpha)/2 \\ 0 & \alpha & 0 & 0 \\ 0 & 0 & 1 & 0 \\ (1-\alpha)/2 & 0 & 0 & (1+\alpha)/2 \end{pmatrix} \tag{7.1.7}$$

The partial transpose of this matrix has a positive zero crossing when $\alpha = -3 + 2\sqrt{2}$, so entanglement is possible below $\alpha \approx 0.17$.

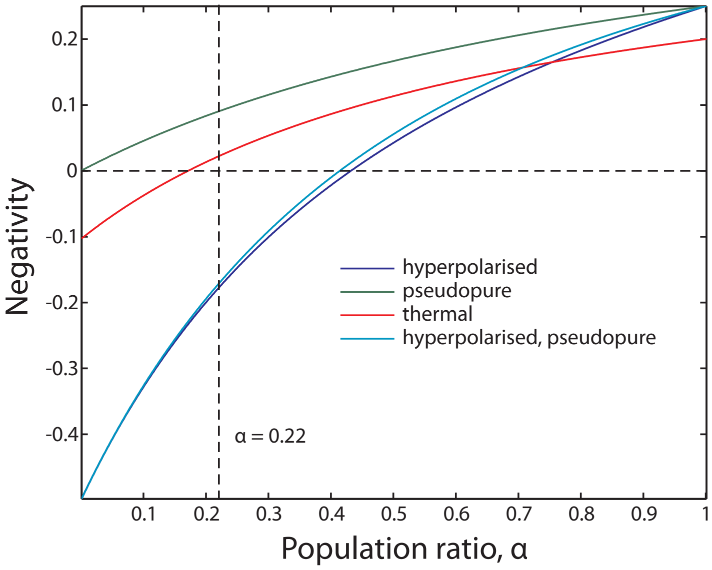

Figure 7.2: **Negativity of states prepared using pulsed hyperpolarisation, pseudopure preparation, neither and both.** These curves reveal both the zero crossings and the resulting negativity as a function of α for various preparation strategies. The dashed line indicating $\alpha = 0.217(2)$ represents the measured spin temperature value in the experiments reported here and hence the best possible negativity at this field and temperature is -0.191.

For iii), the maximally entangled state is equivalent under local unitaries to

$$\rho_{\text{hyper,pp,ent}} = \frac{4}{\mathcal{Z}^2} \begin{pmatrix} (3+2\alpha+\alpha^2)/6 & 0 & 0 & (3-2\alpha-\alpha^2)/6 \\ 0 & \alpha(2+\alpha)/3 & 0 & 0 \\ 0 & 0 & \alpha(2+\alpha)/3 & 0 \\ (3-2\alpha-\alpha^2)/6 & 0 & 0 & (3+2\alpha+\alpha^2)/6 \end{pmatrix} \tag{7.1.8}$$

The partial transpose of this matrix has a positive zero crossing when $\alpha = \sqrt{2} - 1$, and so entanglement is possible below $\alpha \approx 0.4142$.

Of these strategies, pulsed hyperpolarisation followed by entangling the greatest and second-smallest populations has the highest crossing-point and, for a given α, also the highest quality of entanglement measured by the positive partial transpose, as shown in Figure 7.2. This is the approach adopted in the present work [SBR$^+$11].

7.1.3 COMPLETE PULSE SEQUENCES

The spin temperature measurement revealed a value of $\alpha \leq 0.217(2)$, and so the target state is:

$$\rho_{\text{target}} = \begin{pmatrix} 0.4108 & 0 & 0 & 0.2643 \\ 0 & 0.0318 & 0 & 0 \\ 0 & 0 & 0.1465 & 0 \\ 0.2643 & 0 & 0 & 0.4108 \end{pmatrix} \tag{7.1.9}$$

This state is obtained with the sequence shown in Figure 7.3.

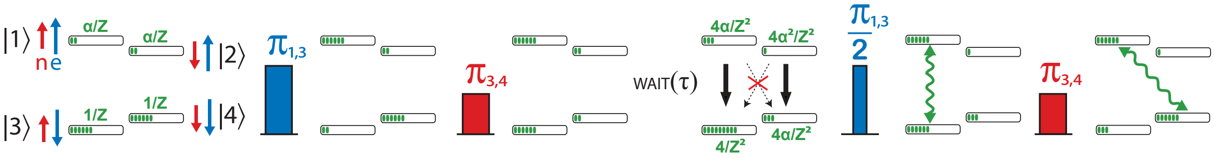

Figure 7.3: **Generating entanglement in ^{28}Si:P.** The initial state is at thermal equilibrium where populations (green) are distributed according to the electron spin polarisation at this magnetic field and temperature. A pair of microwave and radiofrequency π pulses move spin populations to favour the $|\Uparrow\rangle$ nuclear spin state, and after a time wait$(\tau) >> T_{1E}$ the hyperpolarised initial state is prepared. The entangled state is then formed by a coherence-generating microwave $(\frac{\pi}{2})_{1,3}$ pulse followed by a radiofrequency $\pi_{3,4}$ pulse, creating a superposition of $|1\rangle$ and $|4\rangle$.

The tomography process includes labelling each eigenstate with a phase that varies per shot with R^Z rotations. These gates can be implemented with the four pulses $\varphi^Z_{1,3} =$

$(\pi)^X_{1,3} : \pi_{1,3}^{\cos(\varphi/2)\sigma_X + \sin(\varphi/2)\sigma_Y}$ and $\theta^Z_{3,4} = (\pi)^X_{3,4} : \pi_{3,4}^{\cos(\theta/2)\sigma_X + \sin(\theta/2)\sigma_Y}$ to form the unitary

$$\begin{pmatrix} e^{+i\varphi/2} & 0 & 0 & 0 \\ 0 & 1 & 0 & 0 \\ 0 & 0 & e^{-i\varphi/2+i\theta/2} & 0 \\ 0 & 0 & 0 & e^{-i\theta/2} \end{pmatrix} \tag{7.1.10}$$

Tests upon this tomography scheme were presented in Chapter 6. After the phase of each eigenstate is appropriately labelled, each coherence is moved to the observable transition which is taken to be $\{1,3\}$. To record any coherence between $|1\rangle$ and $|3\rangle$ one does not require any pulses, whereas to record any coherence between $|2\rangle$ and $|4\rangle$ one must apply four pulses, namely $\pi^X_{3,4} : \pi^X_{1,3} : \pi^X_{2,4} : \pi^X_{3,4}$. Four pulses are required because the $\{1,2\}$ nuclear transition is unavailable. In some instances, final refocusing $\pi^X_{1,3}$ pulses are required to form an echo; deducing whether or not such refocusing pulses are required can be done by using the parity chart technique introduced in Section 3.7. The full pulse sequences can be seen in Figure 7.4.

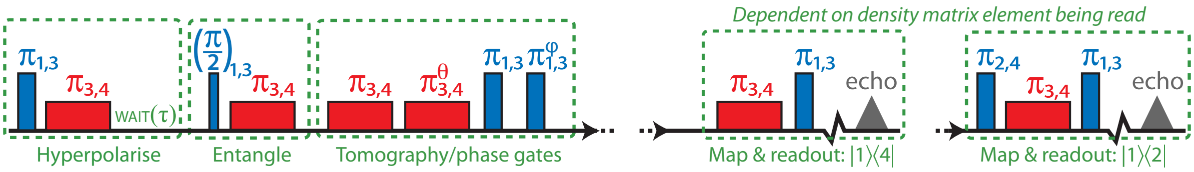

Figure 7.4: **Complete sequences for creating and measuring entanglement.** The full pulse sequence used to prepare, entangle and measure the two-spin state. The pulse $\pi^\theta_{3,4}$ is shorthand for the pulse $\pi_{3,4}^{\cos(\theta/2)\sigma_X + \sin(\theta/2)\sigma_Y}$, and similarly for $\pi^\varphi_{1,3}$. The final readout stage was changed according to the density matrix element being measured: two examples are shown for the $|1\rangle\langle 2|$ and $|1\rangle\langle 4|$ coherences.

7.1.4 Results and discussion

The results of this tomography process are given by:

$$\begin{pmatrix} 0.382 & 0.003+0.000i & -0.035-0.039i & 0.272 \\ 0.003-0.000i & 0.017 & -0.000+0.001i & 0.001+0.003i \\ -0.035+0.039i & -0.000-0.001i & 0.174 & -0.055-0.042i \\ 0.272 & 0.001-0.003i & -0.055+0.042i & 0.427 \end{pmatrix} \tag{7.1.11}$$

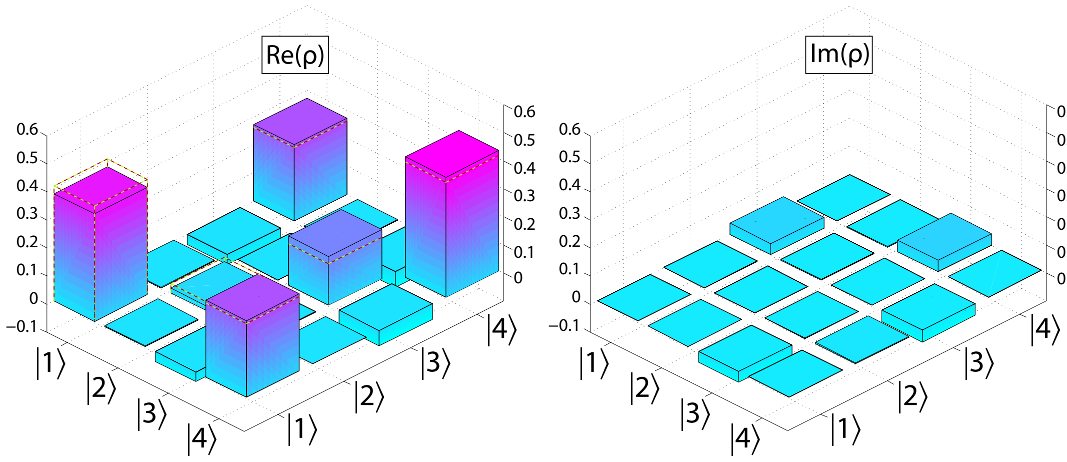

Figure 7.5: **Entangled density matrix obtained with quantum state tomography.** The obtained density matrix is shown as solid bars, while the dashed outline (zero where not shown) shows that of an ideal state given $\alpha = 0.217$.

which is illustrated in Figure 7.5. The target matrix is indicated by the dashed lines for comparison [SBR+11].

The fidelity of the measured state with the target state is calculated as 98%. This can be used to infer that the pulses used were of sufficiently high fidelity to warrant disregarding the errors associated with pulse imperfections. The remaining errors on each element due to noise amount to less than 0.04 on each element. Monte-Carlo generation of matrices can be used to determine the measured state's negativity, concurrence and fidelity with the target matrix. The results of these simulations are on display in Figure 7.6, registering a negativity of $-0.19(1)$ and concurrence of $-0.43(4)$, each of which confirm the presence of finite entanglement because these tests are both necessary and sufficient.

To achieve higher purity entangled states one could move to lower temperatures, e.g. if these experiments were performed at 0.8 K we would expect a concurrence of ~ 0.99 and a negativity of ~ -0.495 (where a pure Bell state registers values of $+1$ and $-1/2$, respectively). Complementary to this approach, entanglement purification could be performed using a larger Hilbert space at each node [Cam07], for example using a donor atom with a higher nuclear spin such as bismuth. Additionally, the sequences and analysis presented here could be applied to single-spin ^{28}Si:P technologies in development elsewhere [MPZ+10].

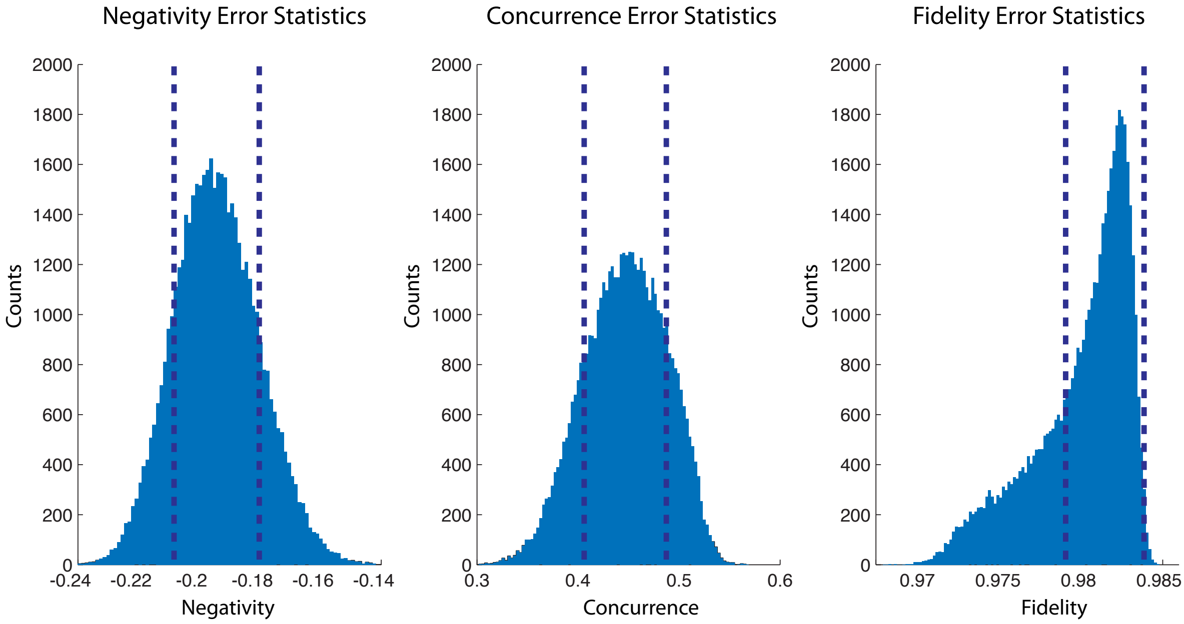

Figure 7.6: **Monte-Carlo analysis of fidelity, negativity and concurrence**. For the density matrix given in Equation 7.1.11 the resulting Monte-Carlo simulations of the uncertainty of the state's negativity, concurrence and fidelity are shown above, and result in a negativity of -0.19(1), concurrence of -0.43(4) and fidelity of 98.2(2)% with the ideal target state.

The electron-nuclear spin entanglement generated here could also be mapped into an entangled state between nuclear spin pairs. By SWAPping the state of the electron spin with a second, coupled nucleus, for example, one could attain nuclear-spin entanglement in a regime where the thermal polarisation of the nuclei would be orders of magnitude too small and the direct coupling between them weak [JSD07].

7.2 Nuclear-nuclear pseudo-entanglement using DMFPH

Although nuclear spins are advantageous as qubits due to their long coherence lifetimes, they exhibit very slow spin interactions and have weak polarisation. Through hyperpolarisation sequences, a coupled electron spin can be used to polarise nuclear spins and implement fast nuclear R^Z rotations through geometric operations. Unfortunately, the permanent presence of electron spins is a source of nuclear decoherence. The nuclear spin coherence time can be strongly limited by electron spin relaxation or electron spin flip-flop processes [MTB+08]. A better strategy therefore invokes an electron spin only at certain key times, for example to hyperpolarise the nuclear spins at the beginning of an algorithm, or to perform fast logic gates, so that there is minimal long-term impact on nuclear decoherence.

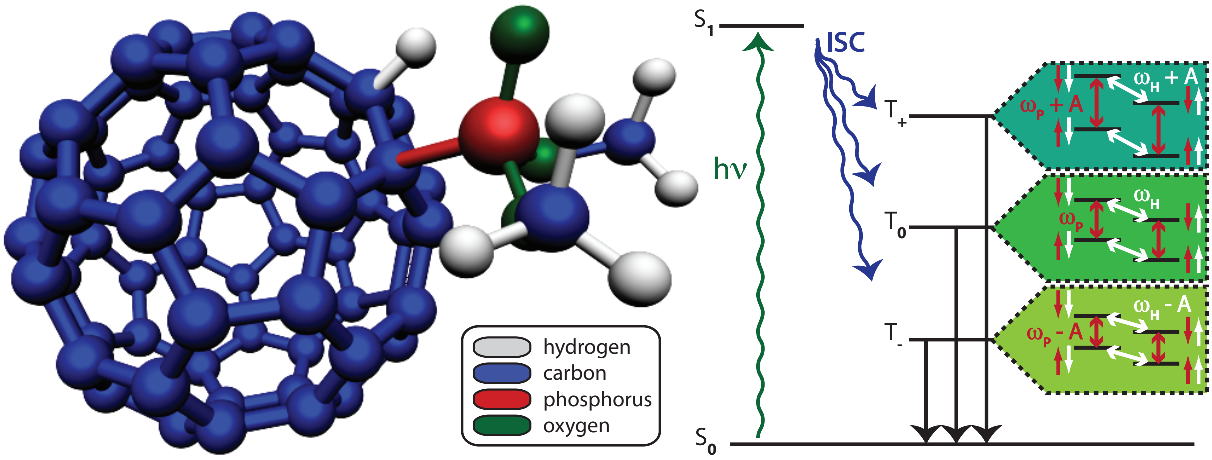

Figure 7.7: **DMFPH: physical system and schematic energy level diagram.** The ground electron state orbiting the cage can be temporarily excited into a triplet state through an excited singlet state followed by intersystem crossing (ISC). These triplet sublevels are preferentially populated in different amounts depending upon the molecular orientation and magnetic field. Some of these states are long-lived, which initialises the triplet after each photoexcitation pulse. These triplet states each are broken into four nuclear sublevels corresponding to the spin states of the ^{31}P and ^{1}H spins directly bonded to the C_{60} cage. The four nuclear sublevels in the T_0 subspace are the levels used for the nuclear-nuclear pseudo-entanglement described in this section.

One method of controlling the paramagnetic presence of an electron spin is to optically excite it from a diamagnetic singlet ground state into a long-lived paramagnetic triplet state. A variety of systems are known to support these dynamics including C_{60} molecules and their derivatives. To explore the possibility of generating nuclear-nuclear entanglement using transient electron spins, a C_{60} derivative was identified which possesses two spin-active nuclei directly bonded to the C_{60} molecule, known as dimethyl fullerene phosphine oxide or DMFPH. This molecule has a diamagnetic singlet ground state S_0 which can be photoexcited to populate the first excited single state S_1. This state undergoes intersystem crossing (ISC) to a long-lived triplet state which is paramagnetic. An illustration of this molecule and a simplified energy level diagram is shown in Figure 7.7.

7.2.1 Electronic characteristics

We will examine two principal electronic transitions available to the triplet state: the transition between the triplet state T_0 and the triplet states T_- and T_+, at 350 mT [1]. If each of these levels were equally populated, there would be no observable population differences. However, if the ISC or the relaxation properties to the singlet ground state S_0 are spin-selective, the T_0 state can be populated differently from the others and a population difference between the T_0 state and the other triplet sublevels can be observed. These population differences can be both positive and negative, leading to absorption (positive amplitude) and dispersion (negative amplitude) traces in the echo-detected EPR spectrum.

This molecule can be dissolved into a toluene solution and frozen for EPR experiments at low temperatures. The orientations of the DMFPH molecules are randomly distributed with respect to the background magnetic field, and so any orientation dependence of the electronic transitions broadens a particular transition in the molecule's spectrum. In this example, shown in Figure 7.8, the spectrum of the sample is very broad — tens of millitesla wide — and the curve corresponding to the T_0:T_- transitions overlaps the T_0:T_+ curve. The populations of the triplet levels also depend upon the molecular orientation, and the spectrum includes all of this information, which can be modelled. For a fixed microwave frequency, this modelling allows for the identification of a field position which has no contributions from T_0:T_+ transitions and large contributions from T_0:T_-, which will be referred to as the $X_{0,-}$ transition. This transition is used in this work to optimise the nuclear characteristics of the system, which will now be discussed.

---

[1] The other electronic transistion, $\Delta m_S = 2$ transition between T_- and T_+, is available when the magnetic field is halved.

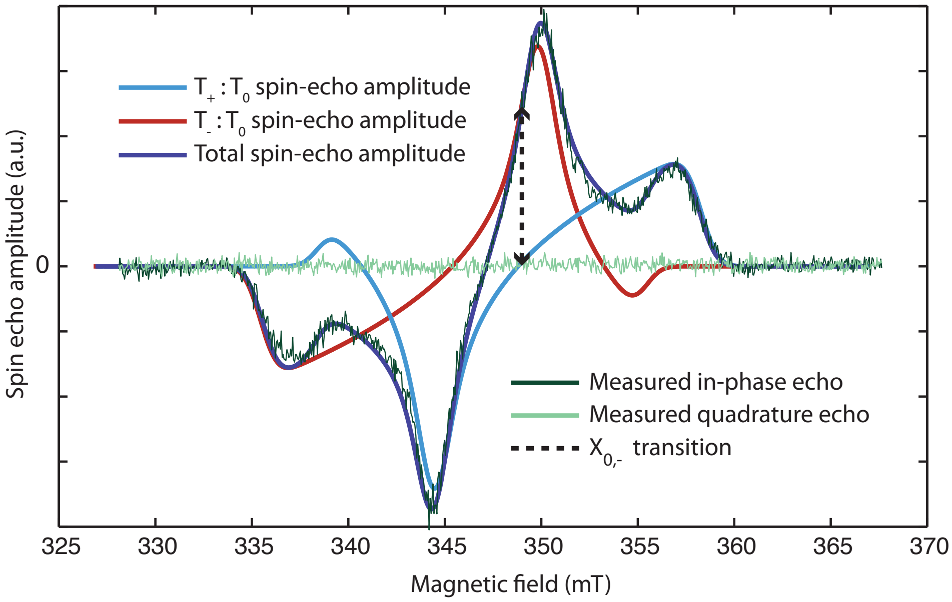

Figure 7.8: **DMFPH: field sweep and modelled fit.** An example field swept-spectrum of DMFPH can be modelled to reveal the orientation and field-dependent triplet state transitions alongside their population differences. Here the $X_{0,-}$ transition is identified which only has net contributions from T_0:T_- electronic transitions.

7.2.2 Nuclear characteristics

The triplet has a spin density which varies across the entire molecule and strongly interacts with the $S > 0$ nuclear spins adjacent to the C_{60} cage[2]. Consequently, each of the triplet states are split into four sublevels by the phosphorus Zeeman interaction and the hydrogen Zeeman interaction. Additionally, there exist hyperfine interactions between the electron triplet and two nuclear spins, which modifies these nuclear transition frequencies in the T_+ and T_- subspaces. In contrast with the nuclear Zeeman interaction, which produces a narrow NMR linewidth because the interaction is similar across all nuclear spins, the hyperfine interactions depend upon the molecular orientation and in this instance both shift and broaden the nuclear transitions in the T_+ and T_- subspaces.

The hyperfine interactions ($\mathcal{A}_{\mathrm{H}} = 6.0$ MHz and $\mathcal{A}_{\mathrm{P}} = 11.0$ MHz) are responsible for shifting the frequencies of electronic transitions depending upon the nuclear state [Fil11]. Specifically, the transition between the $|\mathrm{T}_0, \uparrow\uparrow\rangle$ and $|\mathrm{T}_-, \uparrow\uparrow\rangle$ eigenstates differs from the

---

[2] the hydrogen spins on the arms of the phosphine adduct have a low electron spin density and so their contributions are assumed to be negligible.

$|\mathrm{T}_0,\uparrow\downarrow\rangle : |\mathrm{T}_-,\uparrow\downarrow\rangle$ transition, where the eigenstates are expressed in the $|\mathrm{T}_0,{}^1\mathrm{H},{}^{31}\mathrm{P}\rangle$ spin product basis. Correspondingly, if the bandwidth of the microwave pulse is less than 6.0 MHz, the triplet electron spin can be manipulated conditional upon a particular nuclear spin state. The nuclear populations for each triplet sublevel are assumed to be initialised evenly; a microwave pulse longer than $\approx$ 200 ns on the $X_{0,-}$ transition can therefore selectively swap populations between a particular nuclear sublevel in the T_0 subspace and that same nuclear sublevel in the T_- subspace.

An ENDOR experiment applied with microwaves tuned to the $X_{0,-}$ transition reveals two very narrow transitions, corresponding to the T_0 phosphorus and hydrogen transitions, and two broadened nuclear transitions corresponding to the T_- phosphorus and hydrogen transitions. The integrated amplitude of these transitions reveal the quality of state initialisation in the respective electronic subspace, because for high-fidelity nuclear operations the ENDOR sequence is a measure of nuclear population differences. By choosing to work with the $X_{0,-}$ electronic transition, the integrated amplitude of the two nuclear transitions are approximately equal after calibrating equal-length π pulses. Due to the hyperfine interaction, other electronic transitions may have contributions from both T_0:T_- and T_0:T_+ transitions which can populate more than one T_0 sublevel at a given orientation, leading to a lower quality of state initialisation. Explicitly, for one fixed orientation, the hyperfine values shift the four electron and nuclear Zeeman eigenstates of the T_+ subspace by $\pm\mathcal{A}_\mathrm{H}/2 \pm \mathcal{A}_\mathrm{P}/2$ and the four eigenstates of the T_- subspace by $\mp\mathcal{A}_\mathrm{H}/2 \mp \mathcal{A}_\mathrm{P}/2$ depending upon nuclear spin, and so two electronic transitions are available at any particular choice of frequency. Moving to a field position with no spin-echo contribution from T_0:T_+ transitions preferentially populates one nuclear sublevel within the T_0 subspace and acts as a pseudopure initialisation technique for that subspace.

The T_0 subspace permits high-fidelity nuclear operations because of the very narrow nuclear transition linewidths. A fit of the Rabi oscillations reveals a 96(1)% and 97(1)% fidelity π pulse for the ${}^{31}\mathrm{P}$ and ${}^{1}\mathrm{H}$ transitions, respectively. Unfortunately the generation of nuclear-nuclear entanglement within this subspace is met with some challenges. The scheme discussed at the end of Section 7.1.4, involving a SWAP of an entangled electron's state with that of a second nucleus, cannot be supported by this system due to the very short T_{2E} of the triplet electron spin: in this system T_{2E} is much shorter than the time required to perform a nuclear π pulse. The triplet electron spin can be used for nuclear hyperpolarisation, however the coherence must be generated from within the T_0 subspace. Generating nuclear-nuclear entanglement directly within the T_0 subspace requires selective operations, which are not directly available because of the absence of the hyperfine interaction: the nuclear transitions are nearly degenerate.

In addition to the hyperfine interaction, the nuclear spins are coupled to each other through the solid-state dipolar interaction. This coupling can be used to perform CNOT operations with nonselective pulses as was introduced in Section 3.7. In the liquid state, nuclear interactions between the spin-active phosphorus and hydrogen atoms joined to the C_{60} cage are weak; the measured J-coupling between them is 30 Hz. CNOT operations exploiting this weak coupling require a minimum time of 16 ms. Fortunately, in the solid state, the nuclear dipolar interaction can be significantly stronger allowing for much faster selective nuclear operations.

7.2.3 Entangling operations using enhanced couplings

One scheme for measuring the nuclear couplings in the presence of an electron is known as *spin echo double resonance* (SEDOR). This sequence and the data it generates when applied to DMFPH is shown in Figure 7.9. The SEDOR sequence is based upon a nuclear Hahn echo sequence where the triplet electron spin is used for initialisation and readout. To read out any nuclear coherence through an electron with a very short T_{2E} it must first be projected onto a population on the nuclear sublevel on resonance with the $X_{0,-}$ electronic transition. It is for this reason that the nuclear Hahn echo takes the form $(\frac{\pi}{2})^X_H : \mathrm{wait}(\tau) : \pi^X_H : \mathrm{wait}(\tau) : (\frac{\pi}{2})^X_H$. By extending wait($\tau$), this Hahn echo sequence can be used to measure T_{2H}, and when applied to the phosphorus transition extending τ can reveal T_{2P}. The refocusing π^X pulse in a Hahn echo sequence refocuses any couplings between the spin under investigation and its environment, which includes any dipolar couplings. To detect dipolar couplings, the parity of the coupling must be refocussed as well, which is accomplished with a simultaneous π^X pulse on the second nuclear spin (as is done with standard NMR CNOT sequences). The only modification required for final detection in a SEDOR sequence is a final π^X pulse on the second nucleus immediately prior to readout: this is to return the state to the correct nuclear subspace for projective readout. By extending the delay in this SEDOR sequence, one can observe oscillations in the measured amplitude. These oscillations correspond to multiple iterations of a CNOT operation using the enhanced nuclear coupling of 3kHz. For more details on the application of SEDOR to DMFPH see Reference [Fil11].

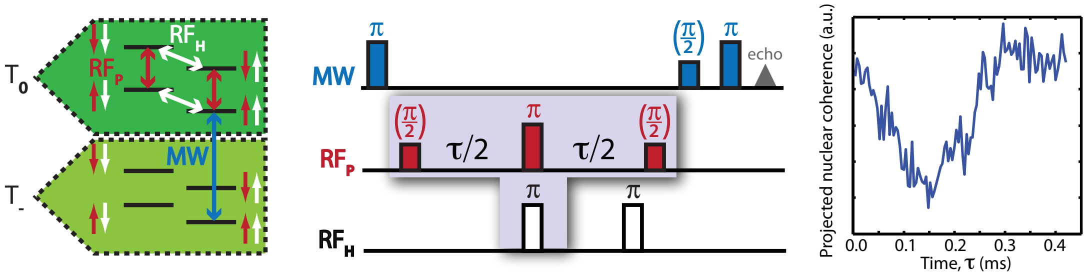

Figure 7.9: **DMFPH: SEDOR experiment to determine enhanced nuclear coupling.** A technique based on the spin echo double resonance (SEDOR) sequence can be used to measure the dipolar coupling between spins. The sequence resembles a Hahn-echo experiment on one spin (^{31}P), however both spins are flipped during the refocusing pulse such that the parity of their coupling remains unchanged and the nuclear coupling is not refocused. Microwave pulses before and after are used to prepare and measure the ^{1}H nuclear spin coherence, and the final π pulse on ^{1}H moves the coherence back to the correct subspace for projective readout. The highlighted part of this sequence with $\tau = 1/2J$ corresponds to a CNOT operation acting upon ^{31}P conditional upon ^{1}H.

For the purposes of generating nuclear-nuclear pseudo-entanglement, this enhanced nuclear coupling allows for fast nuclear operations on the order of 160 μs. Given that the triplet state relaxes to the singlet ground state on the timescale of $\approx$ 300 μs, this in principle allows for two CNOT operations within a single experimental shot. This would be sufficient to create a pseudo-entangled state and measure it using quantum state tomography.

7.2.4 Quantum state tomography of the T_0 subspace

Any quantum state tomography performed with DMFPH is subject to a few limitations. The principle limitation of tomography performed with frozen-solution DMFPH is the labelling of nuclear eigenstates. There are a number of different orientations that make up the $X_{0,-}$ transition, and the nuclear spin state along this transition need not be common to each of these orientations. Therefore the gathered density matrix is determined with respect to an effective eigenbasis, where eigenstate $|4\rangle$ is defined to be the orientation-dependent nuclear eigenstate associated with the $X_{0,-}$ transition. The effective eigenstates $|3\rangle$ and $|2\rangle$ differ from $|4\rangle$ by a ^{1}H and ^{31}P spin flip, respectively, and $|1\rangle$ differs from $|4\rangle$ by a flip of both nuclear spins. This poses a problem for the R^Z coherence labelling introduced in Chapter 6. The R^Z operations can be applied geometrically as before, however they are not selective and so a φ_P^Z gate followed by a θ_H^Z gate results in the unitary:

$$\begin{pmatrix} e^{+i\varphi/2+i\theta/2} & 0 & 0 & 0 \\ 0 & e^{+i\varphi/2-i\theta/2} & 0 & 0 \\ 0 & 0 & e^{-i\varphi/2+i\theta/2} & 0 \\ 0 & 0 & 0 & e^{-i\varphi/2-i\theta/2} \end{pmatrix} \tag{7.2.1}$$

which does not distinguish between the coherences $|1\rangle\langle 3|$ and $|2\rangle\langle 4|$, nor between the coherences $|1\rangle\langle 2|$ and $|3\rangle\langle 4|$. This is acceptable[3] given high-fidelity nuclear π pulses and the fact that the final measurement only measures the population difference between $|4\rangle$ and its matching nuclear eigenstate in T_-. The important problem with the mixed labelling of eigenstates is not the single quantum coherences; regardless of the spin state of $|4\rangle$ the single quantum coherences evolve according to the correct absolute frequency. What differs is the response of the generated entangled coherences.

To illustrate this, consider how the θ_H^Z gate acts upon a coherence between $|3\rangle$ and $|4\rangle$. Depending upon the actual spin state of $|3\rangle$ and $|4\rangle$, a geometric θ_H^Z gate will either apply a positive rotation to $|3\rangle$ or a positive rotation to $|4\rangle$. This can be understood as θ adopting either a positive or negative value depending upon the actual spin state of $|4\rangle$.

---

[3] In Section 7.2.5 I discuss a technique able to resolve this imperfection in the tomography sequence.

Because the final measurement is projective, one does not distinguish between positive and negative frequencies and so the operator θ_H^Z acts equivalently in both instances. Entangled quantum states however record either the sum or difference of these two phase rotations, which identifies the relative sign of θ and φ. Therefore, the phase evolution of the entangled quantum coherence can reveal both the sum and the difference frequencies depending upon which nuclear spin states make up the eigenstate $|4\rangle$. This cannot be easily distinguished from pulse errors which can also give rise to erroneous frequencies, which is a large limitation of this tomography method. A thorough model of this system can reveal the composition of $|4\rangle$, however if the nuclear π pulses are of sufficiently high fidelity to plausibly assume negligible rotation errors, which is the case here, one can use the relative strength of the two frequencies to infer the composition of $|4\rangle$. Under such assumptions we infer from the resulting data that the composition of $|4\rangle$ is mostly made up of the $|\downarrow, \downarrow\rangle$ and $|\uparrow, \uparrow\rangle$ nuclear states. More modelling is required to understand why $|4\rangle$ should have this composition.

The second limitation of tomography applied to the T_0 subspace of DMFPH is the triplet recombination lifetime, which is temperature-independent below 50 K at ≈ 0.34 T. The amplitude of any final electronic spin-echo measurement depends strongly on the length of time passed since the initial photoexcitation pulse. To ensure relaxation effects do not corrupt the quality of the tomography, all tomography measurements, including the population measurements and reference amplitudes, must be taken at the same final echo position with the same τ delay between the microwave π and $\pi/2$ pulses. In order to relate the final electron spin echo amplitude to a σ_z measurement of of the nuclear spins, nuclear Rabi oscillations are performed. Such a measurement ignores population common to all levels in the T_0 subspace, and so the experiments here are performed under the pseudopure approximation.

The full pulse sequences including the entangling operations and quantum state tomography can be seen in Figure 7.10. The total time taken for such sequences using the dipolar coupling and 16 μs nuclear π pulses is 448 μs. Although the definition of the ensemble is restricted to the set of triplet states present 448 μs after initial photoexcitation for the purposes of tomography, without this restriction the overall fidelity

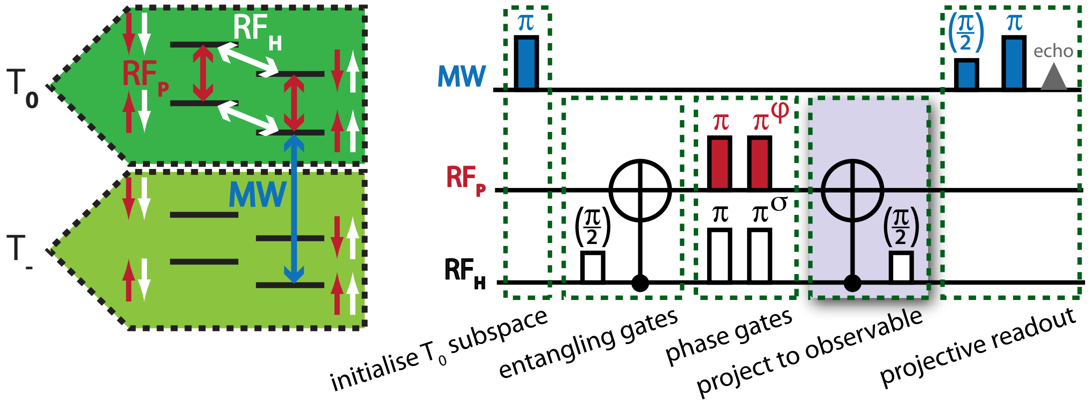

Figure 7.10: **Full pulse sequences for projective tomography in DMFPH.** Nuclear states of the T_0 subspace in DMFPH are measured projectively through the triplet electron spin, and so the populations and the coherences are projected onto the state $|4\rangle$, shown in the left panel as $|\uparrow, \uparrow\rangle$. The highlighted section changes depending upon which density matrix element is being measured — the example shown is for the entangled quantum coherence. Measuring the populations of the four eigenstates require at most two nuclear π pulses; coherences require a $\pi/2$ to project them onto a population plus an additional CNOT gate for multiple quantum coherences. Refocusing pulses are omitted from the figure for clarity.

of this operation is very low. For higher fidelity operations, given this triplet lifetime, even shorter entangling gate times are required. This can be achieved by using the $X_{0,-}$ triplet electron spin transition to apply conditional geometric phase gates — also known as CPHASE gates — to the nuclear spins [SLG11]. As explained in Section 2.2.3, the sequence $(\frac{\pi}{2})^X$: CPHASE : $(\frac{\pi}{2})^X$ is a CNOT operation, which can be used in place of the dipolar coupling CNOT gates in the full sequences described above.

7.2.5 ENTANGLING OPERATIONS USING GEOMETRIC GATES

If a quantum state is taken through a closed-loop trajectory in Hilbert space, it acquires a geometric phase equal to half the solid angle mapped out by that trajectory as explained in Section 2.2.2. Because the field is on-resonance with the $X_{0,-}$ electronic transition corresponding to the collection of the ^{1}H and ^{31}P nuclear spins in the state $|4\rangle$, we can apply a selective microwave pulse which only rotates the triplet electron spin when the nuclear spins are in the state $|4\rangle$, whatever that nuclear state may be. Applying a 2π pulse to the triplet electron spin in this way imparts a π phase shift to the $|4\rangle$ state with respect to the others in the T_0 subspace, which is equivalent to a CPHASE operation. This selective π^Z operation is fast; its duration is limited only by the hyperfine coupling strength which determines the minimum bandwidth of the microwave pulse. In this way an entangling operation on the timescale of hundreds of nanoseconds can be performed[4].

To illustrate how this phase gate can be applied to the individual nuclear spins, I applied 2π microwave pulses while driving nuclear Rabi oscillations (see Figure 7.11). I verified that this CPHASE behaviour was conditional by observing uninterrupted Rabi oscillations on the complementary nuclear subspace.

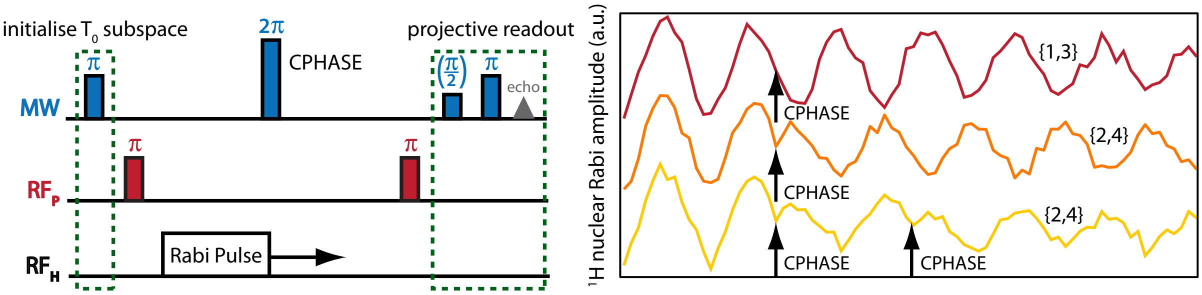

Figure 7.11: **Ultrafast conditional phase gates.** A CPHASE operation can be used for fast entangling operations on the T_0 subspace. To test these CPHASE operations one can drive nuclear Rabi oscillations and at selected points perform π^Z operations using 2π microwave pulses, which impart a geometric phase of π onto the state $|4\rangle$. Optional leading and trailing π pulses on the ^{31}P nuclear spin confirm that this phase gate is in fact conditional: an uninterrupted trace of Rabi oscillations on the $\{1,3\}$ subspace is shown in red on the right. Without π pulses on the ^{31}P spin one observes fast π^Z rotations during Rabi oscillations on the $\{2,4\}$ subspace, as indicated by the black arrows in the other two traces. The 2π microwave pulse is chosen to have the same bandwidth as the π microwave pulse to improve the fidelity of this CPHASE operation; the residual loss in signal amplitude is due to microwave inhomogeneities across the sample.

---

[4] By modifying the axis of rotation of the second microwave π pulse, one could impart an arbitrary R^Z rotation which would be suitable for tomography in distinguishing between different single quantum coherences. This would be necessary if the nuclear π pulses displayed a low fidelity which they do not.

These two entangling operations were used to generate and perform quantum state tomography upon DMFPH. The dipolar coupling based CNOT operations already refocus the nuclear spins at the one-quarter and three-quarter points in the sequence, however the geometric entangling operation provides no such refocusing and so additional π pulses are required mid-way through the sequence. No other changes are required. The results of these experiments, using both types of entangling operations will now be presented and discussed.

7.2.6 Results and discussion

The measured oscillations of the multiple quantum coherence respond according to the sum of the two applied frequencies, which matches a double quantum coherence behaviour and indicates that the $|4\rangle$ is mostly made up of the $|\downarrow,\downarrow\rangle$ and/or $|\uparrow,\uparrow\rangle$ nuclear states. For tomography purposes, the $|4\rangle\langle 1|$ is assigned this double quantum coherence (DQC) oscillation frequency. The $|4\rangle\langle 1|$ oscillations display a second, lower-amplitude frequency component which evolves according to the difference of these two frequencies, with a relative amplitude of approximately 1:3 compared to the dominant DQC frequency (See Figure 7.12). The second entangled quantum coherence reveals a dominant ZQC frequency and a lesser DQC with approximately this same ratio, however these could both be due to pulse imperfections or initialisation imperfections as explained above.

In Figure 7.13 we compare the density matrices obtained using the two different implementations of the CNOT gate: through the natural dipolar coupling of the nuclei and through the geometric CPHASE operation combined with Hadamard gates. The fidelities of the final pseudopure density matrices with respect to an ideal Bell state are 35% and 69% respectively, and their pseudopure negativities are -0.11(5) and -0.19(4), respectively. The increased fidelity of the latter sequence is due primarily to the shorter and higher quality entangling operations. The geometric entangling gate is performed in 0.2 μs, and applies to all nuclear configurations that make up the state $|4\rangle$. In contrast, the CNOT based on the dipolar coupling had a duration of 160 μs, and the dipolar coupling evolves the superposition state differently depending upon which nuclear states make up the state $|4\rangle$. The residual imperfection with the CPHASE-based sequence is partially due to the

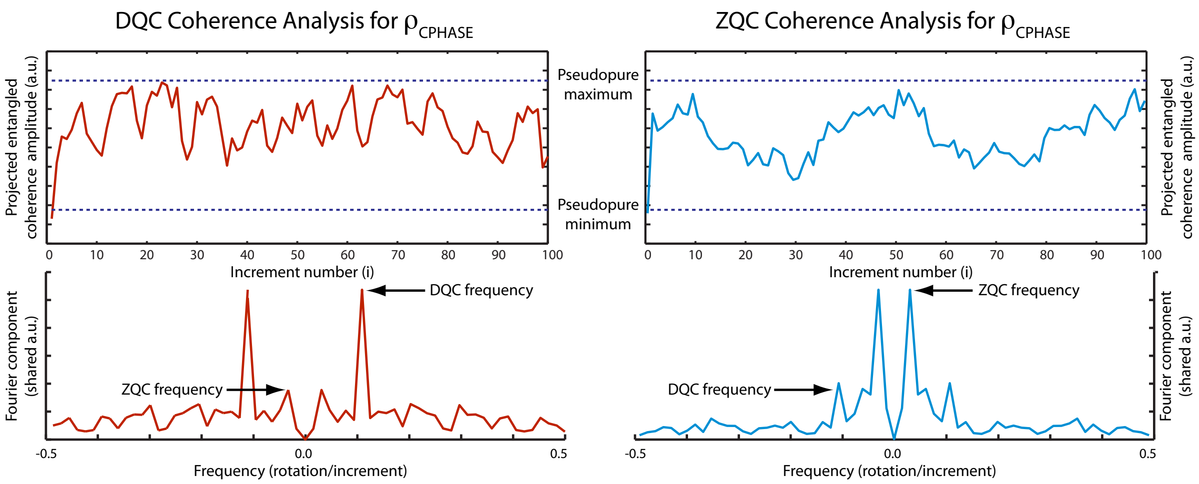

Figure 7.12: **Coherence analysis**. The CPHASE entangling operations can be used to generate either a ZQC or a DQC and the observed oscillations due to the tomography process are shown above. Fourier analysis of both measurements reveal contributions from the other multiple quantum coherence, which could be due to systematic pulse errors or due to the composition of $|4\rangle$.

limited fidelity of the CPHASE operation, which is evident in Figure 7.11, and in combination with the errors of the other nuclear π pulses this can mostly account for the reduced amplitude of the entangled coherence. It is worth determining if decoherence affects the final state fidelity, and by measuring the relaxation rates of the various coherences in the system one can determine their effects.

The T_{1P} and T_{1H} times limit the lifetime of the DQC coherence and can be measured with a nuclear inversion-recovery experiment with a fixed final spin echo time. The times measured using this sequence exceed the lifetime of the triplet electron spin and so are not expected to play a role in the reduced DQC amplitude. The T_{2P} and T_{2H} times, measured to be 1.9(4) ms and 0.20(4) ms respectively using the Hahn echo technique described above, can provide a rough estimate for the decay rate of the entangled quantum coherence. In place of an estimate for the T_2 of the entangled coherence, it can be measured directly by extending the length of time on either side of the phase gates in the sequence given in Figure 7.10, which is explicitly given in Figure 7.14. These sequences involve refocussing pulses applied to both spins at the midway point: flipping both spins reverses the phase of a DQC or ZQC, but does not change one into the other. The lifetimes of

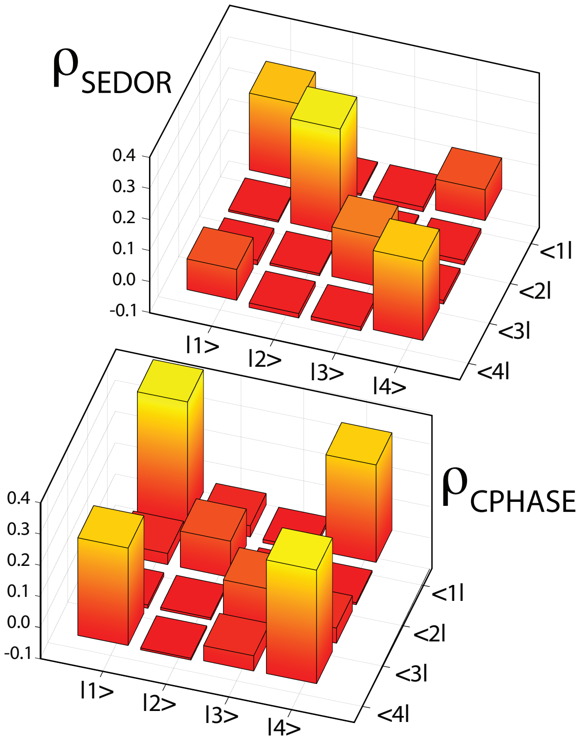

Figure 7.13: **Complete density matrices**. The pseudopure density matrices measured using projective quantum state tomography are given above under two different conditional operations. The state labelled ρ_{SEDOR} implements conditional operations using the nuclear dipolar coupling. The state labelled ρ_{CPHASE} implements conditional operations using selective geometric gates provided by a 2π microwave pulse. In both instances the target state is the Bell state $\frac{1}{\sqrt{2}}(|1\rangle + |4\rangle)$, with only the real part shown.

both a ZQC and a DQC coherence can be measured in this way and the results are shown in Figure 7.15.

A decoupling scheme involving a π pulse on each nuclear spin midway through the sequence does not refocus the dipolar coupling. This is indeed the way that nuclear couplings are used to perform a CNOT operation, and these effects will contribute to a modulation of the ZQC and DQC amplitudes with a frequency of 3 kHz. The decay of these coherences is seen to be on the order of 160 μs (specifically, $T_{2,\mathrm{DQC}} \approx 100$ μs and $T_{2,\mathrm{ZQC}} \approx 200$ μs, and does not recover in signal beyond this point, and so a second source of decoherence must be present which affects the multiple quantum coherences. To confirm that the dipolar coupling is not playing a role in the measured ZQC and DQC

DQC lifetime measurement:

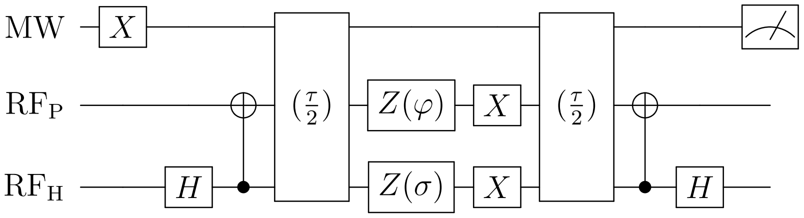

(7.2.2)

ZQC lifetime measurement:

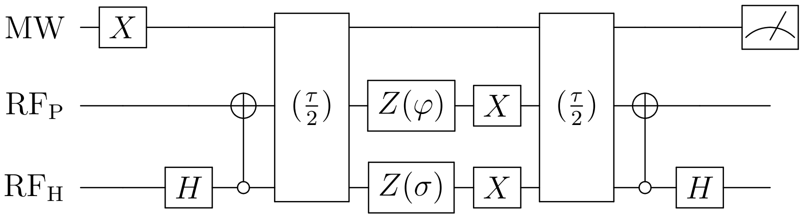

(7.2.3)

Refocused ZQC/DQC measurement:

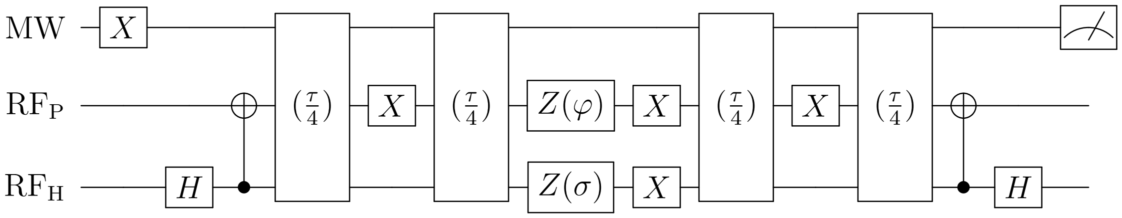

(7.2.4)

Figure 7.14: **Measuring lifetimes with DMFPH.** These sequences are used to determine the lifetimes of the ZQC and DQC coherences, as well as to test the effects of the dipolar coupling upon these coherences by refocusing its effects. The delay wait(τ) is written as just the time τ, the Hadamard matrix is implemented using a $\pi/2$ pulse, and the meter at the end of each sequence represents a microwave spin-echo population measurement.

decoherence times, a decoupling sequence can be used which removes the effects of the dipolar coupling. Additional refocusing pulses are applied to a single nucleus at the one-quarter and three-quarter points during this delay. This sequence, shown in Figure 7.14, takes an entangled quantum coherence through each of the four pseudopure Bell states, and so although it refocuses the effects of dipolar coupling, it should yield an average of the DQC and ZQC decoherence rates. Indeed, the results shown in Figure 6.14 reveal a lifetime midway between the ZQC and DQC, confirming that the dipolar coupling plays no dominant role in the faster relaxation mechanism of the multiple quantum coherences.

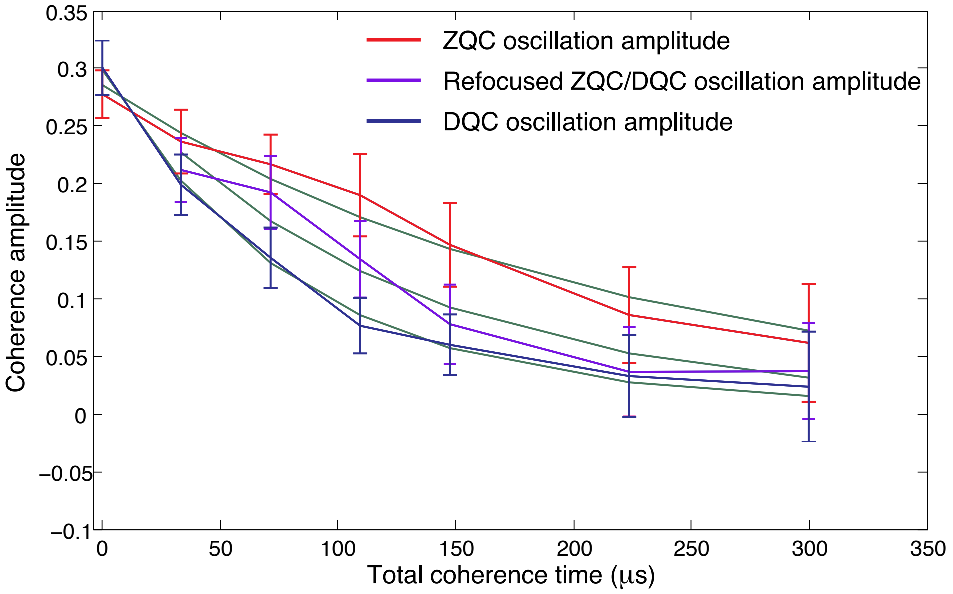

Figure 7.15: **Entangled coherence lifetimes.** Results of the measurements of various lifetimes of the system are shown above. Both the ZQC and the DQC coherences decay roughly an order of magnitude faster than the single quantum coherences in the system. By decoupling the effects of the dipolar coupling one sees no improvement to this lifetime, indicating that this shortened lifetime is due to some other source of dephasing in the system. Here $T_{2,\mathrm{DQC}} \approx 100$ μs and $T_{2,\mathrm{ZQC}} \approx 200$ μs.

Taking into account these relaxation times, the maximum expected fidelities for the pseudo-entangled states with uniform dipolar coupling and geometric entangling operations amount to 55% and 77%, respectively. These fast relaxation times largely account for the low recovered fidelities of the of the pseudo-entangled states (35% and 69% respectively[5]), indicating that the overall limitations with this entangling approach are the natural lifetimes of the system. It is possible that these coherence properties depend upon the orientation of the molecule. If the sample was prepared as a single crystal the excitation of a single orientation would lead to uniform T_0 subspace initialisation, and the orientation dependence of the relaxation mechanisms can possibly provide useful insight into the mechanism itself.

---

[5] These times do not compare favourably to a randomly generated state which would on average have a fidelity of 25%, however the pseudo-entangled state is generated in much less time than the total tomography sequence time, allowing one to infer a much higher fidelity at the time of generation.

Nuclear-nuclear entanglement using transient electron spins is most useful when the nuclear-nuclear entanglement outlives the photoexcited triplet state. These experiments have not shown any observable nuclear polarisation buildup surviving between successive photoexcitation events (separated by 100 ms); this can be attributed to the small proportion of photoexcited molecules compounded with the very orientation-selective pulses required to properly initialise the T_0 subspace. A single-orientation crystal can be used to dramatically improve the overall nuclear hyperpolarisation of the T_0 subspace because all the molecules will share the same orientation and hence particular electronic transitions. In addition, transitions from the T_+ subspace can also be used to hyperpolarise the T_0 subspace. To remove the electron triplet state as a source of decoherence, controlled de-excitation may be necessary due to the short lifetimes of the entangled quantum coherence. For example, this may be accomplished with a second optical pulse of a different wavelength chosen to excite the triplet into a more highly excited state which decays quickly into the singlet ground state. Once in the singlet ground state, NMR tomography of the nuclei could be used to test for the presence of ground state nuclear entanglement.

§ 8. CONCLUSIONS AND OUTLOOK

From the earliest work on quantum mechanics, the ideas underpinning entanglement have perplexed and intrigued philosophers and scientists alike. Demonstrations of fantastic phenomena including physical nonlocality, teleportation and unbreakable encryption have shown that entanglement not only exists but can be harnessed for technological gain beyond classical capabilities. Although the general relationship between quantum entanglement and mixed quantum computation remains elusive, most of the quantum algorithms demonstrating exponential enhancement over their classical counterparts exist only as pure-state algorithms and rely upon the complexity inherently present in unbounded entanglement. Other applications, such as quantum metrology, only require the use of mixed pseudo-entangled states.

In Chapter 4, I studied the role of entanglement in quantum metrology and demonstrated a sensitivity enhancement of separable, pseudo-entangled nuclear states over classical resources. This enhancement was experimentally demonstrated by measuring the local magnetic field using nuclear spins arranged as NOON states in molecular sensors. Two conceptual advancements over the basic sensor sequence to improve the accuracy and the precision of this pseudo-entanglement resource were presented. I implemented these improved pulse sequences on a few molecular sensors of different sizes to measure the local magnetic field with a sensitivity beyond the standard quantum limit.

Inspired by the enhanced sensitivity afforded by optimal state initialisation in Chapter 4, I considered nonunitary state initialisation techniques using donor qubits in silicon throughout Chapter 5. Various mechanisms for using the electrons' polarisation to hyperpolarise nuclear spins were discussed, and in particular a polarisation transfer technique was used which exploits the ratio between the nuclear and electronic relaxation to optimally hyperpolarise the coupled electron-nucleus system. I compared the nuclear hyperpolarisation effects of illuminated phosphorus and bismuth donors at high fields to probe the dynamics of these two important donor qubits in silicon.

Having investigated state initialisation techniques I turned to the implementation of scalable state measurement techniques in Chapter 6. A coherence-labelling scheme which is able to conservatively estimate the superpositions in the system was introduced and implemented using geometric Z gates. In conjunction with population measurements of the eigenstates, this tomography technique is able to determine the values and uncertainties of each element of a state's observable density matrix. I showed how the unobservable component of a density matrix can also be experimentally measured by exploiting the nonunitary techniques developed in the previous chapter, permitting a complete measurement of the state's full density matrix.

In Chapter 7, I hyperpolarised a ^{28}Si:P ensemble and manipulated it into an entangled state. This state was measured using quantum state tomography and the presence of finite entanglement was verified using two necessary and sufficient entanglement measures. Replicating these experiments with decreasing temperatures would generate entangled states which asymptotically approach a pure entangled state. This chapter also discussed the molecular system DMFPH which is able to possess a photoexcited transient electron spin for nuclear-nuclear pseudo-entanglement. I showed how this system also supports ultrafast entangling operations by making use of the geometric properties of the electron spins whose coherence times are too short to form electron-nuclear entanglement.

The ability to generate large amounts of fundamentally identical entangled qubit pairs on demand is an important step towards the development of an inherently scalable measurement-based quantum computer however it must be combined with ways to move quantum information between donor sites. The earliest proposed mechanism for coupling spatially separated sites involves specific donor placement, registered against electrostatic gates, to control wavefunction overlap and thus exchange coupling [Kan98]. A similar approach uses the different wavefunction overlap of the excited state [SFG03]. Alternatively, the ability to ionise the donor and transfer the electron to an adjacent donor site could be used to build up a large cluster state [Mor09]. Finally, with the recent demonstration of high fidelity single-shot single spin measurment [MPZ$^+$10], ideas such as parity measurements between multiple donors could be used to entangle spatially separated donor spins.

The experimental demands associated with building a quantum computer are numerous and complicated, and a scalable prototype remains many years away. The results of this thesis indicate that hybrid electron-nucleus spin systems are exceptionally promising, demonstrating the individual control and decoherence characteristics required of a scalable architecture. The demonstration of inherently scalable entanglement on demand resolves one of these outstanding concerns. It is worth investing considerable effort in the last outstanding experimental challenge: entangling remote qubits to form the large entangled states required of a universal quantum processor.

§ A. Overhauser Rate Equations

A.1 Overhauser effect with no T_{1N} process

Recall the basic two-qubit spin Hamiltonian given in Chapter 3.1:

$$\mathcal{H}_0 = \omega_A \hbar \sigma_Z \otimes \sigma_I + \omega_B \hbar \sigma_I \otimes \sigma_Z + \mathcal{A}(\vec{\sigma} \cdot \vec{\sigma}) \tag{A.1.1}$$

$$\text{where } \vec{\sigma} \cdot \vec{\sigma} \equiv \sigma_X \otimes \sigma_X + \sigma_Y \otimes \sigma_Y + \sigma_Z \otimes \sigma_Z \tag{A.1.2}$$

By the principle of detailed balance we have that the population ratios of thermally-populated eigenstates A and B (given by P_A and P_B) must match the ratio of rates connecting them:

$$\frac{P_A}{P_B} = \frac{R_{BA}}{R_{AB}} = \exp((E_A - E_B)/kT) := \alpha_{AB} \tag{A.1.3}$$

where the rate R_{JK} is the rate at which population from eigenstate J moves into the eigenstate K, and E_K is the energy level of eigenstate K. Assuming no nuclear relaxation and no flip-flip relaxation, the above model (visualised in Figure A.1) yields the following

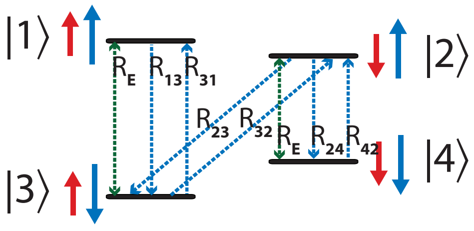

Figure A.1: **Rate equation model in a two spin-$\frac{1}{2}$ system where $w_A >> w_B$.** Illustration of the rates used to calculate Overhauser DNP.

rate equations for $\vec{P} = (P_1, P_2, P_3, P_4)$:

$$\frac{d\vec{P}}{dt} = M\vec{P} \text{ where } M = \begin{pmatrix} -R_{13} - R_E & 0 & R_{31} + R_E & 0 \\ 0 & -R_{23} - R_{24} - R_E & R_{32} & R_{42} + R_E \\ +R_{13} + R_E & R_{23} & -R_{31} - R_{32} - R_E & 0 \\ 0 & R_{24} + R_E & 0 & -R_{42} - R_E \end{pmatrix} \tag{A.1.4}$$

The steady-state solution of this matrix equation is found by the null space of M, given by:

$$\text{Null}(M) = \left(\frac{(R_E + R_{31})(R_E + R_{42})R_{23}}{(R_E + R_{13})(R_E + R_{24})R_{32}}, \frac{(R_E + R_{42})}{(R_E + R_{24})}, \frac{(R_E + R_{42})R_{23}}{(R_E + R_{24})R_{32}}, 1 \right) \tag{A.1.5}$$

$$= \left(\frac{(R_E + R_{31})(R_E + R_{42})}{(R_E + R_{13})(R_E + R_{24})}\alpha_{32}, \frac{(R_E + R_{42})}{(R_E + R_{24})}, \frac{(R_E + R_{42})}{(R_E + R_{24})}\alpha_{32}, 1 \right) \tag{A.1.6}$$

In the regime of a very weak driving field ($R_E \to 0$), this solution becomes

$$= \left(\alpha_{13}\alpha_{32}\alpha_{24}, \alpha_{24}, \alpha_{32}\alpha_{24}, 1 \right) \tag{A.1.7}$$

$$= \left(\alpha_{14}, \alpha_{24}, \alpha_{34}, 1 \right) \tag{A.1.8}$$

and renormalising this solution recovers the expected Boltzmann population distribution. At the other extreme, when the microwaves saturate the transition ($R_E >> \{R_{31}, R_{13}\}$) we arrive at the population distribution given by $\left(\alpha_{32}, 1, \alpha_{32}, 1\right)$, and the positive nuclear polarisation in this instance equals that of the thermal electronic polarisation of the system.

Between these two extremes exists the situation where the electronic transitions are partially, but not completely, saturated. We will assume this saturation is similar for both electronic transitions. For a saturated population ratio S where $\alpha_{24} < \frac{(R_E+R_{42})}{(R_E+R_{24})} = S < 1$, one expects a population distribution of

$$= \left(S^2\alpha_{32}, S, S\alpha_{32}, 1 \right) \tag{A.1.9}$$

which leads to a positive nuclear polarisation of $(S\alpha_{32} - 1)/(S\alpha_{32} + 1)$. Relating S to a reduced spin echo amplitude via $(1 - S) = R(1 - \alpha)$ where α is the population ratio used throughout the main text (for our purposes $\alpha := \alpha_{23} = 1/\alpha_{32}$), we arrive at an expression for the positive Overhauser DNP in terms of R and the electronic polarisation $\mathcal{P} = (1-\alpha)/(1+\alpha)$ given by:

$$\begin{aligned} \text{Nuclear DNP} &= (S-\alpha)/(S+\alpha) && \text{(A.1.10)} \\ &= \frac{R(\alpha-1)-(\alpha-1)}{R(\alpha-1)+(\alpha+1)} && \text{(A.1.11)} \\ &= \frac{R-1}{R-(1/\mathcal{P})} && \text{(A.1.12)} \end{aligned}$$

A.2 OVERHAUSER EFFECT WHERE $T_{1X} >> T_{1N}$

The more general solution to these Overhauser rate equations with a nonzero rate for T_{1N} are cumbersome without some simplifying assumptions. The first assumption we will adopt here is that the driving field is sufficiently strong to completely saturate the microwave transitions. With this we can consider R_{13} and R_{31} to be negligible compared to R_E. The second assumption we will make is that the T_{1N} nuclear relaxation processes do not depend upon the state of the electron. The last assumption used is that the nuclear processes move to equalise nuclear spin populations (i.e. $R_{12} = R_{21} := R_N$); this is only valid in the limit where the thermal nuclear polarisation is very low. The resulting rate equations take on the form:

$$\frac{d\vec{P}}{dt} = M\vec{P} \text{ where } M = \begin{pmatrix} -R_E - R_N & R_N & R_E & 0 \\ R_N & -R_{23} - R_E - R_N & R_{32} & R_E \\ R_E & R_{23} & -R_{32} - R_E - R_N & R_N \\ 0 & R_E & R_N & -R_E - R_N \end{pmatrix} \tag{A.2.1}$$

And the steady-state solution to this simplified rate model takes on the form:

$$\text{Null}(M) = \Big(R_E(2R_N + R_{23}) + R_N R_{32}, R_E(2R_N + R_{32}) + R_N R_{32}, \tag{A.2.2}$$

$$R_E(2R_N + R_{23}) + R_N R_{23}, R_E(2R_N + R_{32}) + R_N R_{23} \Big) \tag{A.2.3}$$

If we define $C = T_{1N}/T_{1X} \approx R_{23}/R_N$ and $\alpha = R_{32}/R_{23}$ and consider this expression in the limit where $R_E \to \infty$, this population distribution reduces to $(2+C, 2+\alpha C, 2+C, 2+\alpha C)$.

If C is very large, the electron polarisation distribution is recovered. If, on the other extreme, $C = 0$ and there is no cross-relaxation (or that it is very slow compared to the nuclear relaxation) this distribution approaches $(2, 2, 2, 2)$ — a perfectly mixed state, as expected.

Intermediate values of C lead to a steady-state nuclear polarisation of

$$(1 - \alpha)/(1 + \alpha + 4/C) \tag{A.2.4}$$

This Overhauser DNP is less than the optimal electron polarisation by a factor of $(1 + \alpha + 4/C)/(1 + \alpha)$: with a known value of α and a measured estimate of the steady-state nuclear polarisation one can estimate $C = T_{1N}/T_{1X}$. Allowing flip-flip contributions to contribute to this relaxation model will further reduce this DNP enhancement, and so any measured DNP polarisation enhancement places an upper bound on the contribution that T_{1N} can play. This in turn places a lower bound on the ratio T_{1N}/T_{1X}.

§ B. Basic model for DQC1

The DQC1 scheme is based upon the *back-action* of CNOT gates; this is simply a statement that conditional operations are able to link the state of one qubit with that of another. The quantum circuit used to perform general DQC1 algorithms are based upon the circuit shown in Figure B.1 and its principles.

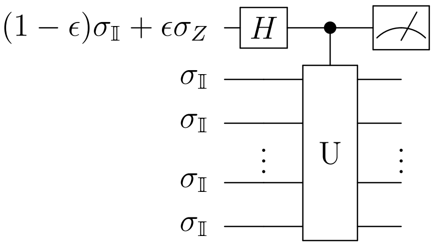

(B.0.1)

Figure B.1: **Basic DQC1 scheme.** A single pure control qubit (or alternatively a pseudopure control qubit paired with a time resource overhead of ϵ^{-2}) can be used to deduce the trace of the N-qubit operator U, as derived below. Measuring the expectation value of the control qubit along X or Y after this sequence reveals the trace of U, as calculated in the expression B.0.6.

A single pure input qubit $|0\rangle\langle 0|$ is acted upon with a *Hadamard gate* $H = (\frac{-\pi}{2})^Y : \pi^Z = \frac{1}{\sqrt{2}}\left(\begin{smallmatrix} 1 & 1 \\ 1 & -1 \end{smallmatrix}\right)$. A controlled unitary is then applied to the maximally mixed set of states given by $\rho = \sigma_{\mathbb{I}}^{\otimes N}$. In ket notation, the pseudopure component ρ_0 evolves according to:

$$\rho_0 = |0\rangle\langle 0| \otimes \rho \tag{B.0.2}$$

$$(H \otimes \sigma_{\mathbb{I}}) \Rightarrow \rho_1 = \frac{1}{2}(|0\rangle\langle 0| + |0\rangle\langle 1| + |1\rangle\langle 0| + |1\rangle\langle 1|) \otimes \rho \tag{B.0.3}$$

$$U \Rightarrow \rho_S = \frac{1}{2}(|0\rangle\langle 0| \otimes \rho + |0\rangle\langle 1| \otimes \rho U^\dagger + |1\rangle\langle 0| \otimes U\rho + |1\rangle\langle 1| \otimes U\rho U^\dagger) \tag{B.0.4}$$

In the basis of the pure input top qubit this can be expressed as:

$$\rho_S = \frac{1}{2}\begin{pmatrix} \rho & \rho U^\dagger \\ U\rho & U\rho U^\dagger \end{pmatrix} \tag{B.0.5}$$

The expectation value of ρ_S in the σ_X basis of the top qubit is

$$\langle X \rangle = \text{Trace}[(\sigma_X \otimes \sigma_{\mathbb{I}})\rho_S] = \text{Trace}\left[\rho\Big(\frac{U + U^\dagger}{2}\Big)\right] \tag{B.0.6}$$

One can see that for $\rho = \sigma_{\mathbb{I}}^{\otimes N}$, this amounts to finding the trace of the unitary U. If the initial input is a pseudopure state the same analysis holds provided one accepts a time resource overhead of ϵ^{-2}, Some problems, including those in quantum metrology, can be reduced to finding the trace of a particular unitary.

BIBLIOGRAPHY

[AA87] Y. Aharonov and J. Anandan. *Phys. Rev. Lett.*, 58:1593, 1987. Cited on page 30.

[Aar08] S. Aaronson. *Sci. Am.*, 298:62, 2008. Cited on pages 1 and 14.

[ABC$^+$04] M. S. Anwar, D. Blazina, H. A. Carteret, S. B. Duckett, T. K. Halstead, J. A. Jones, C. M. Kozak, and R. J. K. Taylor. *Phys. Rev. Lett.*, 93:040501, 2004. Cited on page 8.

[ADP51] J. T. Arnold, S. S. Dharmatti, and M. E. Packard. *J. Chem. Phys.*, 19:507, 1951. Cited on page 44.

[AG78] A. Abragam and M. Goldman. *Rep. Prog. Phys.*, 41:395, 1978. Cited on page 20.

[AGR81] A. Aspect, P. Grangier, and G. Roger. *Phys. Rev. Lett.*, 47:460, 1981. Cited on page 5.

[AL04] P. Aliferis and D. Leung. *Phys. Rev. A*, 70:062314, 2004. Cited on page 22.

[AOV08] L. Amico, A. Osterloh, and V. Vedral. *Rev. Mod. Phys.*, 80:517, 2008. Cited on page 5.

[AvDK$^+$04] D. Aharonov, W. van Dam, J. Kempe, Z. Landau, S. Lloyd, and O. Regev. In *45th Ann. IEEE Symp. Found. Comp. Sci.*, pages 42–51. IEEE, October 2004. Cited on page 21.

[BAB$^+$06] S. C. Benjamin, A. Ardavan, G. A. D. Briggs, D. A. Britz, D. Gunlycke, J. Jefferson, M. A. G. Jones, D. F. Leigh, B. W. Lovett, A. N. Khlobystov,

S. A. Lyon, J. J. L. Morton, K. Porfyrakis, M. R. Sambrook, and A. M. Tyryshkin. *J. Phys. Cond. Matt.*, 18:S867, 2006. Cited on page 16.

[BBCe$^+$93] C. H. Bennett, G. Brassard, C. Crepeau, R. Jozsa, A. Peres, and W. K. Wootters. *Phys. Rev. Lett.*, 70:1895, 1993. Cited on pages 5, 21, and 22.

[BCJ$^+$99] S. L. Braunstein, C. M. Caves, R. Jozsa, N. Linden, S. Popescu, and R. Schack. *Phys. Rev. Lett.*, 83:1054, 1999. Cited on page 8.

[BCM96] S. L. Braunstein, C. M. Caves and G. Milburn. *Ann. Phys.*, 247:135, 1996. Cited on page 69.

[BDDW09] K. Banaszek, R. Demkowicz-Dobrzanski, and I. A. Walmsley. *Nat. Phot.*, 3:673, 2009. Cited on pages 64 and 69.

[BDF$^+$08] S. Boixo, A. Datta, S. Flammia, A. Shaji, E. Bagan, and C. Caves. *Phys. Rev. A*, 77:012317, 2008. Cited on page 75.

[BDR$^+$07] F. Brennecke, T. Donner, S. Ritter, T. Bourdel, M. Köhl, and T. Esslinger. *Nature*, 450:268, 2007. Cited on page 5.

[Bel64] J. S. Bell. *Physics*, 1:195, 1964. Cited on page 5.

[Ber84] M. V. Berry. *Proc. Roy. Soc. A: Math. Phys. Eng. Sci.*, 392:45, 1984. Cited on page 32.

[BGM08] S. Bertaina, S. Gambarelli, T. Mitra, B. Tsukerblat, A. Müller and B. Barbara *Nature*, 453:203, 2008. Cited on page 16.

[BIWH96] J. J. Bollinger, W. M. Itano, D. J. Wineland, and D. J. Heinzen. *Phys. Rev. A*, 54:R4649, 1996. Cited on page 64.

[Blo08] I. Bloch. *Nature*, 453:1016, 2008. Cited on page 22.

[BMR$^+$05] J. Baugh, O. Moussa, C. A. Ryan, A. Nayak, and R. Laflamme. *Nature*, 438:470, 2005. Cited on pages 17 and 20.

[BNT$^+$09] G. Balasubramanian, P. Neumann, D. Twitchen, M. Markham, R. Kolesov, N. Mizuochi, J. Isoya, J. Achard, J. Beck, J. Tissler, V. Jacques, P. R. Hemmer, F. Jelezko, and J. Wrachtrup. *Nature Materials*, 8:383, 2009. Cited on page 17.

[BPM$^+$97] D. Bouwmeester, J.-W. Pan, K. Mattle, M. Eibl, H. Weinfurter, and A. Zeilinger. *Nature*, 390:575, 1997. Cited on page 22.

[BPRA09] P. Becker, H. J. Pohl, H. Riemann, and N. Abrosimov. *Phys. Stat. Sol. A*, 207:49, 2009. Cited on page 118.

[BR01] H. J. Briegel and R. Raussendorf. *Phys. Rev. Lett.*, 86:910, 2001. Cited on page 21.

[BR05] D. E. Browne and T. Rudolph. *Phys. Rev. Lett.*, 95:010501, 2005. Cited on page 22.

[Cam07] E. T. Campbell. *Phys. Rev. A*, 76:040302, 2007. Cited on pages 99 and 124.

[Cas67] T. G. Castner. *Phys. Rev.*, 155:816, 1967. Cited on pages 83 and 84.

[CFBK07] E. T. Campbell, J. Fitzsimons, S. C. Benjamin, and P. Kok. *New J. Phys.*, 9:196, 2007. Cited on page 22.

[CFH97] D. G. Cory, A. F. Fahmy, and T. F. Havel. *Proc. Natl. Acad. Sci.*, 94:1634, 1997. Cited on page 8.

[CG99] I. L. Chuang and D. Gottesman. *Nature*, 402:390, 1999. Cited on page 22.

[CGDT$^+$06] L. Childress, M. V. Gurudev Dutt, J. M. Taylor, A. S. Zibrov, F. Jelezko, J. Wrachtrup, P. R. Hemmer, and M. D. Lukin. *Science*, 314:281, 2006. Cited on page 20.

[Cho10] J. M. Chow. Ph.D. Thesis, Yale, 2010. Cited on page 18.

[CHSH69] J. F. Clauser, M. A. Horne, A. Shimony, and R. A. Holt. *Phys. Rev. Lett.*, 23:880, 1969. Cited on page 6.

[CJ63] T. G. Castner Jr. *Phys. Rev.*, 130:58, 1963. Cited on pages 84 and 91.

[CLL04] M. Curty, M. Lewenstein, and N. Lutkenhaus. *Phys. Rev. Lett.*, 92:217903, 2004. Cited on page 5.

[CMB04] A. R. R. Carvalho, F. Mintert, and A. Buchleitner. *Phys. Rev. Lett.*, 93:230501, 2004. Cited on page 23.

[CP58] J. Culvahouse and F. Pipkin. *Phys. Rev.*, 109:319, 1958. Cited on page 99.

[CVZ$^+$98] I. L. Chuang, L. M. K. Vandersypen, X. Zhou, D. W. Leung, and S. Lloyd. *Nature*, 393:143, 1998. Cited on page 8.

[Deu85] David Deutsch. *Proc. Roy. Soc. London Ser. A*, A400:97, 1985. Cited on page 21.

[DH76] G. Davies and M. F. Hamer. *Proc. Roy. Soc. A: Math. Phys. Eng. Sci.*, 348:285, 1976. Cited on page 16.

[DPS02] A. C. Doherty, P. A. Parrilo, and F. M. Spedalieri. *Phys. Rev. Lett.*, 88:187904, 2002. Cited on page 7.

[DRS$^+$10] L. DiCarlo, M. D. Reed, L. Sun, B. R. Johnson, J. M. Chow, J. M. Gambetta, L. Frunzio, S. M. Girvin, M. H. Devoret, and R. J. Schoelkopf. *Nature*, 467:574, 2010. Cited on page 22.

[DSC08] A. Datta, A. Shaji, and C. M. Caves. *Phys. Rev. Lett.*, 100:050502, 2008. Cited on page 12.

[DVB10] B. Dakić, V. Vedral, and Č. Brukner. *Phys. Rev. Lett.*, 105:190502, 2010. Cited on pages 12 and 13.

[Dzu11] A. Dzurak. Data presented at Spintech 6, Matsue, Japan, August 4th 2011. Cited on page 19.

[Eng05] H. A. Engel. *Science*, 309:586, 2005. Cited on page 22.

[EPR35] A. Einstein, B. Podolsky, and N. Rosen. *Phys. Rev.*, 47:777, 1935. Cited on pages 1 and 5.

[FAC+10] A. Ferraro, L. Aolita, D. Cavalcanti, F. M. Cucchietti, and A. Acín. *Phys. Rev. A*, 81:052318, 2010. Cited on page 12.

[FC72] S. J. Freedman and J. F. Clauser. *Phys. Rev. Lett.*, 28:938, 1972. Cited on page 5.

[FDT+09] G. D. Fuchs, V. V. Dobrovitski, D. M. Toyli, F. J. Heremans, and D. D. Awschalom. *Science*, 326:1520, 2009. Cited on page 17.

[Feh56] G. Feher. *Phys. Rev.*, 103:834, 1956. Cited on pages 20, 53, and 96.

[Feh59] G. Feher. *Phys. Rev. Lett.*, 3:135, 1959. Cited on page 93.

[FG59] G. Feher and E. A. Gere. *Phys. Rev.*, 114:1245, 1959. Cited on pages 56, 86, 89, 92, and 97.

[FGG+01] E. Farhi, J. Goldstone, S. Gutmann, J. Lapan, A. Lundgren, and D. Preda. *Science*, 292:472, 2001. Cited on page 21.

[Fil11] V. Filidou. D.Phil. thesis, Oxford, 2011. Cited on pages 128 and 131.

[FMZ+10] M. Fuechsle, S. Mahapatra, F. A. Zwanenburg, M. Friesen, M. A. Eriksson, and M. Y. Simmons. *Nature Nano.*, 5:502, 2010. Cited on page 22.

[FYPM54] R. C. Fletcher, W. A. Yager, G. L. Pearson, and F. R. Merritt. *Phys. Rev.*, 95:844, 1954. Cited on pages 16 and 47.

[GHZ89] D. M. Greenberger, M. A. Horne, and A. Zeilinger. *Bell's Theorem, Quantum Theory, and Conceptions of the Universe*, pages 69–72, 1989. Cited on page 64.

[GLM06] V. Giovannetti, S. Lloyd, and L. Maccone. *Phys. Rev. Lett.*, 96:010401, 2006. Cited on pages 63, 64, and 69.

[GLvdM$^+$10] P. T. Greenland, S. A. Lynch, A. F. G. van der Meer, B. N. Murdin, C. R. Pidgeon, B. Redlich, N. Q. Vinh, and G. Aeppli. *Nature*, 465:1057, 2010. Cited on page 18.

[GWR$^+$10] R. E. George, W. Witzel, H. Riemann, N. V. Abrosimov, N. Notzel, M. L. W. Thewalt, and J. J. L. Morton. *Phys. Rev. Lett.*, 105:067601, 2010. Cited on pages 84 and 99.

[GZN$^+$10] C. Gross, T. Zibold, E. Nicklas, J. Estève, and M. K. Oberthaler. *Nature*, 464:1165, 2010. Cited on page 15.

[Hah50] E. Hahn. *Phys. Rev.*, 80:580, 1950. Cited on page 50.

[Hei02] W. D. Heiss. *Fundamentals of quantum information: quantum computation, communication, decoherence, and all that.* Springer, 2002. Cited on page 5.

[Hem02] L. A. Hemaspaandra. *SIGACT News*, 33:34, 2002. Cited on page 13.

[HGM86] P. Höfer, A. Grupp, and M. Mehring. *Phys. Rev. A*, 33:3519, 1986. Cited on page 57.

[HHG$^+$97] P. Horak, G. Hechenblaikner, K. Gheri, H. Stecher, and H. Ritsch. *Phys. Rev. Lett.*, 79:4974, 1997. Cited on page 20.

[HHH96] M. Horodecki, P. Horodecki, and R. Horodecki. *Phys. Lett. A*, 223:1, 1996. Cited on page 6.

[HHH97] M. Horodecki, P. Horodecki, and R. Horodecki. *Phys. Rev. Lett.*, 78:574, 1997. Cited on page 37.

[HHHH09] R. Horodecki, P. Horodecki, M. Horodecki, and K. Horodecki. *Rev. Mod. Phys.*, 81:865, 2009. Cited on pages 5 and 7.

[HHR$^+$05] H. Häffner, W. Hänsel, C. F. Roos, J. Benhelm, D. Chek-Al-Kar, M. Chwalla, T. Körber, U. D. Rapol, M. Riebe, P. O. Schmidt, C. Becher, O. Gühne, W. Dür, and R. Blatt. *Nature*, 438:643, 2005. Cited on page 8.

[HS60] A. Hoing and E. Stupp. *Phys. Rev.*, 117:69, 1960. Cited on pages 89 and 91.

[HSM06] J. Harrison, M. Sellars, and N. Manson. *Diamond Rela. Mat.*, 15:586, 2006. Cited on page 20.

[HSSP99] J. Hald, J. L. Sorensen, C. Schori, and E. S. Polzik. *Phys. Rev. Lett.*, 83:1319, 1999. Cited on page 9.

[JKF$^+$09] J. A. Jones, S. D. Karlen, J. Fitzsimons, A. Ardavan, S. C. Benjamin, G. A. D. Briggs, and J. J. L. Morton. *Science*, 324:1166, 2009. Cited on pages 15, 63, 64, and 66.

[JKK$^+$10] T. Jorg, F. Krzakala, J. Kurchan, A. C. Maggs, and J. Pujos. *Europhys. Lett.*, 89:40004, 2010. Cited on page 21.

[JKP01] B. Julsgaard, A. Kozhekin, and E. S. Polzik. *Nature*, 413:400, 2001. Cited on page 9.

[JL03] R. Jozsa and N. Linden. *Proc. Roy. Soc. A: Math. Phys. Eng. Sci.*, 459:2011, 2003. Cited on pages 5, 10, and 11.

[JM98] J. A. Jones and M. Mosca. *J. Chem. Phys.*, 109, 1648, 1998. Cited on pages 8, 39, 60, and 61.

[Jon01] J. A. Jones. *Prog. NMR Spec.*, 38:325, 2001. Cited on page 77.

[Jon11] J. A. Jones. *Prog. NMR Spec.*, 59:91, 2011. Cited on page 48.

[Jor11] S. Jordan. Quantum Algorithm Zoo: http://math.nist.gov/quantum/zoo/. Cited on pages 1 and 10.

[Joz94] R. Jozsa. *J. Mod. Opt.*, 41:3215, 1994. Cited on page 9.

[JSD07] C. Ju, D. Suter and J. Du *Phys. Rev. A*, 75:012318, 2007. Cited on page 125.

[Kan98] B. E. Kane. *Nature*, 393:133, 1998. Cited on pages 39 and 144.

[KBD04] P. Kok, S. L. Braunstein, and J. P. Dowling. *J. Opt. B: Quantum Semiclass. Opt.*, 6:S811, 2004. Cited on page 15.

[KCL98] E. Knill, I. Chuang, and R. Laflamme. *Phys. Rev. A*, 57:3348, 1998. Cited on page 19.

[KLM$^+$01a] H. Kimble, Y. Levin, A. Matsko, K. Thorne, and S. Vyatchanin. *Phys. Rev. D*, 65:022002, 2001. Cited on page 15.

[KLM01b] E. Knill, R. Laflamme, and G. J. Milburn. *Nature*, 409:46, 2001. Cited on page 22.

[KLMT00] E. Knill, R. Laflamme, R. Martinez, and C.-H. TSeng. *Nature*, 404:368, 2000. Cited on pages 16 and 64.

[KLR$^+$08] E. Knill, D. Leibfried, R. Reichle, J. Britton, R. Blakestad, J. Jost, C. Langer, R. Ozeri, S. Seidelin, and D. Wineland. *Phys. Rev. A*, 77:012307, 2008. Cited on page 18.

[KS04] H. Krojanski and D. Suter. *Phys. Rev. Lett.*, 93:090501, 2004. Cited on page 23.

[KSM$^+$03] D. Karaiskaj, J. A. H. Stotz, T. Meyer, M. L. W. Thewalt, and M. Cardona. *Phys. Rev. Lett.*, 90:186402, 2003. Cited on pages 17 and 117.

[KSW$^+$05] N. Kiesel, C. Schmid, U. Weber, G. Tóth, O. Gühne, R. Ursin, and H. Weinfurter. *Phys. Rev. Lett.*, 95:210502, 2005. Cited on page 22.

[LCYY00] D. Leung, I. Chuang, F. Yamaguchi, and Y. Yamamoto. *Phys. Rev. A*, 61:042310, 2000. Cited on pages 59 and 60.

[Lev01] M. H. Levitt. *Spin Dynamics: Basics of Nuclear Magnetic Resonance; 2nd ed.* Wiley, Chichester, 2001. Cited on pages 18, 40, 44, 45, and 60.

[LG08] C. Lazarou and B. M. Garraway. *Phys. Rev. A*, 77:023818, 2008. Cited on page 9.

[LH61] R. Levitt and A. Honig. *J. Phys. Chem. Sol.*, 22:269, 1961. Cited on pages 88 and 90.

[Lid04] D. A. Lidar. *New J. Phys.*, 6:167, 2004. Cited on page 12.

[LLVC09] D. Leibrandt, J. Labaziewicz, V. Vuletić, and I. Chuang. *Phys. Rev. Lett.*, 103:103001, 2009. Cited on page 20.

[LS93] R. G. Larsen and D. J. Singel. *J. Chem. Phys.*, 98:5134, 1993. Cited on page 18.

[LSS92] A. Luis and L. L. Sánchez-Soto. *Opt. Comm.*, 89:140, 1992. Cited on page 63.

[Mer11] Z. Merali. *Nature*, 474:24, 2011. Cited on page 1.

[MF79] G. A. Morris and R. Freeman. *J. Am. Chem. Soc.*, 101:760, 1979. Cited on pages 20 and 73.

[MGF$^+$10] A. Mohan, P. Gallo, M. Felici, B. Dwir, A. Rudra, J. Faist, and E. Kapon. *Small*, 6:1268, 2010. Cited on page 18.

[MKB04] F. Mintert, M. Kus, and A. Buchleitner. *Phys. Rev. Lett.*, 92:167902, 2004. Cited on page 7.

[MKB05] F. Mintert, M. Kus, and A. Buchleitner. *Phys. Rev. Lett.*, 95:260502, 2005. Cited on pages 7 and 35.

[MMK$^+$95] C. Monroe, D. M. Meekhof, B. E. King, W. M. Itano, and D. J. Wineland. *Phys. Rev. Lett.*, 75:4714, 1995. Cited on page 8.

[Mor05] G. Morley. D.Phil. thesis, Oxford, 2005. Cited on page 16.

[Mor09] J. J. L. Morton. arXiv:0905.4008v1, 2009. Cited on page 144.

[MPZ$^+$10] A. Morello, J. J. Pla, F. A. Zwanenburg, K. W. Chan, K. Y. Tan, H. Huebl, M. Mottonen, C. D. Nugroho, C. Yang, J. A. van Donkelaar, A. D. C. Alves, D N. Jamieson, C C. Escott, L C. L. Hollenberg, R. G. Clark, and A. S. Dzurak. *Nature*, 467:687, 2010. Cited on pages 22, 105, 124, and 144.

[MSB+11] T. Monz, P. Schindler, J. Barreiro, M. Chwalla, D. Nigg, W. Coish, M. Harlander, W. Hänsel, M. Hennrich, and R. Blatt. *Phys. Rev. Lett.*, 106:130506, 2011. Cited on page 22.

[MTA+05a] J. J. L. Morton, A. M. Tyryshkin, A. Ardavan, K. Porfyrakis, S. A. Lyon, and G. A. D. Briggs. *Phys. Rev. Lett.*, 95:200501, 2005. Cited on pages 17, 31, and 39.

[MTA+05b] J. J. L. Morton, A. Tyryshkin, A. Ardavan, K. Porfyrakis, S. A. Lyon, and G. A. D. Briggs. *Phys. Rev. A*, 71:012332, 2005. Cited on page 51.

[MTA+06] J. J. L. Morton, A. M. Tyryshkin, A. Ardavan, S. C. Benjamin, K. Porfyrakis, S. A. Lyon, and G. A. D. Briggs. *Nature Physics*, 2:40, 2006. Cited on pages 17, 18, and 30.

[MTB+08] J. J. L. Morton, A. M. Tyryshkin, R. M. Brown, S. Shankar, B. W. Lovett, A. Ardavan, T. Schenkel, E. E. Haller, J. W. Ager, and S. A. Lyon. *Nature*, 455:1085, 2008. Cited on pages 16, 40, 56, 57, 58, and 126.

[MvTA+07] Gavin W Morley, Johan van Tol, Arzhang Ardavan, Kyriakos Porfyrakis, Jinying Zhang, and G Andrew D Briggs. *Phys. Rev. Lett.*, 98:220501, 2007. Cited on page 96.

[MvTMB09] D. R. McCamey, J. van Tol, G. W. Morley, and C. Boehme. *Phys. Rev. Lett.*, 102:027601, 2009. Cited on page 94.

[MvTMB10] D. R. McCamey, J. van Tol, G. W. Morley, and C Boehme. *Science*, 330:1652, 2010. Cited on page 97.

[MWCV10] Kavan Modi, Mark Williamson, Hugo Cable, and Vlatko Vedral. arXiv:1003.1174v3, 2010. Cited on page 72.

[MWS+10] G. W. Morley, M. Warner, A. M. Stoneham, P. T. Greenland, J. van Tol, C. W. M. Kay, and G. Aeppli. *Nature Materials*, 9:725, 2010. Cited on pages 84 and 99.

[MWY+11] M. Mariantoni, H. Wang, T. Yamamoto, M. Neeley, R. C. Bialczak, Y. Chen, M. Lenander, E. Lucero, A. D. O'Connell, D. Sank, M. Weides, J. Wenner, Y. Yin, J. Zhao, A. N. Korotkov, A. N. Cleland, and J. M. Martinis. *Science*, 10:1208517, 2011. Cited on page 22.

[NC00] M. A. Nielsen and I. L. Chuang. *Quantum Computation and Quantum Information.* Cambridge University Press, 2000. Cited on pages 1, 4, 9, 11, 19, 22, 34, 35, and 99.

[NKL98] M. A. Nielsen, E. Knill, and R. Laflamme. *Nature*, 396:52, 1998. Cited on page 22.

[NKN07] K. C. Nowack, F. H. L. Koppens, Y. V. Nazarov and L. M. K. Vandersypen *Science*, 318:1430, 2007. Cited on page 16.

[NMR+06] C. Negrevergne, T. S. Mahesh, C. A. Ryan, M. Ditty, F. C. Racine, W. Power, N. Boulant, T. Havel, D. G. Cory, and R. Laflamme. *Phys. Rev. Lett.*, 96:170501, 2006. Cited on pages 8, 17, 22, and 39.

[NMR+08] P. Neumann, N. Mizuochi, F. Rempp, P. Hemmer, H. Watanabe, S. Yamasaki, V. Jacques, T. Gaebel, F. Jelezko, and J. Wrachtrup. *Science*, 320:1326, 2008. Cited on page 9.

[NSL+11] K. C. Nowack, M. Shafiei, M. Laforest, G. E. D. K. Prawiroatmodjo, L. R. Schreiber, C, Reichl, W, Wegscheider, and L. M. K. Vandersypen. *Science*, 333:1269, 2011. Cited on page 22.

[Ove53] A. W. Overhauser. *Phys. Rev.*, 92:411, 1953. Cited on pages 20 and 92.

[OWC+11] C. Ospelkaus, U. Warring, Y. Colombe, K. R. Brown, J. M. Amini, D. Leibfried, and D. J. Wineland. *Nature*, 476:181, 2011. Cited on page 22.

[Par70] J. L. Park. *Found. Phys.*, 1:23, 1970. Cited on page 21.

[PBWZ98] J.-W. Pan, D. Bouwmeester, H. Weinfurter, and A. Zeilinger. *Phys. Rev. Lett.*, 80:3891, 1998. Cited on page 22.

[PDS05] X. Peng, J. Du and D. Suter *Phys. Rev. A* 71:012307, 2005. Cited on page 8.

[Per96] A. Peres. *Phys. Rev. Lett.*, 77:1413, 1996. Cited on page 6.

[Per00] A. Peres. *J. Mod. Opt.*, 47:139, 2000. Cited on page 22.

[PGA$^+$11] M. Piani, S. Gharibian, G. Adesso, J. Calsamiglia, P. Horodecki, and A. Winter. *Phys. Rev. Lett.*, 106:220403, 2011. Cited on pages 12 and 13.

[PLG10] J. R. Petta, H. Lu, and A. C. Gossard. *Science*, 327:669, February 2010. Cited on page 22.

[PMRL09] G. Passante, O. Moussa, C. A. Ryan, and R. Laflamme. *Phys. Rev. Lett.*, 103:250501, 2009. Cited on page 13.

[Pow58] J. G. Powles. *Proc. Phys. Soc.*, 71:497, 1958. Cited on page 22.

[RB01] R. Raussendorf and H. J. Briegel. *Phys. Rev. Lett.*, 86:5188, 2001. Cited on page 21.

[RBSH11] L. Robledo, H. Bernien, T. van der Sar, and R. Hanson. *New J. Phys.*, 13:025013, 2011. Cited on page 20.

[RCB$^+$11] L. Robledo, L. Childress, H. Bernien, B. Hensen, P. F. A. Alkemade, and R. Hanson. *Nature*, 477:574, 2011. Cited on page 19.

[RH07] R. Raussendorf and J. Harrington. *Phys. Rev. Lett.*, 98:190504, 2007. Cited on page 17.

[RLL09] C. A. Ryan, M. Laforest, and R. Laflamme. *New J. Phys.*, 11:013034, 2009. Cited on page 17.

[RPP$^+$07] K. Resch, K. Pregnell, R. Prevedel, A. Gilchrist, G. Pryde, J. OBrien and A. White. *Phys. Rev. Lett.*, 98:223601, 2007. Cited on page 69.

[RZMK38] I. Rabi, J. Zacharias, S. Millman, and P. Kusch. *Phys. Rev.*, 53:318, 1938. Cited on page 18.

[SAB+06] M. Steffen, M. Ansmann, C. Bialczak, N. Katz, E. Lucero, R. McDermott, M. Neely, E. M. Weig, A. N. Cleland, and J. M. Martinis. *Science*, 313:1423, 2006. Cited on page 9.

[Sak93] J. J. Sakurai. *Modern Quantum Mechanics.* Addison Wesley, 1993. Cited on pages 5 and 19.

[SBM+11] P. Schindler, J. T. Barreiro, T. Monz, V. Nebendahl, D. Nigg, M. Chwalla, M. Hennrich, and R. Blatt. *Science*, 332:1059, 2011. Cited on page 22.

[SBR+11] S. Simmons, R. M. Brown, H. Riemann, N. V. Abrosimov, P. Becker, H. J. Pohl, M. L. W. Thewalt, K. M. Itoh, and J. J. L. Morton. *Nature*, 470:69, 2011. Cited on pages 18, 20, 96, 112, 122, and 124.

[Sch95] Z. Schreiber. MSc. thesis, Imperial College, 1995. Cited on page 3.

[SCHP87] D. Suter, G. Chingas, R. A. Harris and A. Pines *Mol. Phys.*, 61:1327, 1987 Cited on page 30.

[SGMF10] M. Schaffry, E. M. Gauger, J. J. L. Morton, J. Fitzsimons, S. C. Benjamin and B. W. Lovett. *Phys. Rev. A*, 82:042114, 2010. Cited on pages 69 and 72.

[Sho94] P. W. Shor. *FOCS*, pages 124–134, 1994. Cited on page 13.

[SJ08a] A. Schweiger and G. Jeschke. *Principles of Pulse Electron Paramagnetic Resonance.* Oxford University Press, 2008. Cited on pages 18, 40, and 44.

[SJ08b] P. W. Shor and S. P. Jordan. *Quantum Info. Comp.*, 8:681, 2008. Cited on pages 12 and 19.

[SJK+10] S. Simmons, J. A. Jones, S. D. Karlen, A. Ardavan, and J. J. L. Morton. *Phys. Rev. A*, 82:022330, 2010. Cited on pages 64, 68, 75, and 78.

[SLG11] M. Schaffry, B. Lovett, and E. Gauger. *Phys. Rev. A*, 84:032332, 2011. Cited on page 134.

[SMP88] D. Suter, K. T. Mueller, and A. Pines. *Phys. Rev. Lett.*, 60:1218, 1988. Cited on page 30.

[SMW05] L. J. Schulman, T. Mor, and Y. Weinstein. *Phys. Rev. Lett.*, 94:120501, 2005. Cited on pages 20 and 98.

[Sør89] O. W. Sørensen. *Prog. NMR Spec.*, 21:503, 1989. Cited on page 73.

[SPM86] D. Suter, A. Pines and M. Mehring *Phys. Rev. Lett.*, 57:242, 1986. Cited on page 31.

[SSS+10] T. Sekiguchi, M. Steger, K. Saeedi, M. L. W. Thewalt, H. Riemann, N. V. Abrosimov, and N. Nötzel. *Phys. Rev. Lett.*, 104:137402, 2010. Cited on pages 99 and 100.

[SSY+11] M. Steger, T. Sekiguchi, A. Yang, K. Saeedi, M. E. Hayden, M. L. W. Thewalt, K. M. Itoh, H. Riemann, N. V. Abrosimov, P. Becker, and H. J. Pohl. *J. Appl. Phys.*, 109:102411, 2011. Cited on page 105.

[STA59] A. Stam. *Information and Control*, 2:101, 1959. Cited on page 69.

[Sza05] S. Szarek. *Phys. Rev. A*, 72:032304, 2005. Cited on page 11.

[Ter00] B. M. Terhal. *Phys. Rev. A*, 271:319, 2000. Cited on page 7.

[The11] M. L. W. Thewalt. Data presented at SpinTech 6, August 2011, Matsue Japan, 2011. Cited on pages 17 and 86.

[TLAR03] A. M. Tyryshkin, S. A. Lyon, A. V. Astashkin, and A. M. Raitsimring. *Phys. Rev. B*, 68:193207, 2003. Cited on page 118.

[TMAL06] A. M. Tyryshkin, J. J. L. Morton, A. Ardavan, and S. A. Lyon. *J. Chem. Phys.*, 124:234508, 2006. Cited on page 54.

[Tot05] G. Toth. *Phys. Rev. A*, 71:010301, 2005. Cited on page 7.

[TPS+11] N. Thomas-Peter, B. Smith, A. Datta, L. Zhang, U. Dorner, I. Walmsley. *Phys. Rev. Lett.*, 107:113603, 2011. Cited on pages 15 and 69.

[TTM+11] A. M. Tyryshkin, S. Tojo, J. J. L. Morton, H. Riemann, N. V. Abrosimov, P. Becker, H.-J. Pohl, T. Schenkel, M. L. W. Thewalt, K. Itoh, and S. A. Lyon. arXiv:1105.3772v1, 2011. Cited on pages 17, 18, and 51.

[TWC+11] M. Tsang, H. Wiseman and C. Caves. *Phys. Rev. Lett.*, 106:090401, 2011. Cited on page 69.

[TWK+98] Q. A. Turchette, C. S. Wood, B. E. King, C. J. Myatt, D. Leibfried, W. M. Itano, C. Monroe, and D. J. Wineland. *Phys. Rev. Lett.*, 81:3631, 1998. Cited on page 8.

[UVB01] R. G. Unanyan, N. V. Vitanov, and K. Bergmann. *Phys. Rev. Lett.*, 87:137902, 2001. Cited on page 9.

[VAdM01] F. Verstraete, K. Audenaert, and B. de Moor. *Phys. Rev. A*, 64:12316, 2001. Cited on page 119.

[Ved10] V. Vedral. *Found Phys*, 40(8):1141, 2010. Cited on page 10.

[VLM+10] A. N. Vamivakas, C.-Y. Lu, C. Matthiesen, Y. Zhao, S. Fält, A. Badolato, and M. Atatüre. *Nature*, 467:297, 2010. Cited on page 19.

[VPM+07] G. Vallone, E. Pomarico, P. Mataloni, F. De Martini, and V. Berardi. *Phys. Rev. Lett.*, 98:180502, 2007. Cited on page 21.

[VSB+01] L. M. K. Vandersypen, M. Steffen, G. Breyta, C. S. Yannoni, M. H. Sherwood, and I. L. Chuang. *Nature*, 414:883, 2001. Cited on pages 17 and 39.

[Wal83] D. F. Walls. *Nature*, 306:141, 1983. Cited on page 9.

[Wat09] J. Watrous. Enc. Complexity Sys. Sci., 17:7174, 2009. Cited on page 13.

[Wer89] R. F. Werner. *Phys. Rev. A*, 40:4277, 1989. Cited on page 5.

[WF61] D. K. Wilson and G. Feher. *Phys. Rev.*, 124:1068, 1961. Cited on page 18.

[WMD05] D.-W. Wang, E. G. Mishchenko, and E. Demler. *Phys. Rev. Lett.*, 95:086802, 2005. Cited on page 5.

[WMK+00] D. J. Wineland, C. J. Myatt, B. E. King, Q. A. Turchette, C. A. Sackett, D. Kielpinski, W. M. Itano, and C. Monroe. *Nature*, 403:269, 2000. Cited on page 23.

[WNG+03] T. C. Wei, K. Nemoto, P. M. Goldbart, P. G. Kwiat, W. J. Munro, and F. Verstraete. *Phys. Rev. A*, 67:22110, 2003. Cited on pages 4, 37, and 119.

[Woo98] W. K. Wootters. *Phys. Rev. Lett.*, 80:2245, 1998. Cited on pages 6 and 7.

[WPA+04] P. Walther, J.-W. Pan, M. Aspelmeyer, R. Ursin, S. Gasparoni, and A. Zeilinger. *Nature*, 429:158, 2004. Cited on page 64.

[Wra10] J. Wrachtrup. *Proc. Natl. Acad. Sci.*, 107:9479, 2010. Cited on page 16.

[WRR+05] P. Walther, K. J. Resch, T. Rudolph, E. Schenck, H. Weinfurter, V. Vedral, M. Aspelmeyer, and A. Zeilinger. *Nature*, 434:169, 2005. Cited on page 21.

[WW01] R. F. Werner and M. M. Wolf. *Phys. Rev. A*, 64:032112, 2001. Cited on page 6.

[YCZ+08] Z.-S. Yuan, Y.-A. Chen, B. Zhao, S. Chen, J. Schmiedmayer, and J.-W. Pan. *Nature*, 454:1098, 2008. Cited on page 22.

[YSS+09] A. Yang, M. Steger, T. Sekiguchi, M. L. W. Thewalt, T. D. Ladd, K. M. Itoh, H. Riemann, N. V. Abrosimov, P. Becker, and H. J. Pohl. *Phys. Rev. Lett.*, 102:257401, 2009. Cited on pages 20 and 94.

[Yur86] B. Yurke. *Phys. Rev. Lett.*, 56:1515, 1986. Cited on page 15.

[ZBLW02] M. Zukowski, Č. Brukner, W. Laskowski, and M. Wiesniak. *Phys. Rev. Lett.*, 88:210402, 2002. Cited on page 6.

[ŻZHE93] M Żukowski, A. Zeilinger, M. Horne, and A. Ekert. *Phys. Rev. Lett.*, 71:4287, 1993. Cited on page 22.